

POLITECNICO DI MILANO
School of Industrial and Information Engineering
Master of Science in Automation and Control Engineering



Multicopter UAVs for fugitive emissions detection:
sizing, modelling and control system design

Advisor: Prof. Marco LOVERA
Co-Advisor: Eng. Paolo GATTAZZO
Co-Advisor: Eng. Mattia GIURATO

Thesis by:
Marco MACCOTTA Matr. 852544

Academic Year 2017–2018

*Ai miei Genitori,
che non hanno mai smesso di credere in me.*

Acknowledgments

Vi sono momenti in cui le parole non possono esprimere cosa proviamo veramente e soprattutto in alcuni casi la parola "grazie" non risulta sufficiente a dimostrare il nostro sentimento di riconoscenza per tutto il supporto ricevuto. Seppur questa sia una di quelle circostanze vorrei tentare ugualmente. Prima di tutto vorrei ringraziare il Professore Lovera Marco, per la sua professionalità ed i preziosi consigli, soprattutto durante la stesura della tesi.

Un sentito ringraziamento va anche a Paolo Gattazzo e Mattia Giurato per la loro pazienza e l'aiuto datomi durante tutto il progetto di tesi. Ringrazio inoltre Simone Panza e tutto il gruppo dell'ASCL per il loro supporto e la loro compagnia. Vorrei inoltre ringraziare i miei amici e compagni di studi Marco, Dave, Lorenzo, Davide, Francesco, Cosimo, Riccardo, Angelo per essermi stati accanto ad aver arricchito questo periodo della mia vita. Grazie anche a tutti coloro che ho conosciuto e con cui ho condiviso quasi tre anni qui a Milano.

Non dimentico certamente i miei amici e compagni più stretti fin dall'infanzia Giovanni e Walter i quali, nonostante la distanza, si dimostrano sempre interessati ai miei progressi.

Inoltre, un ringraziamento speciale va alla persona che proprio in questi anni mi ha sopportato ed aiutato rimanendomi accanto sia nei momenti difficili che in quelli felici, grazie Tania.

Infine, ma assolutamente di non minor importanza, alla mia famiglia va il ringraziamento più sentito e l'abbraccio più caloroso. Grazie a mio fratello Alessio ed ai miei genitori Antonio e Mariagrazia, che mi hanno sempre sostenuto ed incoraggiato anche nei momenti più complicati dandomi oltretutto la possibilità di svolgere gli studi. Grazie ai miei nonni ed i miei zii, sempre a disposizione e presenti in qualsiasi situazione.

Tutti voi avete contribuito al raggiungimento di questo traguardo. Grazie.

Abstract

Nowadays, the Remotely Piloted Aircrafts (RPAs) are more and more popular thanks to the large number of application fields where they can be adopted. When referring to a drone, usually one refers to a category of RPAs with four, six, or eight motors. Especially, these aircrafts have become increasingly used in the field of aerial monitoring and inspection of dangerous areas. The work conducted within this thesis is focused on multirotor RPAs suited for monitoring industrial areas and detecting hazardous gases. These platforms apart from the commonly used sensors (barometer, IMU) need to include vision systems (to provide for the lack of global positioning signal in the target areas) and gas detection instruments. In particular the choice of gas detectors is related to the task and spectrum of gases to be monitored. Furthermore, due to the heavy weight and dimensions of these devices, hexacopters and octocopters result to be the most suitable platforms. Starting from these premises, the purpose of this thesis is to size, model and analyse the behaviour of a hexacopter and an octocopter flying robot (able to perform monitoring missions and to detect industrial gases) when a motor fault occurs and a Linear Virtual Actuator (LVA) is applied.

Initially the requirements associated to the multirotor platform, the vision system and the gas detector are exposed. Then a size procedure is described and applied to a hexacopter (with "H" structure) and to an octocopter (with "X" structure). This allows to find the most reasonable choice of motors and propellers based on the requirements specified. The same motors and propellers adopted on the hexa-configuration are then applied to the octo-structure too. Once identified the parameters of the actuators and the moments of inertia terms, the multicopters models are presented. Moreover PID controllers are tuned based on an H_∞ approach. Finally a reconfigurability tolerance analysis to actuators fault is applied together with the implementation of a LVA to both the multicopter models.

Sommario

Al giorno d'oggi, gli aeromobili a pilotaggio remoto (APR) sono sempre più diffusi grazie ai numerosi campi d'applicazione dove possono essere impiegati. Quando ci si riferisce ad un drone, si fa riferimento ad una categoria di APR con quattro, sei oppure otto rotori. In particolar modo, questi velivoli sono diventati sempre più utilizzati nel campo del monitoraggio aereo ed ispezione di aree pericolose. Questo lavoro di tesi si concentra su piattaforme multirotores specializzate nel monitoraggio di aree industriali e rilevazione di gas pericolosi. A prescindere dai sensori comunemente utilizzati (barometro e unità di misura inerziali), tali velivoli implementano anche sistemi di visione (utilizzati per sopperire alla mancanza di segnale GPS nelle aree d'interesse) e sistemi d'individuazione di gas. In particolare, la scelta del rilevatore di gas è legata allo spettro dei gas da individuare. Inoltre, a causa dell'elevato peso e dimensione di tali dispositivi, le piattaforme tipicamente utilizzate dispongono di sei od otto rotori. A partire da queste premesse, lo scopo di questo lavoro di tesi è il dimensionamento, modellizzazione ed analisi delle prestazioni di due piattaforme, un esacottero ed un ottocottero (adatte al compimento di operazioni di monitoraggio e rilevazione di gas industriali) quando, dopo il guasto e la perdita di uno dei motori, il sistema è riconfigurato tramite la tecnica dell'attuatore lineare virtuale.

Inizialmente, verranno esposti i requisiti associati al velivolo, al tipo di sistema di visione ed alla scelta del rilevatore di gas. Di conseguenza, verrà descritta una procedura di dimensionamento da applicare ad un esacottero con struttura ad "H" ed un ottocottero con struttura ad "X". Questa permetterà di identificare la coppia motori-eliche più adatta al caso in esame. Le caratteristiche e parametri dei motori verranno calcolate insieme alle quantità fisiche della macchina ed i modelli dei due multicotteri saranno presentati. Conseguentemente un sistema di controllo lineare (ottenuto tramite sintesi H_∞) sarà calcolato ed implementato. Infine verrà eseguita un'analisi di riconfigurabilità seguita dall'implementazione di un sistema di riconfigurazione di tipo LVA su entrambi i modelli.

Contents

Acknowledgments	I
Abstract	III
Sommario	V
List of figures	IX
List of tables	XIII
Introduction	1
1 Requirements and technology review	3
1.1 Mission and requirements	3
1.2 Vision systems	4
1.2.1 Camera: mathematical description	4
1.2.2 Stereo camera: model	6
1.2.3 Analysis and comparison of stereo cameras	7
1.3 Measurement and detection instruments	9
1.3.1 Instruments analysis and comparison	9
1.3.2 Laser targeting system precision	11
1.4 Platform selection	16
2 Preliminary drone design	19
2.1 Methodology	19
2.1.1 On-board energy storage	19
2.1.2 Actuators and speed controllers	20
2.1.3 Sizing	20
2.2 Results	24
2.2.1 Parameters and requirements	24
2.2.2 Hexacopter sizing	24
2.2.3 Octocopter sizing	29

3	Dynamic modelling and simulation	35
3.0.1	Objectives	35
3.1	Actuator analysis	35
3.1.1	Momentum theory in hovering flight	35
3.1.2	Thrust and torque coefficient identification	37
3.1.3	Results	38
3.2	Dynamics of a multirotor UAV	39
3.2.1	Rotations formalism and equations of motion	39
3.2.2	External forces and moments	41
3.3	Inertia matrix	45
3.3.1	Hexacopter	45
3.3.2	Octocopter	46
3.3.3	Results	48
3.4	Simulink	48
4	Control law design	51
4.1	Hovering model	51
4.2	Control strategy	52
4.2.1	Structured H_∞ synthesis	52
4.2.2	Method and PID structure	53
4.2.3	Hexacopter tuning requirements	55
4.2.4	Hexacopter simulation results	61
4.2.5	Octocopter	66
4.2.6	Octocopter simulation results	69
4.3	Drift analysis of the vision system	74
5	Fault tolerance analysis	85
5.1	Basic concepts	85
5.2	Application	86
5.3	Hexacopter	90
5.3.1	Simulation	91
5.4	Octocopter	96
5.4.1	Simulation	97
	Conclusions	103

List of Figures

1.1	Perspective projection of a 3D point P on the image plane	5
1.2	Stereo vision model	6
1.3	(a) Diagonal, vertical and horizontal field of view; (b) Jello effect .	7
1.4	Paralleling of stereo vision systems	8
1.5	Diffusion detector example	10
1.6	Laser detector example	10
1.7	Example of an infrared thermal camera for gases detection	11
1.8	Laser targeting system mounted on Hexa2	12
1.9	3D trajectory performed by Hexa2	13
1.10	Yaw motion in position holding	14
1.11	North-(-Down) plane	14
2.1	Examples of thrust coefficient (a) and flight time (b) with respect to battery weight and for three payloads (1 kg, 1.5 kg, 2 kg), in a hexacopter	23
2.2	Hexacopter frame	25
2.3	T-Motor MN3515 KV400	25
2.4	Thrust coefficient (a) and flight time (b) with respect to battery weight and for three payloads (1 kg, 1.5 kg, 2 kg)	27
2.5	eCalc results	28
2.6	Final dimensions of the hexacopter	28
2.7	Octocopter frame	29
2.8	Thrust coefficient (a) and flight time (b) with respect to battery weight and for three payloads (1 kg, 1.5 kg, 2 kg); (c): eCalc results	31
2.9	eCalc results	32
2.10	Final dimensions of the octocopter	33
3.1	Omega VS Throttle	39
3.2	(a) PNPNP configuration; (b) NPPNP configuration	42
3.3	(a) PNPNPNP configuration; (b) PPNNPPNN configuration . .	44
3.4	Plane rotation	46
3.5	(a) Simulator of the hexacopter; (b) Simulator of the hexacopter and mixer	49

3.6	(a) Simulator of the octocopter; (b) Simulator of the octocopter and mixer	50
4.1	H_∞ synthesis scheme	52
4.2	Adopted scheme for controlling the attitude	54
4.3	Position closed loop block diagram	54
4.4	Adopted scheme for controlling the altitude	55
4.5	Sensitivity functions with associated weights on the roll angle . .	56
4.6	Sensitivity functions with associated weights on the pitch angle. .	57
4.7	Sensitivity functions with associated weights on the North control loop	58
4.8	Sensitivity functions with associated weights on the East control loop.	59
4.9	Sensitivity functions with associated weights on the altitude control loop	59
4.10	Sensitivity functions with associated weights on the yaw angle . .	60
4.11	(a) Position of the hexacopter; (b) Position error of the hexacopter	62
4.12	Velocity of the hexacopter	63
4.13	(a) Attitude of the hexacopter; (b) Yaw error of the hexacopter .	64
4.14	Angular speeds of the hexacopter	65
4.15	Motor thrusts of the hexacopter	65
4.16	Sensitivity functions with associated weights on roll and pitch angles	66
4.17	Sensitivity functions with associated weights on the North control loop and East control loops	67
4.18	Sensitivity functions with associated weights on altitude control loop	67
4.19	Sensitivity functions with associated weights on the yaw angle . .	68
4.20	(a) Position of the hexacopter; (b) Position error of the octocopter	70
4.21	Velocity of the octocopter	71
4.22	(a) Attitude of the octocopter; (b) Yaw error of the octocopter . .	72
4.23	Angular speeds of the octocopter	73
4.24	Motor thrusts of the octocopter	73
4.25	Overall simulator of the quadrotor	75
4.26	(a) Position of the quadcopter; (b) Position error of the quadcopter	76
4.27	Velocity of the quadcopter	77
4.28	Bode diagram on the North velocity control loop	77
4.29	Sensitivity functions with associated weights on the North control loop	78
4.30	(a) Position of the quadcopter after tuning; (b) Position error of the quadcopter after tuning	79
4.31	Velocity of the quadcopter after tuning	80
4.32	Absolute North traslational error due to the drift and for different values of σ_{RW} and σ_{RRW}	81

4.33	Absolute East traslational error due to the drift and for different values of σ_{RW} and σ_{RRW}	82
4.34	Absolute traslational error on the altitude due to the drift and for different values of σ_{RW} and σ_{RRW}	82
5.1	Active fault control scheme (see [1])	86
5.2	Digraph of a hexarotor	89
5.3	Control system using fault-tolerant control	92
5.4	Rotational speed of rotor number four	93
5.5	Position response of H_2	94
5.6	Attitude response of H_2	94
5.7	Throttles of H_2	95
5.8	Position response of O_1	98
5.9	Attitude response of O_1	99
5.10	Throttles of O_1	99
5.11	Position response of O_2	100
5.12	Attitude response of O_2	100
5.13	Throttles of O_2	101

List of Tables

1.1	Means and standard deviations	12
1.2	Monitoring systems from competitors	16
1.3	Customizable UAV platforms selected	17
2.1	Sizes and weights of devices to carry onboard	24
2.2	Actuator data.	26
3.1	Summary table of moments of inertia	48
4.1	Signals and transfer functions	54
4.2	Values of the regulators	61
4.3	Values of the regulators	68
4.4	Traslational errors respect to distance travelled given by VINS-MONO and SVO+MSF	80
5.1	Summary table of reconfigurable rotors for H_1 and H_2	91

Introduction

An unmanned aerial vehicle (UAV), is an aircraft without a human pilot aboard. Since the aircrafts piloted remotely, have become very diffused among the masses, the more simple word "drone" has substituted the acronym UAV. The idea of UVAs date back to the attacks of Austria on Venice during the 19th century using hot-air ballons loaded with bombs. Nowadays, drones have become more complex systems, used in different fields, from military implementation to hobbyist purpose. A very simple multicopter is composed by a Flight Control Unit (FCU) which transforms the commands taken by a receiver and the sensors, in inputs to the Electronic Speed Controller (ESC) of each motor. A battery pack supply the electronics, the motors and the sensors. Usually an IMU, a GPS receiver and a barometer are mounted on the platform. But, in general multiple sensors can be adopted depending on the mission. Furthermore, UAVs have been particularly applied to industrial monitoring sectors.

In this context, drones are particularly valuable for monitoring industrial structures and infrastructures (pipelines, electric power lines, etc.) in the oil-gas and utilities industries, allowing to make critical operational or maintenance decisions. For this purpose, these aircrafts are equipped with detection instruments able to reveal leakages of dangerous gases. Moreover, vision systems (which are computer based systems where software performs tasks assimilable to "seeing"), are mounted on the platform to provide position information when the aerial vehicle flies in areas not properly covered by the GPS signal.

Dealing with the preliminary design, the modelling, the control law design of UAVs sized to carry visual and detection systems, this thesis aims at contributing to different areas of the design process flowing from mission requirements to modelling and analysis of multicopters suited for the task of industrial monitoring and hazardous gas detection.

The first chapter of this thesis begins by presenting the flying platform, vision system and detection instrument requirements. Then a comparison study of the products available on the market is performed to find the best trade-off based on the requirements defined. In Chapter 2, the equations and the main objectives related to the sizing of multicopters are presented. Then, two frame structures (one hexarotor "H" shaped and one octocopter "X" shaped) are taken into account and the battery weight and actuators type are identified for both the multicopters.

Subsequently, in the third chapter, the approach used to characterize the actuators of the drones is described; in particular, the estimation of main aerodynamic coefficients is presented followed by the description of the reference frames and the implementation of the aerodynamical model of both the flying robots in Matlab Simulink (see [2]). In Chapter 4, a linear dynamical model around the hovering equilibrium of a general UAV is derived and used to compute the linear PID attitude and position regulators of both the hexacopter and the octocopter aerial vehicles, by the adoption of an H_∞ control synthesis. The linear controllers have then been tested on the non-linear dynamical models. In the end, Chapter 5 deals with the reconfigurability analysis to motors fult occurrence (see [1]) of the two multirotors (respect to the choice of the direction of rotation of the propellers) and the implementation, on the Simulink models, of the rotors speed reconfiguration system based on the Linear Virtual Actuator (LVA) technique.

Chapter 1

Requirements and technology review

This first chapter introduces the characteristics related to the development of an Unmanned Aerial Vehicle (UAV) for the monitoring and the inspection of industrial plants. Initially, the requirements related to the whole platform and the necessary devices are presented; then the basics of visual sensors and measurement/detection systems are pointed out. After that a comparison among different solutions existing on the market is described. Similar procedure is applied for the selection of the aircraft.

1.1 Mission and requirements

The main target the aircraft must perform is to fly inside an industrial plant following a defined path (chosen by the pilot) to reveal leakages and/or detect the presence of hazardous gases in areas difficult to approach by human operators. To accomplish the task, a gas measurement/detection instrument and a visual system has to be mounted on the drone.

Given this premise, the choice of platform and devices shall be based on the following requirements and parameters:

- Vision sensing system
 - Number and types of sensors
 - Frames per second and maximum frequency
 - FOV (field of view)
 - Dimensions
 - Ease of use
 - Price

- Aircraft
 - Customizable control system
 - Flight hovering time about 20 min
 - Diameter smaller than 1.2 m (propellers not included)
 - Maximum take-off weight about 8 kg - 8.5 kg
 - Possibility to integrate payloads up to 2 kg
 - Motor redundancy greater than four (at least hexacopters)

- Gas detector
 - Long range of detection
 - Multi-gas

1.2 Vision systems

Artificial vision devices are useful sensors because they mimic the human sense of sight and allow us to gather information from the environment without being in direct contact with it.

For this purpose and because the aircraft would fly in covered areas with absence of GPS signal, it is necessary to integrate on the machine a 3D camera. This device will substitute the GPS, retrieving visual measurements which shall be used in a real time feedback loop to improve the control of the UAVs position .

In the next subsections the main functionings of a general monocular camera are introduced and used to give a general description of Stereocameras.

1.2.1 Camera: mathematical description

A camera is a device that can measure the intensity of light, concentrated by a lens on a plane (the image plane) which contains a matrix of pixels. This is possible thanks to a charge coupled device (CCD) which is an integrated circuit that turns the photons incident on its surface into a digital copy of the light patterns, the pixels. The light can be “captured” in terms of:

- Intensity only (gray scale)

- Intensity and spectral components (RGB scale)

In the gray scale, each pixel describes with a certain number of bits the scale of gray from white to black; in RGB three light beams (one red, one green, and one blue) must be superimposed. Each of the three beams is called a component of

that color, and each of them can have an arbitrary intensity, from fully off to fully on, in the mixture.

A monocular camera performs a 2D projection of the scene. A 2D projection can be performed with different methods but in this context only *perspective projection* is considered.

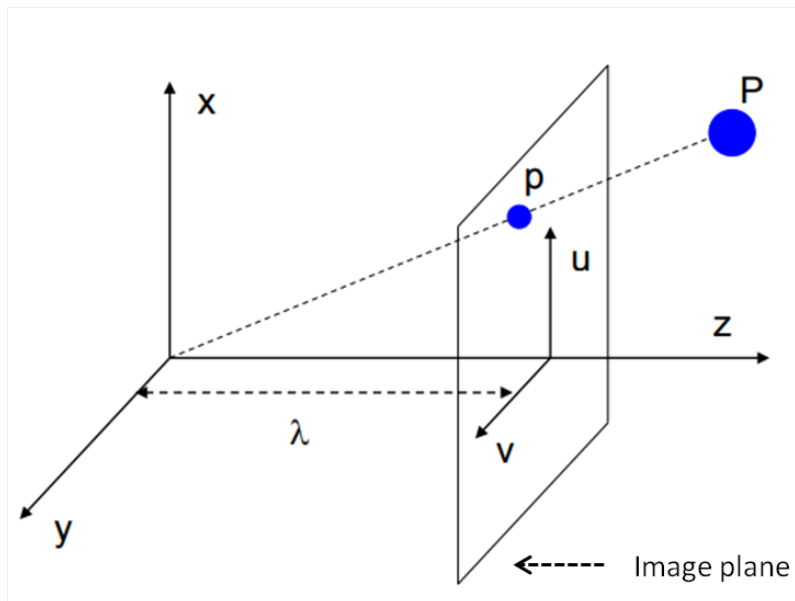


Figure 1.1: Perspective projection of a 3D point P on the image plane

A point "P" with coordinates (X, Y, Z) in the camera frame (Figure 1.1) is projected into a point "p" with coordinates (u, v) in the image plane, expressed in pixels. Denoting with λ the focal length (distance between the centre of a lens and its focus), from similarity of triangles we have that:

$$\frac{\lambda}{Z} = \frac{u}{X}, \quad \frac{\lambda}{Z} = \frac{v}{Y}. \quad (1.1)$$

This can be rewritten as:

$$\xi = \begin{bmatrix} u \\ v \end{bmatrix} = \frac{\lambda}{Z} \begin{bmatrix} X \\ Y \end{bmatrix}. \quad (1.2)$$

The camera performs a 2D projection of the scene. This projection entails a loss of depth information; indeed, each point in the image plane corresponds to a ray in the 3D space.

In order to determine the 3D coordinates of a point corresponding to a 2D point in the image plane a different approach is needed.

1.2.2 Stereo camera: model

A stereo camera is a type of camera with two or more lenses with a separate image sensor or film frame for each lens. This allows the camera to simulate the human binocular vision, and therefore gives it the ability to capture three-dimensional images. This process is known as stereo photography.

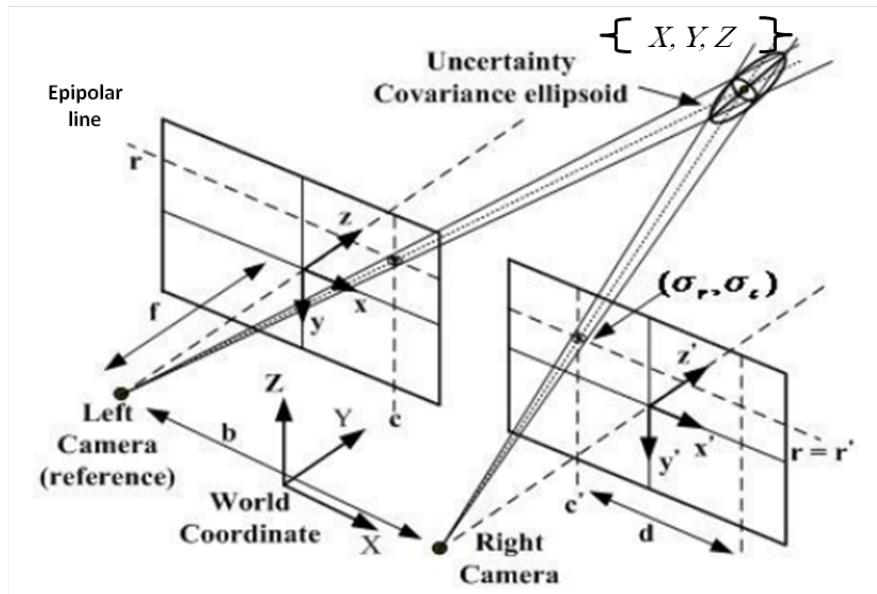


Figure 1.2: Stereo vision model

A 3D vision system is completely characterized through *intrinsic* and *extrinsic* parameters. The first ones (focal length, pixel distortion, pixel shape, etc...) allow to define the correspondence between a 3D point in space and its coordinates on the image plane of each camera. The second ones give the position and the orientation of each camera with respect to a reference frame.

These parameters can be determined with a calibration procedure which permits to perfectly describe a stereoscopic system.

In Figure 1.2, the ideal geometry of stereo vision systems is depicted:

- The optical axes of left and right camera, are parallel
- The optical axes are separated by the baseline b
- The distance of both cameras from their image planes is equal to the focal length f
- The epipolar lines fall along the horizontal direction on the image planes

- Disparity d is the amount by which the two projections of the 3D point on the image planes are displaced relative to each other

1.2.3 Analysis and comparison of stereo cameras

While in the previous paragraph a geometric description of stereo cameras behaviour has been showed, in this section the main parameters shall be marked out.

Stereo visual devices use visual odometry algorithms to track camera motion in 3D space and get position and orientation up to a certain maximum frequency. Also, a 3D camera produces a 3D map of the environment around up to a maximum depth and with a specific frame rate, FPS (frames per second). Both frequency and frame rate are important variables; indeed, the first one gives a measure of the speed of the system, while the second one gives a quantitative information about the number of frames built (per second).

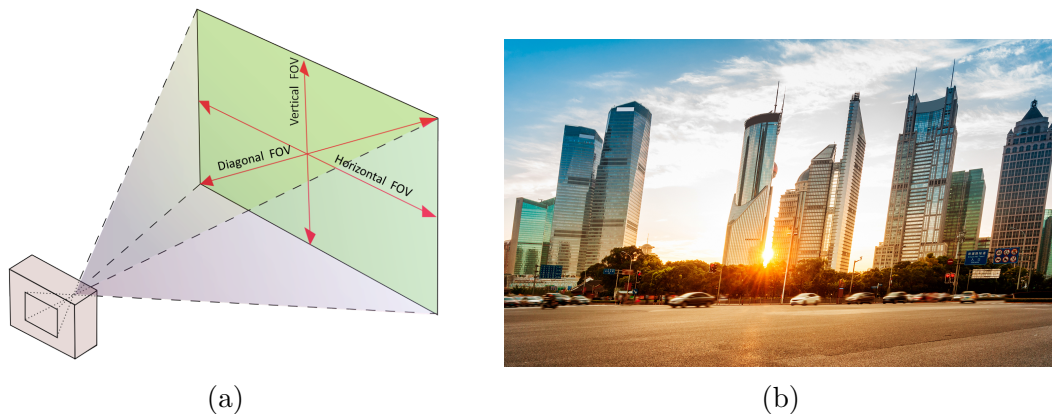


Figure 1.3: (a) Diagonal, vertical and horizontal field of view; (b) Jello effect

Another important consideration is about the FOV (field of view); it is the inspection area captured on the camera sensor at any given moment. FOV is measured (diagonally, horizontally and vertically as in Figure 1.3a) in degrees and its size (as image sensor one) directly affects the resolution.

Moreover, the type of image sensor has to be taken into account in the choice. As a matter of fact, the image sensor can be of two types:

- rolling shutter
- global shutter

If the sensor employs a *rolling shutter*, the image is scanned sequentially, from one side of the sensor (usually the top) to the other, line by line. Hence, the faster the movement of the camera (and so of the aircraft), the more the scene acquisition might be degraded taking on an appearance akin to gelatin. As a consequence, depth measures and position information might be affected. This phenomenon is known as *jello effect* (Figure 1.3b).

In contrast to that, *global shutter* is the technical term referring to sensors that scan the entire area of the image simultaneously, avoiding the arising of jello.

Taking into account the details just exposed and considering the products available on the market, the following comparison has been performed, (see Figure 1.4).

	Stereolabs	Duo3d	E-con system	Intel	Parrot	DJI
Model	ZED	Duo Mix	Tara	RealSense ZR300	Dunk	Guidance (includes 5 vision sensors)
FPS and resolution	100FPS at 1344x376	192FPS at 640x120	60FPS at 640 x 480	60FPS at 628 · 468	120FPS at 900 x 700	20FPS at 640x480
DOF	6	6	6	6	6	6
Depth	0.5-20m	/	0.5-30m	0.5-2.8m	0.1-15m	0.20 - 20 m
Single sensor size	1/3"	1/3"	1/3"	1/3"	1/4"	1/3"
FOV (D)	110°	170°	60°	166°	120°	360°
Dimension (LxHxW) mm	175 x 30 x 33mm	52x25x13mm	100 x 30 x 35mm	130x20x7mm	220 x 150 x 30mm	200 x 20 x 200mm
Weight	159g	12.5g	80.5g	/	140g	337g
Frequency	100Hz	250Hz	60Hz	/	60 Hz	20Hz
Shutter sensor	Rolling	Global	Global	Rolling	Rolling	Global
USB	3.0	Micro 2.0	3.0	3.0	3.0-Micro 2.0	OTG 2.0
Ultrasonic Sensors	NA	NA	NA	NA	Up to 15m	Yes
Embedded Processor	NA	NA	NA	NA	Nvidia TK1	Guidance Core
Price	\$449	\$625	\$249	\$289	\$1 119	\$999
						

Figure 1.4: Paralleling of stereo vision systems

It can be noted that, whereas the first four devices (depicted in Figure 1.4) are stereo cameras, the last two (*DJI Guidance* and *Parrot SLAM dunk*) are vision sensing systems. Precisely, both of them include ultrasonic sensors for obstacle avoidance and are equipped with an embedded computer for real-time data processing. In addition, the Guidance system includes five stereo vision sensors (disposed on a quadratic structure where one of them is directed to the floor) connected to the embedded processor, ensuring a FOV up to 360°. Hence, considering the target of assembling an UAV platform able to safely fly in a risky environment, among the selected products Guidance has turned out to be the best trade off for its dimensions, performance, ease of use and price.

1.3 Measurement and detection instruments

Industrial gases are used in a wide range of industries, which include:

- Oil and gas: The most obvious and significant threat is the leakage and combustion of explosive gas. Operators are constantly faced with the risk of flammable and toxic gas release and exposure.
- Winery: Common gas hazards in wineries and breweries are carbon dioxide from fermentation, argon and nitrogen used to create inert atmospheres.
- Steelmaking: There are many different processes employed in making and forming steel and each stage generates and uses potentially hazardous gases.

Depending on the specific sector, the spectrum of gas hazards produced changes drastically, and so the respective detection instruments. Therefore, in order to choose the most suitable device, the attention has been centered on a particular industrial sector.

1.3.1 Instruments analysis and comparison

Henceforward, the focus will be oriented on gas hazards in the field of petrochemical industry.

Both flammable and toxic gases pose serious hazards in petrochemical plants. In this context, the portable gas detectors suitable (in terms of dimensions and weight) for an onboard drone mounting can be listed as follows:

- Diffusion multi gas detector
- Laser (monogas) detectors
- Optical gas imaging (OGI) instruments.

Before continuing the analysis, it must be underlined that the rotation of the propellers of the aircraft may cause perturbations in the atmosphere, altering the concentration of gases. Therefore, the onboard monitoring device must be a long-range one (as specified in the requirements in Section 1.1). Diffusion instruments can detect a broad range of gases (from carbon monoxide (CO) to flammable gases), and can also include infrared sensors or PID (Photo Ionization Detection) technology for measuring methane or VOCs (Volatile Organic Compounds) concentration, respectively.

They are devices of small sizes, with a typical weight under 400 g, and able to measure and display the gases concentration (in part per million, ppm).

Despite the small dimensions and detection capabilities, these systems have been excluded because they are able to make measurement only in proximity of the gas cloud.



Figure 1.5: Diffusion detector example

The second type of inspection apparatus considered for this application is a long-range portable detector which allows methane gas to be detected at distances of up to 30 m. This technology is used to find where methane leaks are located by pointing the laser beam towards the suspected leak and then detecting a fraction of the diffusely reflected beam from that target point. Sizes and weight are comparable to those of diffusion detectors.



Figure 1.6: Laser detector example

In this case, a question has raised regarding the precision of a laser targeting system mounted on a drone. Consequently, a test has been run (see Section 1.3.2) to estimate the order of magnitude of the laser deviation from a target point. In conclusion, OGI (Optical Gas Imaging) cameras can detect hundreds of industrial gases (methane, sulfur hexafluoride, etc...) allowing scanning broad sections of equipment rapidly and surveying areas that are hard to reach with traditional contact measurement tools. OGI cameras can also detect leaks from a safe distance, displaying these invisible gases as clouds of smoke. Therefore, these instru-



Figure 1.7: Example of an infrared thermal camera for gases detection

ments can only detect the presence of gases, but not display their concentration. The dimensions usually depend on the particular gas spectrum to be identified and the weight can vary from 1 kg to almost 2 kg.

1.3.2 Laser targeting system precision

In this Subsection the precision of a laser targeting system mounted on a drone will be studied.

Assembling

The experiment has been performed in a closed environment with optimal lighting and with the support of a vision system (Optitrack) made of six cameras fixed on the cage where the test has been executed. The working sampling rate of the vision system is 30 Hz and its accuracy is in the order of millimeters. The test has been run mounting a laser pointer on a 2-axis gimbal. The calibration of the gimbal has been accomplished adding small weights on it. The result of this assembling has then been mounted on hexacopter (Hexa2)(see Figure 1.8).

Test

The drone has been piloted until reaching a position-holding configuration with the laser pointed to the center of a graph paper attached to the wall. Then, video results of the movements of the laser point on the paper have been compared with the standard deviations of attitude and position of the drone. The 3D trajectory of the hexarotor respect to an Earth reference system (North-East-(-Down)) is depicted in Figure 1.9. On the upper part of the image the movements of the drone around the set point position are shown.

Since the gimbal is a two axis one, pitch and roll motions are compensated; therefore the only interesting component (in terms of laser-targeting precision) is the yaw motion. In Figure 1.10 the yaw component fluctuations around the set-point is shown.



Figure 1.8: Laser targeting system mounted on Hexa2

The computation of means and standard deviations have been made up when the aircraft is in the reference position. Also, in order to isolate the trajectories of the drone in the neighborhood of the set point, only the measurements related to this condition have been considered. Table 1.1, summarises the values of mean and standard deviations obtained.

	Mean (\bar{p})	Standard Dev. (σ)	Unit
North	0.525	0.0162	m
East	-0.773	0.0165	m
-Down	1.618	0.0102	m
Yaw	1.55	0.0103	°

Table 1.1: Means and standard deviations

Projecting the 3D data (centered in neighborhood of the set point) on the North-(-Down) plane, Figure 1.11 has been obtained. Since the North-(-Down) plane corresponds to the paper's plane, the values of standard deviations along the North and -Down axes can be seen as deviations of the laser point from its center. In other words, the fluctuations of the aircraft in the neighborhood of its reference give a quantitative information about the deviation of the laser point from the paper center. Indeed, the x-axis of the graph paper is aligned with the North-axis of multicopter's Earth system and the y-axis to the Down-axis of the Earth reference system.

In order to add the contribution of the yaw component to the deviation along the x-axis, the mean distance of the aircraft from the wall has been evaluated. The distance of the Earth reference system from the wall (along East-axis) is

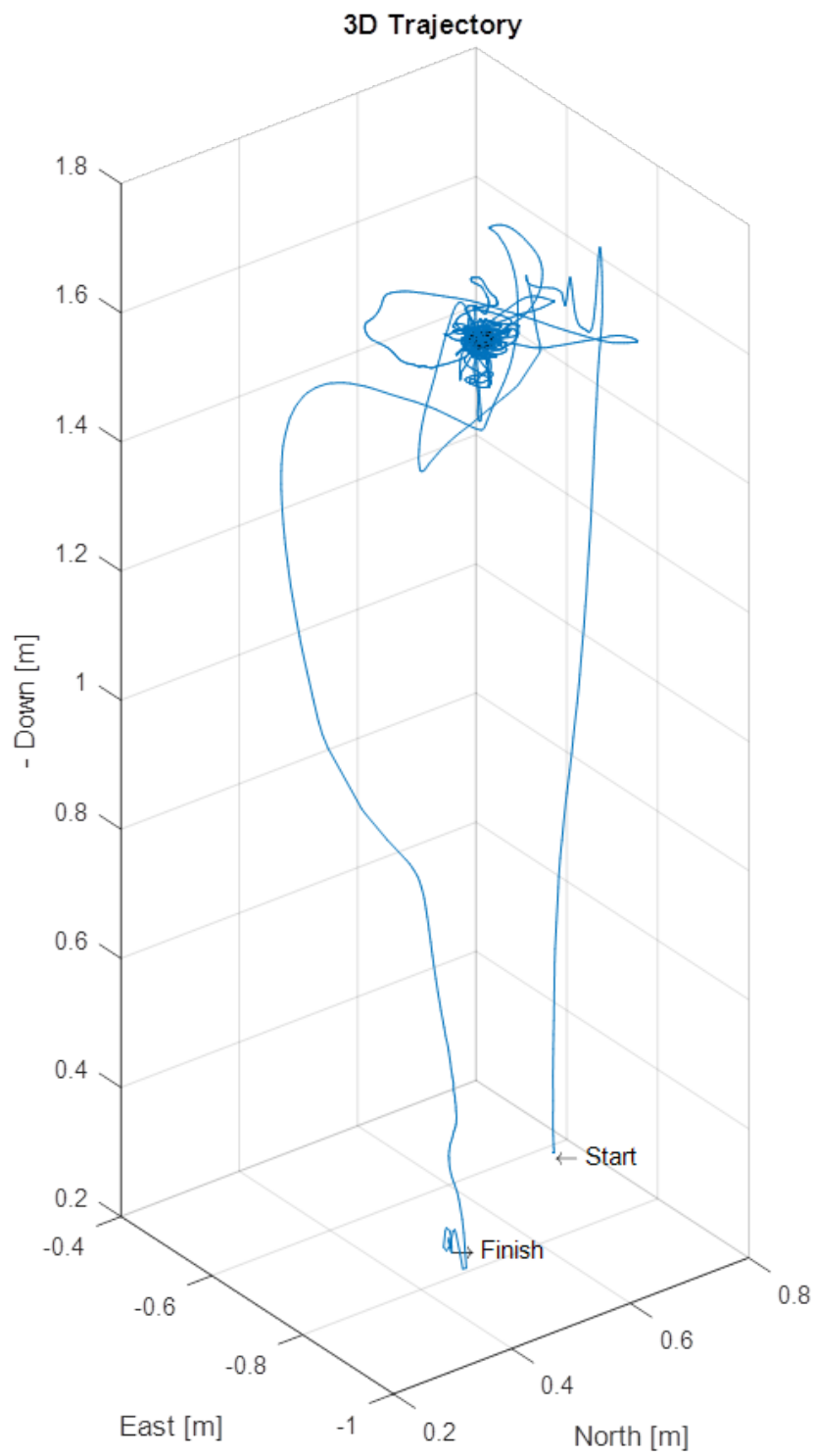


Figure 1.9: 3D trajectory performed by Hexa2

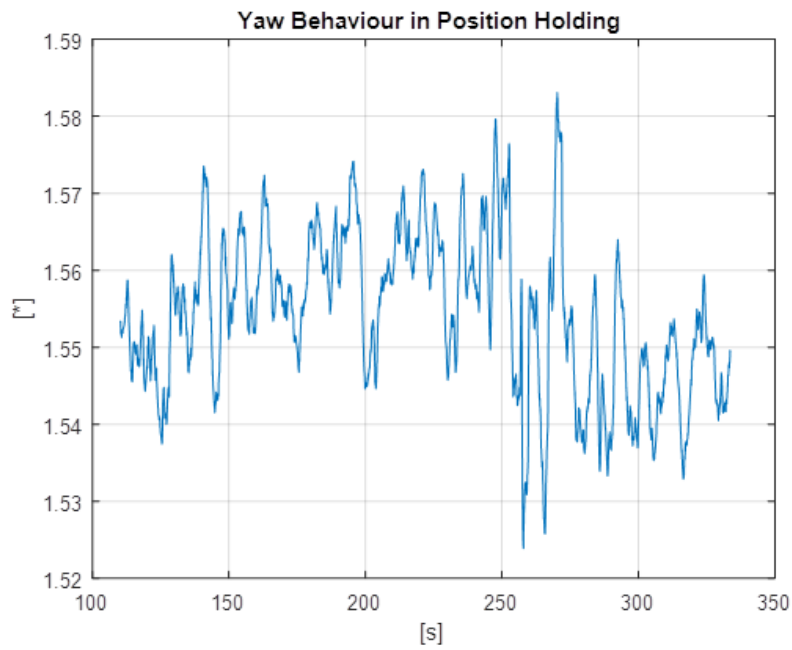


Figure 1.10: Yaw motion in position holding

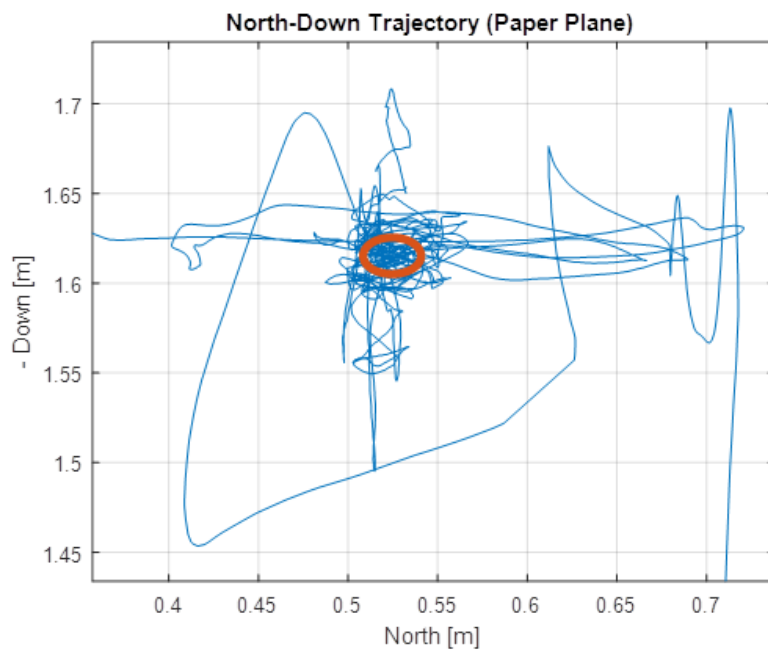


Figure 1.11: North-(-Down) plane

$d_{WRE} = 2.49m$; so the mean distance is:

$$d_{DE} = d_{WRE} - \bar{p}_{DE}, \quad (1.3)$$

where \bar{p}_{DE} is the mean of the positions around the set point in East direction (see Table 1.1). Therefore, the contribution of the yaw component to the deviations is:

$$\sigma_{Yaw} = d_{DE} \cdot \sigma_{\Psi} = 0.0336 m, \quad (1.4)$$

with σ_{Ψ} the standard deviation of the yaw motion (from Table 1.1). The video images of the experiment have suggested that the laser point fluctuations around the paper center are (for the most of the time) inside an ellipse of horizontal radius (along the x-axis of the paper and North-axis of the Earth reference) equal to 0.06 m, and vertical radius (along the y-axis on the paper and Down-axis of the drone) equal to 0.04 m. Thus, the following equations have been obtained:

$$\begin{aligned} \sigma_x &= \sqrt{\sigma_{Yaw}^2 + \sigma_N^2 + e_{g_x}^2} = 0.06 m, \\ \sigma_y &= \sqrt{\sigma_D^2 + e_{g_y}^2} = 0.04 m. \end{aligned} \quad (1.5)$$

Where e_{g_x} and e_{g_y} are compensation factors which take into account the fact that the response of the gimbal is not immediate. Indeed, the instant of time at which the drone moves does not coincide to the one at which the gimbal reacts. Therefore, as the response of the gimbal becomes slower, the values e_{g_x} and e_{g_y} will be higher.

Conclusions

In view of the test results it is possible to deduce that:

- As the axial distance of the drone from the target increases, the laser-targeting precision decreases;
- Better results would be achieved with a 3-axis gimbal, compensating yaw component.
- The hypothesis of a feedback loop for the laser pointer is excluded because of the complexity of the task
- The test has been run in ideal conditions managing to achieve a precision of the laser-targeting in order of centimeters. The Guidance system has an accuracy of centimeters (ten times greater than Optitrack one) at 20 Hz. Also, it shall be mounted on the aircraft and would work outdoor in worse lighting conditions. Hence, according to the results obtained, the precision of a laser-targeting system coupled with the Guidance, will be in the order of decimeters, in the best case.

- For the above considerations, laser detectors have been put aside preferring to focus on an OGI device.

1.4 Platform selection

Firstly, in order to build a competitive UAV monitoring system, a market scouting of already developed drones for fugitive emissions detection has been performed. Table 1.2 summarises the results:





	SyeEye		General Electric	Pergam
<i>Model</i>	Mammoth	Prime	Raven	LMC
<i>N° Rotors</i>	6 (Coaxial)	6 (Coaxial)	4	4
<i>Diameter [m]</i>	1.38	1.02	/	0.6
<i>Weight [kg]</i>	10	8	/	3
<i>Max flight time [min]</i>	/	/	40	50
<i>Max payload [kg]</i>	4.5	1.5	/	/
<i>Detector</i>	OGI camera	OGI camera	Laser methane	Laser methane
<i>Positioning</i>	GPS	GPS	GPS	GPS
				

Table 1.2: Monitoring systems from competitors

Note: Not all the data are provided by the manufacturers.

It is possible to note that, not many companies are involved in this branch of the market. Furthermore, Sky Eye systems are very different from the General Electric and LMC ones, in terms of dimensions and total weight; but also, they are more close to the requirements underlined at the starting of the chapter.

Secondly, based on the requirements previously listed, it has been performed a market scouting of existent customizable platforms suitable for the goal which has been set.

Although many options have been sifted through, the Table 1.3 recaps the closest matches. As can be observed, all three drones are very similar in terms of performances and size, but none of them perfectly satisfies the requests because of their dimensions, oversized take-off weight and payload lifting capacity. Then it has been decided to follow a different approach and realize a custom platform.




	DJI	Freefly	
<i>Model</i>	Matrice 600	Alta 6	Alta 8
<i>N° Rotors</i>	6	6	8
<i>Diameter [m]</i>	1.13	1.12	1.32
<i>Empty [kg]</i> <i>Weight</i>	5.3	4.5	6.2
<i>Batteries [kg]</i>	4.2 (6s 34A)	2.5 (6s 24A)	2.5 (6s 24A)
<i>Flight time [min]</i> <i>with 2kg payload</i>	24	26	20
<i>Max payload [kg]</i>	6	6.6	9.4
<i>Positioning</i>	GPS	GPS	GPS
			

Table 1.3: Customizable UAV platforms selected

Chapter 2

Preliminary drone design

As reported in the previous chapter, none of the platforms identified in the market study has fully satisfied the requirements. Therefore, a new way consisting in developing a custom platform suited for executing monitoring missions, has been considered.

In this chapter the problem of defining the base structure (from frame shape selection to propulsion system choice) of an unmanned aerial vehicle, able to carry a vision system and an OGI camera, will be discussed.

2.1 Methodology

In this section the guidelines of a drone design project will be treated. Particularly, the focus will be pointed on the methods used to find the right propulsion system (actuators and batteries), in order to ensure the best trade-off among requirements, design parameters and final platform dimensions.

2.1.1 On-board energy storage

The type of on-board energy storage influences flight time, for this reason three different kinds of energy systems storage have been initially considered in this work:

- New lithium metal batteries
- Hydrogen fuel cells
- LiPo (Lithium Polymer) batteries.

Lithium metal batteries use lithium metal for the negative electrode of the battery. Even though they can have an energy density (per unit of mass) of 450 Wh/kg, much higher respect to hydrogen fuel cells (300 Wh/kg) and LiPo (180 Wh/kg), to date they are just prototypes not available on the market.

A fuel cell is an electrochemical cell that converts the chemical energy from a fuel into electricity. Because of the presence of hydrogen, the employment of fuel cells has turned out to be excessive dangerous in this context. In conclusion, only LiPo batteries have been taken into account in the design.

2.1.2 Actuators and speed controllers

The considered motors examined are brushless DC motors (BLDC). BLDC motors are powered by an inverter that switches the DC voltage to a DC switching electric signal. These inverters are also known in rc-models as ESCs (Electronic Speed Controllers). To generate the aerodynamic thrust force a propeller is needed. The propellers on multicopters have to rotate in opposite directions in order to balance the generated moments (if N_r is the number of rotors, $\frac{N_r}{2}$ propellers rotate clockwise and $\frac{N_r}{2}$ propellers counter-clockwise). The main parameters of BLDC motors are the K_v parameter (which is a coefficient that represents the number of revolutions per minutes (rpm) for each Volt applied) and the maximum thrust force they can develop.

Commercial propellers are defined by the number of blades, diameter and pitch. Each couple motor-propeller can develop a specific maximum vertical propulsion force also called *maximum thrust force* (T_{max}). This value is usually expressed in kilograms or Newton. Commonly, multicopters are sized so that the product of the number of rotors (N_r) and the thrust force of each rotor at 50% ($T_{50\%}$) is almost equal to the desired maximum take-off weight ($MTOW$). For this reason the actuators choice has been bounded to the sets of motors and propellers able to produce thrusts at 50% ($T_{50\%}$) almost greater than (or equal to) the maximum take-off weight required.

2.1.3 Sizing

The first part of the project has been centered on defining the main design paramaters:

- Maximum take-off weight ($MTOW$) [kg]
- Rotors number (N_r)
- Payload (m_{Pay}) [kg]

Then, once chosen the actuator, the following quantities have been computed:

- Hovering power (P_{hov}) [W]
- Dry weight (m_{dry}) [kg]
- Battery weight (m_{bat}) [kg]

- Flight time (t_{fly}) [s]

Where the hovering power (P_{hov}) is the sum of the power absorbed by electronics (FCU, vision systems) and motors in Watt. The power developed by the motors is given by:

$$P_{mot} = \frac{T_{hov} N_r}{c_{pl}}, \quad (2.1)$$

where the T_{hov} term corresponds to the thrust at 50% (T_{50}) that each rotor should provide in hovering condition in kilograms; The c_{pl} coefficient is the power load coefficient of the actuator measured in kg/W . The power coefficient is a measure of the efficiency of the motors.

The dry weight is the mass (m_{dry}) associated to motors (m_{mot}), propellers (m_{prop}), frame, electronics (m_{el}) and ESCs (m_{ESC}) computed as:

$$m_{dry} = (m_{mot} + m_{ESC} + m_{prop}) N_r + m_{fr} + m_{el}, \quad (2.2)$$

with m_{fr} the hypothesized mass of the frame. Then, the recommended battery weight (m_{bat}) is estimated by the difference between the $MTOW$ and the sum of dry weight and payload (m_{Pay}):

$$m_{bat} = MTOW - m_{dry} - m_{Pay}. \quad (2.3)$$

So, the flight time associated with the specific propulsion system is:

$$t_{fly} = \frac{U_{LiPo} m_{bat} 60}{P_{hov}} 0.7, \quad (2.4)$$

with U_{LiPo} the energy density of a general LiPo 6S (six cells in series).

Notice that an energy consumption up to 70% of the available energy is assumed. Then, the *thrust over weight coefficient* is defined as the ratio between the sum of dry weight, battery weight, payload, and the maximum thrust (T_{max}) given by the N_r motors:

$$c_{Th} = \frac{m_{dry} + m_{bat} + m_{Pay}}{N_r T_{max}}. \quad (2.5)$$

This coefficient represents the percentage of total thrust used. In other words, given a specific payload and battery, it is possible to compute the propulsion force that the actuators would provide, in that particular situation. Thus, it is possible to evaluate if the aircraft hovers with a thrust greater or lower than the threshold (50%).

Similar considerations can be produced for flight time, too.

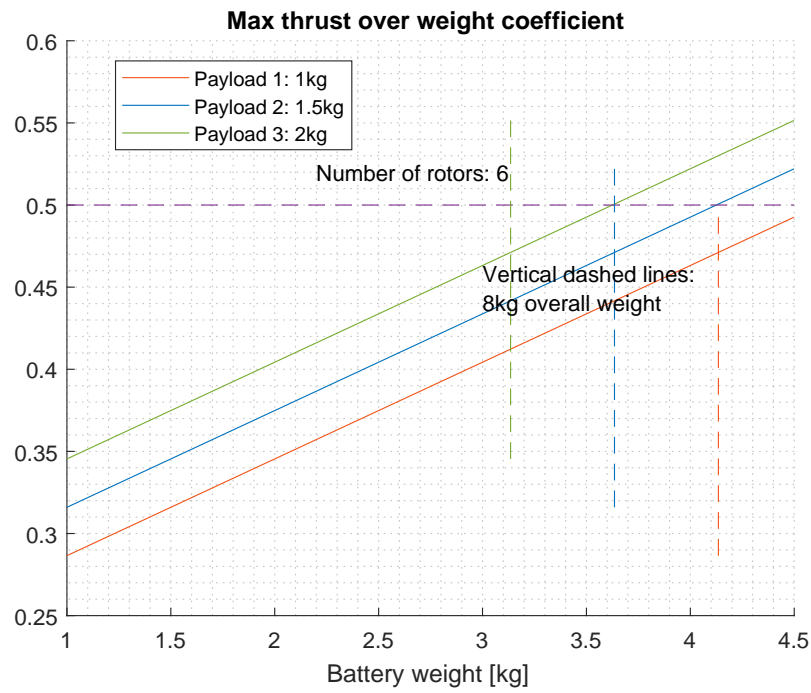
Subsequently, equations (2.6) have been computed (with P_{el} the power absorbed by the electronics) in order to show the dependency of the flight time from battery weight and power load coefficient. Furthermore equations (2.5) and (2.6) allow to

draw Figures 2.1a and 2.1b respectively, which depict the dependency of the *thrust over weight coefficient* and *flight time*, from battery weight. It is evident that, for a fixed payload value, increasing the capacity of the battery (and so its weight), the *thrust over weight coefficient* linearly raises and so more thrust is needed (equation (2.5)).

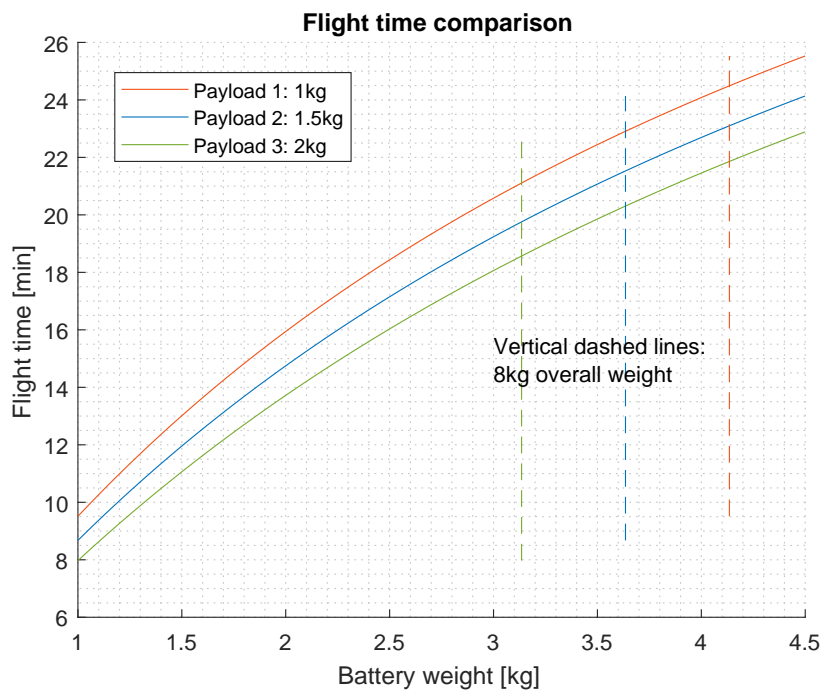
Note: the vertical dashed lines pictured in Figures 2.1a and 2.1b define the points (as intersection with the respective curves) where the overall weight of the multi-copter coincides with the *MTOW*.

While the flight hovering time increases according to equation (2.6); which differs from equation (2.4) since the power provided by the motors is computed using the two variables, battery mass (m_{bat}) and payload (m_{Pay}).

$$\begin{aligned}
 P_{mot} &= \frac{(m_{dry} + m_{bat} + m_{Pay})}{c_{pl}}, \\
 t_{fly} &= \frac{U_{LiPo} \cdot m_{bat} \cdot 0.7}{P_{mot} + P_{el}} 60.
 \end{aligned}
 \tag{2.6}$$



(a)



(b)

Figure 2.1: Examples of thrust coefficient (a) and flight time (b) with respect to battery weight and for three payloads (1 kg, 1.5 kg, 2 kg), in a hexacopter

2.2 Results

In this Section the results of the sizing procedure, taking into account two types of multirotors (hexacopter and octocopter), will be presented. Although many combinations of motors and propellers (from different manufacturers) have been evaluated, only the ones which revealed to be the best fit respect to requirements and design parameters will be pointed out.

2.2.1 Parameters and requirements

Some important requirements listed in Chapter 1 are recalled below:

- MTOW about 8 kg - 8.5 kg
- Number of rotors greater than four
- Payload up to 2 kg
- Flight hovering time close to 20 min

<i>Model</i>	Guidance	Manifold	OGI Niatros
<i>Dimension</i> [cm]	20 x 2 x 20	11 x 2.6 x 11	15 x 7 x 6
<i>Weight</i> [kg]	0.337	0.197	1

Table 2.1: Sizes and weights of devices to carry onboard

In Table 2.1, a possible choice of an OGI camera able to detect methane, and hundreds of industrial gases, is made. Note that, this is not the final choice, but it only gives the usual dimensions of these systems and the guidelines for the definition of the sizes of the plate. Besides detector and visual system, a high-performance embedded computer (DJI Manifold) has been added.

As previously mentioned, the weights of Guidance, Manifold and FCU (the FCU weighs 0.150 kg) have been merged together in the variable (m_{el}), while the OGI system is considered as part of the payload.

2.2.2 Hexacopter sizing

The shape of the frame (pictured in Figure 2.2) has been designed, in order to easily place on its plate the needed devices. Also, the mass of the frame has been estimated at 0.600 kg.

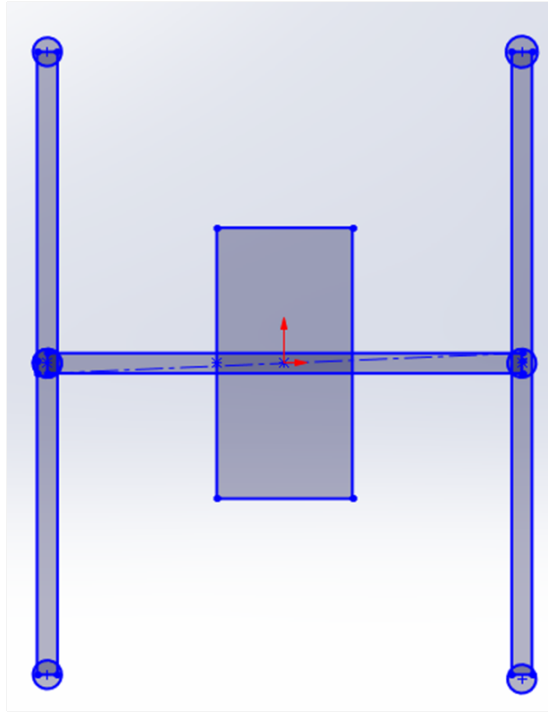


Figure 2.2: Hexacopter frame



Figure 2.3: T-Motor MN3515 KV400

The selected motor (Figure 2.3) is a T-Motor MN3515 KV400 with propellers of 16×5.4 inch and 40 A ESC. The total weight of each actuator is 0.260 kg and the required voltage is 22.2 V.

More technical data (from the motor datasheet) are reported in Table 2.2:

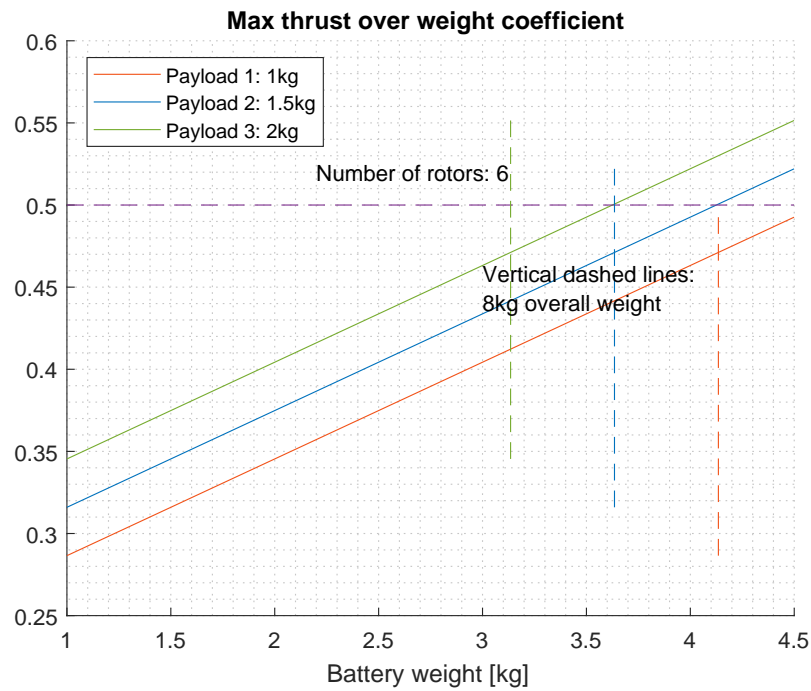
T-Motor MN3515 with 16×5.4inch proeller and 40 A ESC				
<i>Power (W)</i>	<i>Throttle</i>	<i>Thrust (N)</i>	<i>Speed (rad/s)</i>	<i>Efficiency (kg/W)</i>
115.44	50%	11.58	424.11	0.0102
208.68	65%	16.97	507.89	0.00829
288.60	75%	20.60	565.49	0.00728
375.18	85%	25.80	612.61	0.00701
444.00	100%	27.76	654.60	0.00637

Table 2.2: Actuator data.

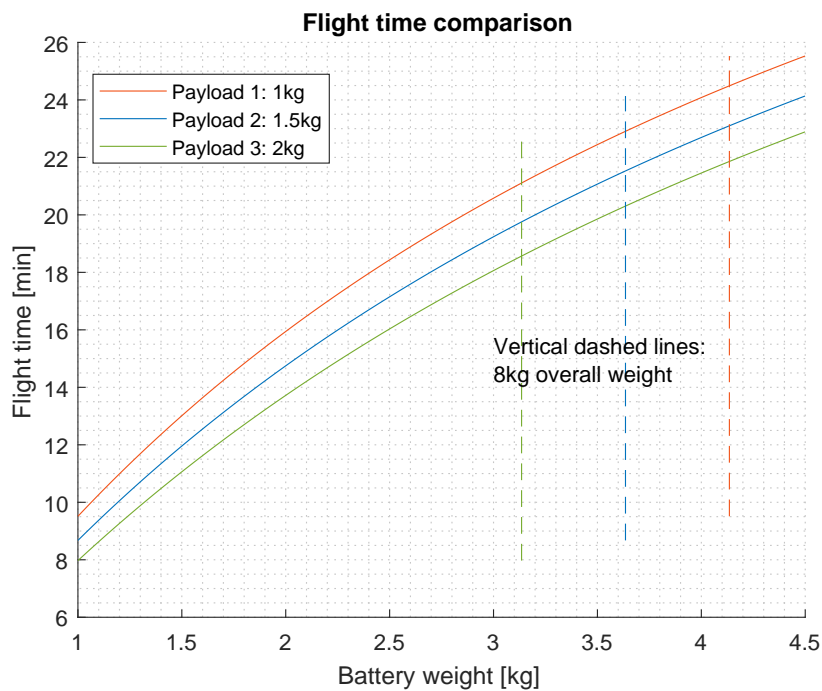
Applying the ideas reported in Section 2.1, the following results have been obtained. Then a comparison analysis has been performed with the support of a multicopter calculator (*eCalc*), in order to check the correctness of the computations:

- Hovering power: 1302 W
- Take-off weight: 8 kg
- Dry weight: 2.865 kg
- Payload: 2 kg
- Flight hovering time: 18.6 min
- Battery weight: 3.135 kg

From Figure 2.4a it is possible to understand that the thrust over weight coefficient remains under the threshold (0.50) as long as the take-off weight does not exceed the desired value (8 kg). Furthermore, decreasing the payload in favour of the weight of the battery, the flight time can be increased (Figure 2.4b). In conclusion, comparing these quantities with those computed with eCalc (Figure 2.5), it is possible to assert that the sizing has been accomplished correctly.



(a)



(b)

Figure 2.4: Thrust coefficient (a) and flight time (b) with respect to battery weight and for three payloads (1 kg, 1.5 kg, 2 kg)

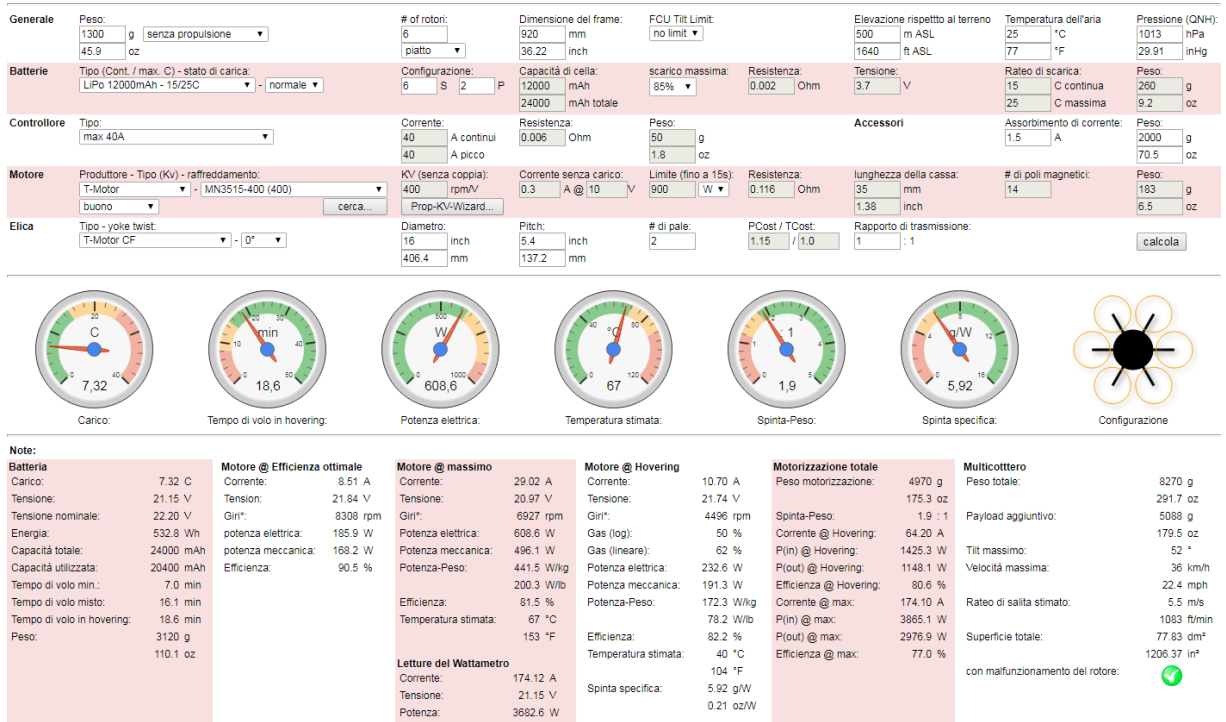


Figure 2.5: eCalc results

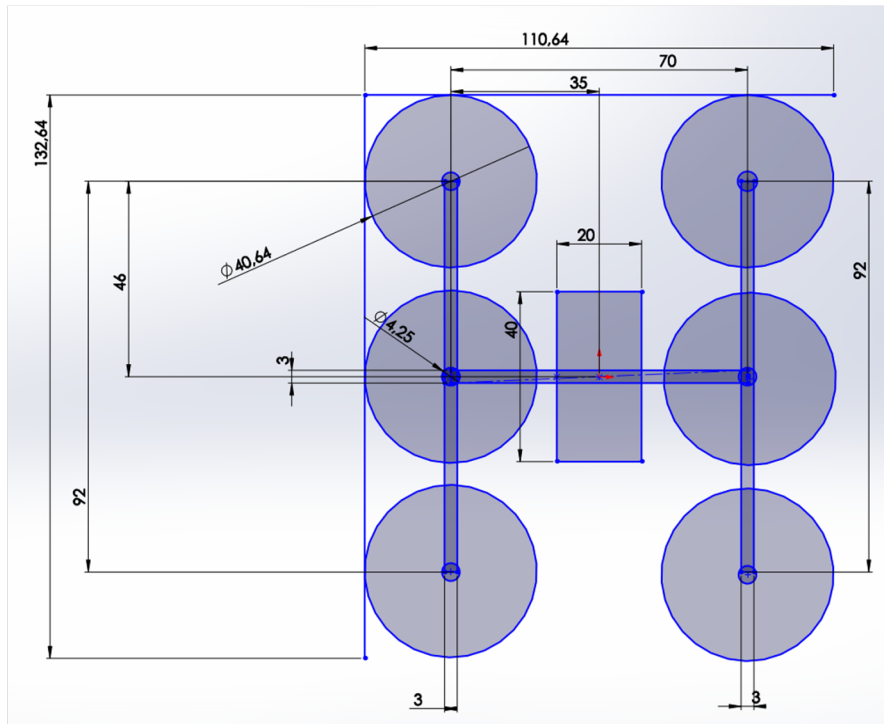


Figure 2.6: Final dimensions of the hexacopter

The dimensions of the drone are shown in Figure 2.6 in centimeters.

Note that the sizes of the plate ensure enough space for devices and batteries.

2.2.3 Octocopter sizing

The octorotor (see Figure 2.7) enables a more omogeneous distribution of propulsion forces when maneuvering. Moreover, the same actuators of the previous case, have been implemented, in order to compensate the heavier frame (0.800 kg) weight and to guarantee (for a take-off weight equal to 8.5 kg) values of thrust over weight coefficient smaller than 0.45. The reason behind the choice of this threshold (lower than the hexacopter one) will be better discussed in Chapter 5 and regard the idea of ensuring smaller thrust values when a fault occurs and the rotational speeds of the multicopter are reconfigured.

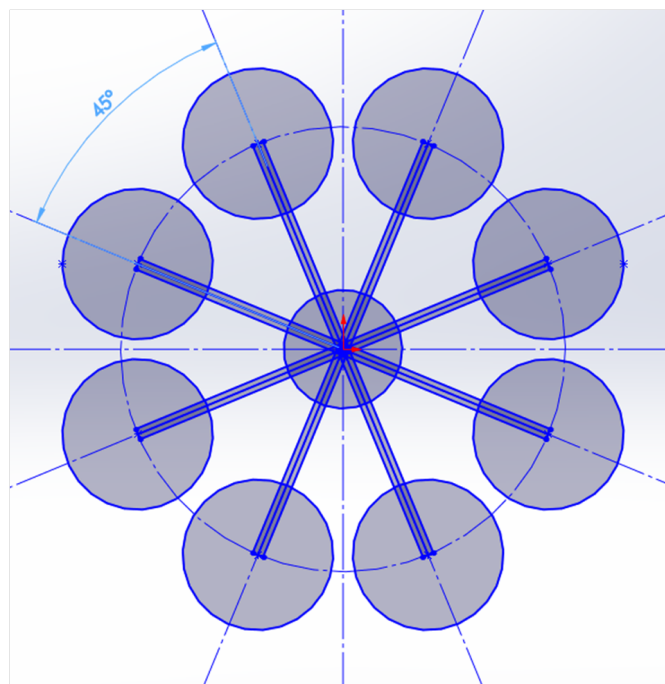


Figure 2.7: Octocopter frame

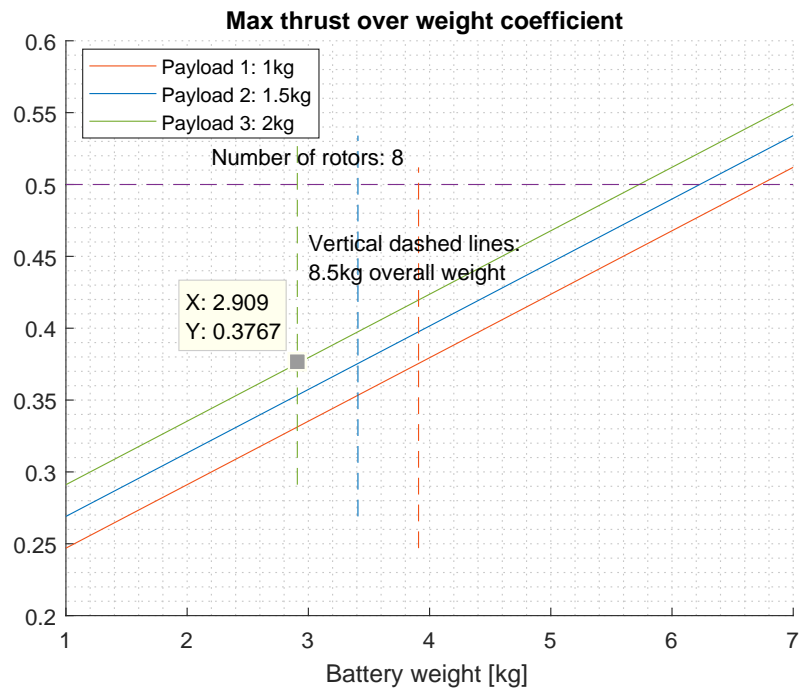
The results obtained with the above assumptions are:

- Hovering power: 1365 W
- Take-off weight: 8.5 kg
- Dry weight: 3.591 kg

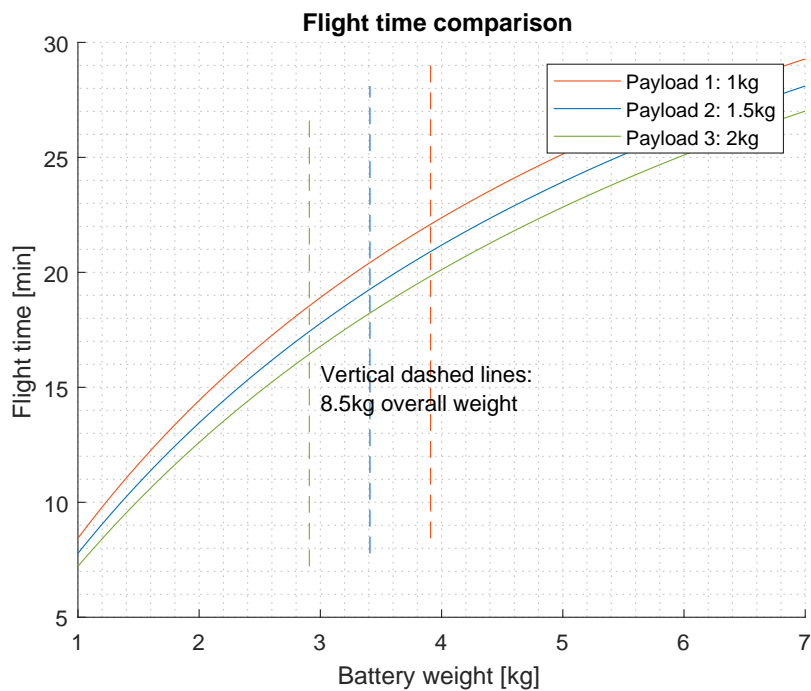
- Payload: 2 kg
- Flight hovering time: 16.4 min
- Battery weight: 2.909 kg

The higher take-off weight (8.5 kg with respect to 8 kg for the hexacopter) allows to integrate on the aircraft, the same payload considered in Section 2.2.2 and a slightly smaller battery.

From Figure 2.8a, the thrust coefficient is about 0.38 for a payload of 2 kg and battery mass of 2.909 kg. These quantities are close to those obtained with the eCalc software. Indeed, in Figure 2.9 can be noted that the percentage of thrust is almost equal to 0.40. The greatest difference is in flight time values (18.5 *min* estimated by Ecalc and 16.4 *min* computed). This is justified by the fact that in Section 2.1 the power load coefficient was assumed constant. In reality this is just an approximation, but perfectly in line with the purpose of the sizing. In fact, it has to be taken into account that the power load coefficient presents only small variations in the neighborhood of T_{hov} and that eCalc has an accuracy equal to 15%. In conclusion, the sized octocopter depicted in Figure 2.10, comprises a circular plate (of radius equal to 0.20 m) in order to carry devices and batteries.



(a)



(b)

Figure 2.8: Thrust coefficient (a) and flight time (b) with respect to battery weight and for three payloads (1 kg, 1.5 kg, 2 kg); (c): eCalc results

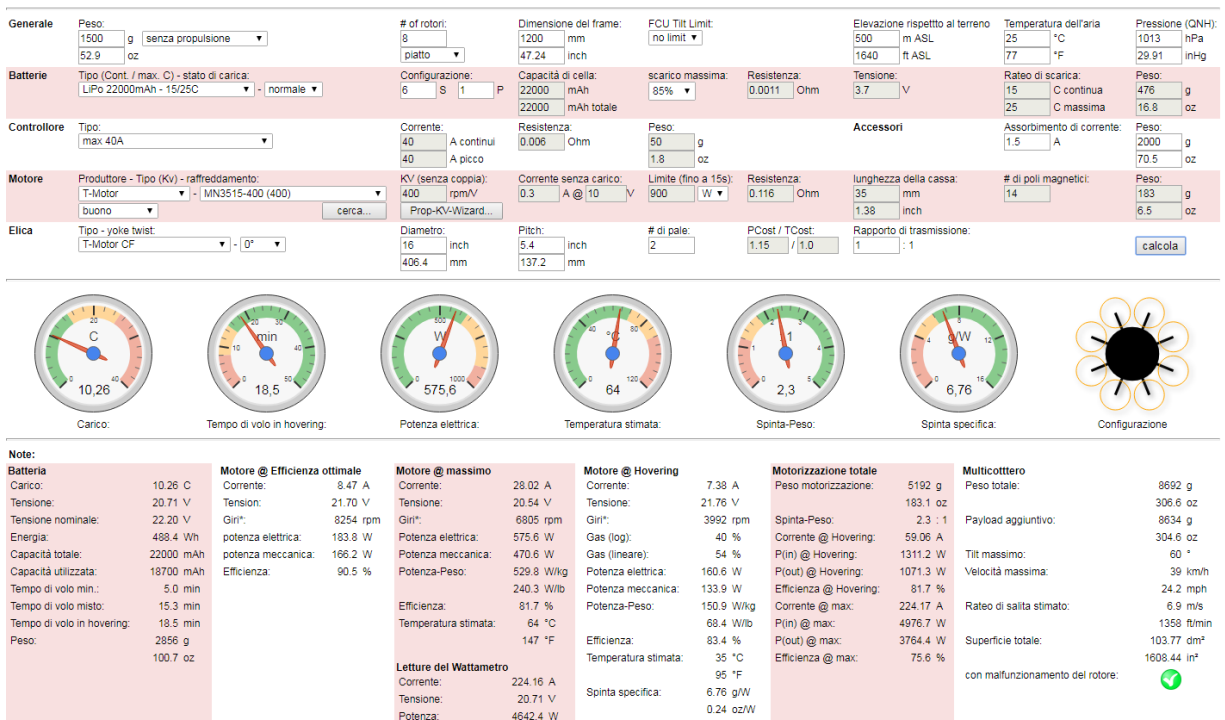


Figure 2.9: eCalc results

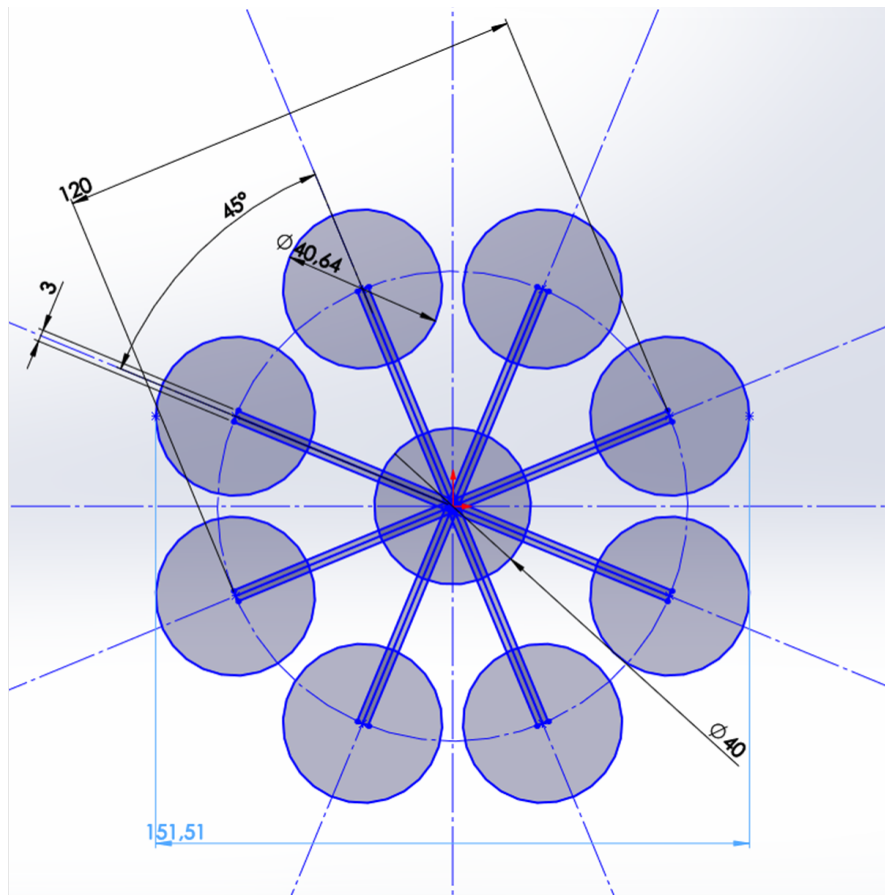


Figure 2.10: Final dimensions of the octocopter

Chapter 3

Dynamic modelling and simulation

This Chapter shall be structured as follows. Firstly, the actuators behaviour shall be characterized (with the support of *Momentum theory*). Secondly, the conventions and formalisms used to describe the dynamics of a multirotor UAV shall be presented and the equations of motion will be pointed out. Finally, the moments of inertia of the sized hexacopter and octorotor shall be computed and the final models will be implemented in Simulink.

3.0.1 Objectives

The main targets of this Chapter are:

- The computation of actuators coefficients (C_T , C_P , C_Q)
- Relating the rotor speed with the throttle
- The definition of the dynamic equations of motion of multicopters UAVs
- The computation of the moments of inertia

Once accomplished the first and second task, it will be possible to relate the external forces and moments (inputs) to the throttle developed by each actuator (outputs). Then the latter quantities will be the inputs of the multirotor dynamical system .

3.1 Actuator analysis

3.1.1 Momentum theory in hovering flight

A helicopter, or any other rotating-wing vehicle, can operate in a variety of flight regimes. These include the hover, climb, descent, or forward flight. Moreover, the

multicopter may undergo maneuvers, which may comprise a combination of these basic flight regimes. In hover or axial flight, the flow is axisymmetric and the flow through the rotor is either upward or downward. This is the easiest regime to analyze. The basic performance of the rotor can be analyzed by a simple approach that has become known as the Rankine-Froude *Momentum theory*. In this case, non-dimensional coefficients are normally employed in helicopter analysis as function of rotor thrust (T), disk area (A), blade radius (R), air density (ρ) and rotor speed (Ω). Therefore, in momentum theory, the rotor thrust coefficient is formally defined as:

$$C_T = \frac{T}{\rho A \Omega^2 R^2}. \quad (3.1)$$

The rotor power coefficient is defined as:

$$C_P = \frac{P}{\rho A \Omega^3 R^3}, \quad (3.2)$$

with P the rotor power. So, after some manipulation, the power coefficient for the hovering rotor is:

$$C_P = \frac{P}{\rho A \Omega^3 R^3} = \frac{C_T^{\frac{3}{2}}}{\sqrt{2}}. \quad (3.3)$$

Momentum theory underpredicts the actual power required because viscous effects are neglected. The rotor shaft torque coefficient is computed respect to torque (Q) as:

$$C_Q = \frac{Q}{\rho A \Omega^2 R^3}. \quad (3.4)$$

Since power is related to torque by $P = Q\Omega$, then $C_Q = C_P$. From the previous equations, it is possible to retrieve the relationship between propeller's thrust and rotational speed:

$$T = K_T \Omega^2, \quad (3.5)$$

where

$$K_T = C_T \rho A R^2. \quad (3.6)$$

In a similar way it is possible to write:

$$Q = K_Q \Omega^2; \quad (3.7)$$

with

$$K_Q = C_Q \rho A R^3. \quad (3.8)$$

Notice that K_T and K_Q are retrieved from data in Table 2.2 as demonstrated in Section 3.1.2.

3.1.2 Thrust and torque coefficient identification

A least squares approach has been used to estimate thrust and torque coefficients. "Least squares", means that the overall solution minimizes the sum of the squares of the errors made in the results of every single equation. Here an over-determined system of m linear equations in n unknowns, $(\beta_1, \beta_2, \beta_3, \dots, \beta_n)$ with $m > n$, is considered:

$$X\beta = y \quad (3.9)$$

$$X = \begin{bmatrix} X_{11} & X_{12} & \dots & X_{1n} \\ X_{21} & X_{22} & \dots & X_{2n} \\ \vdots & \vdots & \ddots & \vdots \\ X_{m1} & X_{m2} & \dots & X_{mn} \end{bmatrix}, \quad \beta = \begin{bmatrix} \beta_1 \\ \beta_2 \\ \vdots \\ \beta_m \end{bmatrix}, \quad y = \begin{bmatrix} y_1 \\ y_2 \\ \vdots \\ y_m \end{bmatrix}. \quad (3.10)$$

The goal is to find the coefficients $\hat{\beta}$ which fit the equations, in the sense of solving the quadratic minimization problem:

$$\hat{\beta} = \min_{\beta} J(\beta) = \min_{\beta} \|y - X\beta\|^2. \quad (3.11)$$

This minimization problem has a unique solution, provided that the n columns of matrix X are linearly independent. The solution is given by solving the normal equations:

$$\hat{\beta} = (X^T X)^{-1} X^T y. \quad (3.12)$$

Then, considering data in Table 2.2 and applying the above procedure, taking:

$$X = \begin{bmatrix} \Omega_{50}^2 \\ \Omega_{65}^2 \\ \Omega_{75}^2 \\ \Omega_{85}^2 \\ \Omega_{100}^2 \end{bmatrix}, \quad \beta = K_T, \quad y = \begin{bmatrix} T_{50} \\ T_{65} \\ T_{75} \\ T_{85} \\ T_{100} \end{bmatrix}, \quad (3.13)$$

the unique solution has been found:

$$\hat{\beta} = \hat{K}_T = (X^T X)^{-1} X^T y. \quad (3.14)$$

Therefore, to calculate C_T , C_P , C_Q and K_Q equations (3.6), (3.3), (3.8) and equality $C_Q = C_P$ are used. Furthermore, a static linear relationship between rotor speed Ω and throttle $Th\%$ has been found, given by:

$$\Omega = Th\%m + q. \quad (3.15)$$

The problem has been structured as:

$$X = \begin{bmatrix} Th_{50\%} & 1 \\ Th_{65\%} & 1 \\ Th_{75\%} & 1 \\ Th_{85\%} & 1 \end{bmatrix}, \quad \beta = \begin{bmatrix} m \\ q \end{bmatrix}, \quad y = \begin{bmatrix} \Omega_{50}^2 \\ \Omega_{65}^2 \\ \Omega_{75}^2 \\ \Omega_{85}^2 \end{bmatrix}; \quad (3.16)$$

$$\hat{\beta} = \begin{bmatrix} m \\ q \end{bmatrix} = (X^T X)^{-1} X^T y. \quad (3.17)$$

3.1.3 Results

The previous identification campaign has led to the following results:

$$\begin{cases} \widehat{K}_T = 6.6464 \cdot 10^{-5} & [kg \cdot m] \\ \widehat{C}_T = 0.0101 \\ \widehat{C}_P = 7.2093 \cdot 10^{-4} \\ \widehat{C}_Q = 7.2093 \cdot 10^{-4} \\ \widehat{m} = 5.4317 & [rad/s] \\ \widehat{q} = 154.0946 & [rad/s] \end{cases} \quad (3.18)$$

Notice that, the relationship between Ω and $Th\%$ shows a non linear behaviour, after values of $Th\%$ greater than 80%, (see Figure 3.1).

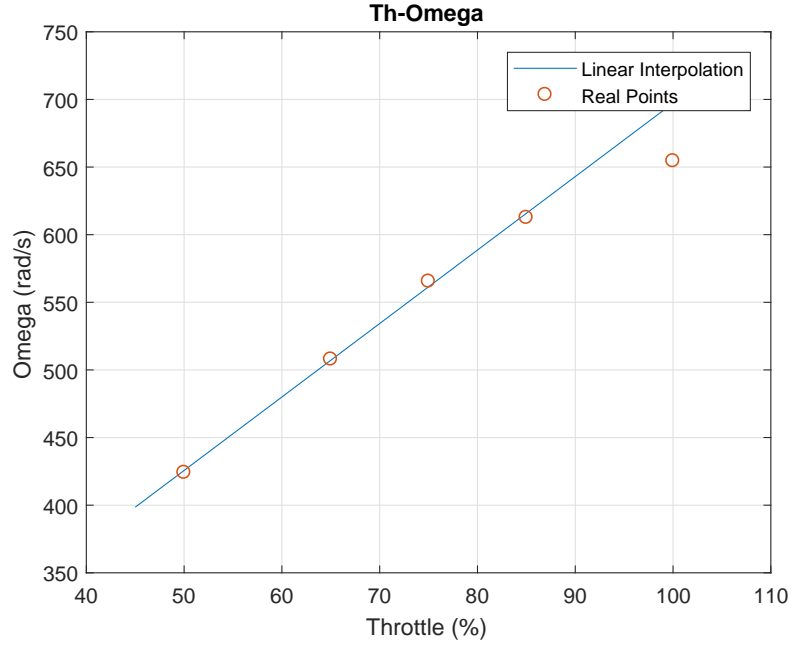


Figure 3.1: Omega VS Throttle

3.2 Dynamics of a multirotor UAV

3.2.1 Rotations formalism and equations of motion

According to mechanics, two reference systems are defined. The Earth reference system and the body reference system. The origin of the Earth axes is arbitrary. The three axes are aligned with the axis labeled North, the axis labeled East, and the surface normal that points toward the center of the Earth, Down. These three axes are mutually perpendicular and, when referred to in the order \mathbf{N} , \mathbf{E} , \mathbf{D} , form a right-handed coordinate system.

The body axes are a set of axes with origin at the center of gravity. The \mathbf{X} , \mathbf{Y} , and \mathbf{Z} axes form a right-handed system. The \mathbf{X} axis lies in the plane of symmetry and generally points forward. The \mathbf{Y} axis points towards right, normal to the plane of symmetry, and the \mathbf{Z} axis points down.

The transformation which maps the coordinates of a vector expressed in a coordinate frame (e.g., M) into the coordinates expressed in another frame (e.g., N) can be achieved using *rotation matrices*. Thus, adopting the to-from notation, vector P_M in system M can be resolved to system N as P_N , through a matrix operation:

$$P_N = R_{NM}P_M. \quad (3.19)$$

Rotation matrices in \mathbb{R}^3 permit to rotate a vector respect to one, two or three axes simultaneously. In a minimal representation the orientation is described by means of three independent parameters. In flight dynamics, one encounters a specific order of rotations using angles named Euler angles. The sequence is composed by:

- Rotation around axis Z (of angle Ψ)
- Rotation around the new Y' axis (of angle Θ)
- Rotation around newer X'' axis (of angle Φ)

Then, the matrix T_{BE} that resolves an Earth-based vector to body axes is defined as:

$$T_{BE}(\Phi, \Theta, \Psi) = R_X(\Phi)R_Y(\Theta)R_Z(\Psi) \quad (3.20)$$

$$T_{BE}(\Phi, \Theta, \Psi) = \begin{bmatrix} C_\Theta C_\Psi & C_\Theta S_\Psi & -S_\Theta \\ S_\Phi S_\Theta C_\Psi - C_\Phi S_\Psi & S_\Phi S_\Theta S_\Psi + C_\Phi C_\Psi & S_\Phi C_\Theta \\ C_\Phi S_\Theta C_\Psi + S_\Phi S_\Psi & C_\Phi S_\Theta S_\Psi - S_\Phi C_\Psi & C_\Phi C_\Theta \end{bmatrix}, \quad (3.21)$$

where $R_X(\Phi)$, $R_Y(\Theta)$, $R_Z(\Psi)$ are rotation matrices which perform rotations about the X, Y and Z axis respectively. In addition, a shorthand notation has been adopted, which is $C_\Theta = \cos(\Theta)$, $S_\Theta = \sin(\Theta)$. Therefore, Euler angles provide a way to represent the 3D orientation of an object using a combination of three rotations about different axes.

Euler angles, also, allow to rotate a velocity or acceleration vector from Earth axes to body axes:

$$P_e = \begin{bmatrix} N \\ E \\ D \end{bmatrix}, \quad V_e = \begin{bmatrix} \dot{N} \\ \dot{E} \\ \dot{D} \end{bmatrix} \implies V_b = T_{BE}(\Phi, \Theta, \Psi)V_e = \begin{bmatrix} u \\ v \\ w \end{bmatrix}; \quad (3.22)$$

where P_e is the position vector of the aircraft center of gravity in the inertial frame (North, East, and Down position), V_e is the velocity of the aircraft with respect to the Earth, and V_b is the linear velocity of the aircraft, resolved to body axes. The vector of angular position of the aircraft body axes with respect to the Earth, where the elements are roll angle, pitch angle and yaw angle is:

$$\alpha_e = \begin{bmatrix} \Phi \\ \Theta \\ \Psi \end{bmatrix}. \quad (3.23)$$

Furthermore, Euler angles rotate Euler rates into body-axis angular rates:

$$\omega_e = \begin{bmatrix} \dot{\Phi} \\ \dot{\Theta} \\ \dot{\Psi} \end{bmatrix}, \quad \omega_b = \begin{bmatrix} p \\ q \\ r \end{bmatrix} \implies \omega_b = E(\Phi, \Theta)\omega_e = \begin{bmatrix} 1 & 0 & -S_\Theta \\ 0 & C_\Phi & S_\Phi C_\Theta \\ 0 & -S_\Phi & C_\Phi C_\Theta \end{bmatrix} \omega_e, \quad (3.24)$$

with ω_b and ω_e , body-axis and Earth-axis rates, respectively. The opposite transformation can be achieved, inverting matrix E .

If the mass of the aircraft m is constant, then, the equation of linear and angular motion can be written as (see Giurato [2]):

$$\begin{cases} m\dot{V}_b + \omega_b \times (mV_b) = F_{ext} \\ I_n \dot{\omega}_b + \omega_b \times (I_n \omega_b) = M_{ext}, \end{cases} \quad (3.25)$$

with:

$$I_n = \begin{bmatrix} I_{xx} & -I_{xy} & -I_{xz} \\ I_{xy} & I_{yy} & -I_{yz} \\ -I_{xz} & -I_{yz} & I_{zz} \end{bmatrix}, \quad F_{ext} = \begin{bmatrix} F_X \\ F_Y \\ F_Z \end{bmatrix}, \quad M_{ext} = \begin{bmatrix} L \\ M \\ N \end{bmatrix}, \quad (3.26)$$

where I_n is the inertia tensor, F_{ext} is the vector of external forces (which comprises aerodynamics, gravity, and others) and M_{ext} is the vector of moments applied on the body-axis X (L), Y (M) and Z (N).

Notice that, if the body frame is coincident with the symmetry axes of the aircraft body, one can assume the inertia tensor as a diagonal matrix.

The usual expressions of the equations of motion use the concept of state vector. In this work the state vector has been ordered as follows:

$$x = \begin{bmatrix} P_e \\ V_b \\ \omega_b \\ \alpha_e \end{bmatrix} = [N \ E \ D \ u \ v \ w \ p \ q \ r \ \Phi \ \Theta \ \Psi]^T. \quad (3.27)$$

Thus, the state vector derivative:

$$\dot{x} = \begin{bmatrix} \dot{P}_e \\ \dot{V}_b \\ \dot{\omega}_b \\ \dot{\alpha}_e \end{bmatrix} = \begin{bmatrix} T_{BE}^T V_b \\ -\omega_b \times (V_b) + F_{ext}/m \\ I_n^{-1}(-\omega_b \times (I_n \omega_b) + M_{ext}) \\ E^{-1} \omega_b \end{bmatrix}. \quad (3.28)$$

3.2.2 External forces and moments

In order to define the forces and moments, the multicopter geometry has to be considered. Starting from the hexarotor, two configurations have been taken into account depending on the direction of rotation of the propellers.

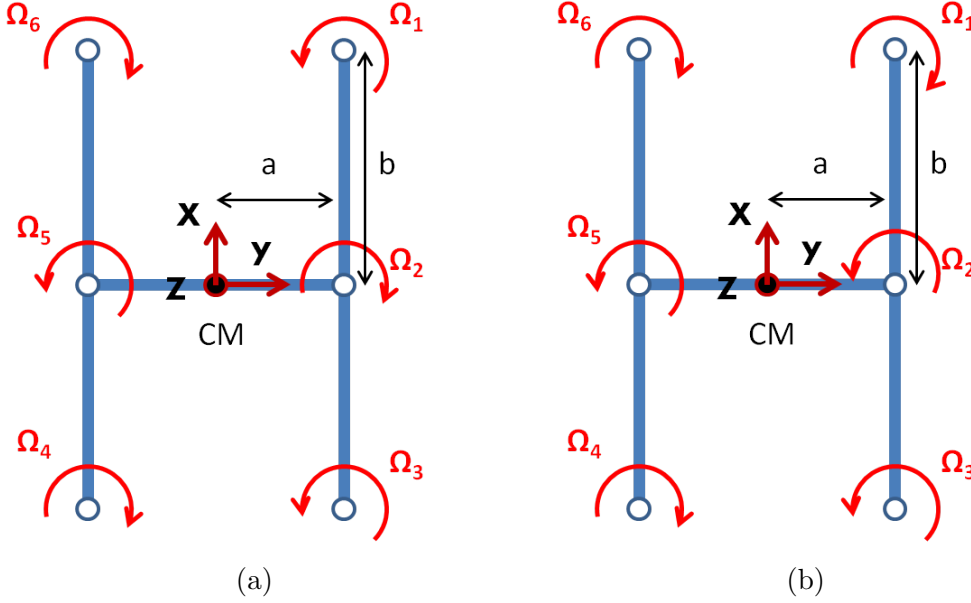


Figure 3.2: (a) PNPNPN configuration; (b) NPPNP configuration

Naming with **P** the propellers whose rotation causes a positive yaw motion and with **N** those which cause a negative yaw motion, in Figures 3.2a and 3.2b the chosen configurations, the label of each propeller, and its rotation direction are pictured.

Concerning forces and moments, each propeller produces a thrust and a torque proportional to the square of the rotational speed (equations (3.5) and (3.7)). Then forces and moments produced by the six propellers for the PNPNPN configuration, are:

$$F_{prop} = - \begin{bmatrix} 0 \\ 0 \\ K_T(\Omega_1^2 + \Omega_2^2 + \Omega_3^2 + \Omega_4^2 + \Omega_5^2 + \Omega_6^2) \end{bmatrix}, \quad (3.29)$$

$$M_{prop} = \begin{bmatrix} L \\ M \\ N \end{bmatrix} = \begin{bmatrix} K_T a (-\Omega_1^2 - \Omega_2^2 - \Omega_3^2 + \Omega_4^2 + \Omega_5^2 + \Omega_6^2) \\ K_T b (\Omega_1^2 - \Omega_3^2 - \Omega_4^2 + \Omega_6^2) \\ K_Q (\Omega_1^2 - \Omega_2^2 + \Omega_3^2 - \Omega_4^2 + \Omega_5^2 - \Omega_6^2) \end{bmatrix} \quad (3.30)$$

and for the NPPNP configuration:

$$F_{prop} = - \begin{bmatrix} 0 \\ 0 \\ K_T(\Omega_1^2 + \Omega_2^2 + \Omega_3^2 + \Omega_4^2 + \Omega_5^2 + \Omega_6^2) \end{bmatrix}, \quad (3.31)$$

$$M_{prop} = \begin{bmatrix} L \\ M \\ N \end{bmatrix} = \begin{bmatrix} K_T a (-\Omega_1^2 - \Omega_2^2 - \Omega_3^2 + \Omega_4^2 + \Omega_5^2 + \Omega_6^2) \\ K_T b (\Omega_1^2 - \Omega_3^2 - \Omega_4^2 + \Omega_6^2) \\ K_Q (-\Omega_1^2 + \Omega_2^2 + \Omega_3^2 - \Omega_4^2 + \Omega_5^2 - \Omega_6^2) \end{bmatrix}. \quad (3.32)$$

Forces and moments can be rearranged to realize the so called *mixer matrix* χ of the motors, which relates forces and moments with rotational speeds. Therefore, marking as χ_{H_1} and χ_{H_2} the mixer matrices for the PNPNP and the NPPNP configuration, respectively, we have:

$$\chi_{H_1} = \begin{bmatrix} -K_T & -K_T & -K_T & -K_T & -K_T & -K_T \\ -K_T a & -K_T a & -K_T a & K_T a & K_T a & K_T a \\ K_T b & 0 & -K_T b & -K_T b & 0 & K_T b \\ K_Q & -K_Q & K_Q & -K_Q & K_Q & -K_Q \end{bmatrix}, \quad (3.33)$$

$$\chi_{H_2} = \begin{bmatrix} -K_T & -K_T & -K_T & -K_T & -K_T & -K_T \\ -K_T a & -K_T a & -K_T a & K_T a & K_T a & K_T a \\ K_T b & 0 & -K_T b & -K_T b & 0 & K_T b \\ -K_Q & K_Q & K_Q & -K_Q & K_Q & -K_Q \end{bmatrix}. \quad (3.34)$$

Another force which actually acts on the center of gravity is the gravitational force, rotated into the body frame:

$$F_g = T_{BE} \begin{bmatrix} 0 \\ 0 \\ mg \end{bmatrix} = \begin{bmatrix} -S_\Theta \\ S_\Phi C_\Theta \\ C_\Phi C_\Theta \end{bmatrix} mg. \quad (3.35)$$

Then, the complete equations of motion can be written as:

$$\begin{cases} m\dot{V}_b + \omega_b \times (mV_b) = F_{ext} = F_g + F_{Prop} \\ I_n \dot{\omega}_b + \omega_b \times (I_n \omega_b) = M_{ext} = M_{prop}. \end{cases} \quad (3.36)$$

Due to the fact that the equations of motion remain the same from an N -rotors to an M -rotors multicopter (N and M number of rotors), while the propellers forces and moments do change, only these need to be recomputed for the octorotor structure.

In particular, similarly to what has been previously done, and paying attention to configurations in Figure 3.3, the mixer matrices have been computed:

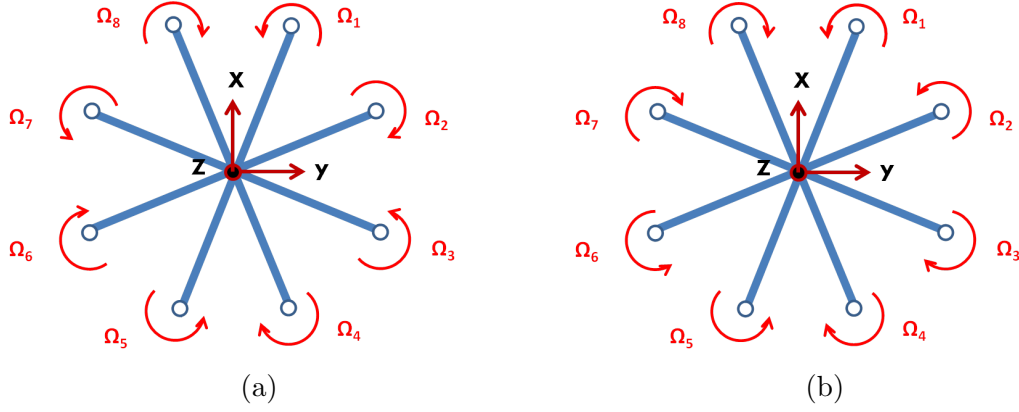


Figure 3.3: (a) PNPNPNP configuration; (b) PPNNPPNN configuration

$$\chi_{O_1} = \begin{bmatrix} -K_T & -K_T & -K_T & -K_T & -K_T & -K_T & -K_T & -K_T \\ -K_T a_{\frac{3\pi}{8}} & -K_T a_{\frac{\pi}{8}} & -K_T a_{\frac{\pi}{8}} & -K_T a_{\frac{3\pi}{8}} & K_T a_{\frac{3\pi}{8}} & K_T a_{\frac{\pi}{8}} & K_T a_{\frac{\pi}{8}} & K_T a_{\frac{3\pi}{8}} \\ K_T b_{\frac{3\pi}{8}} & K_T b_{\frac{\pi}{8}} & -K_T b_{\frac{\pi}{8}} & -K_T b_{\frac{3\pi}{8}} & -K_T b_{\frac{3\pi}{8}} & -K_T b_{\frac{\pi}{8}} & K_T b_{\frac{\pi}{8}} & K_T b_{\frac{3\pi}{8}} \\ K_Q & -K_Q & K_Q & -K_Q & K_Q & -K_Q & K_Q & K_Q \end{bmatrix} \quad (3.37)$$

$$\chi_{O_2} = \begin{bmatrix} -K_T & -K_T & -K_T & -K_T & -K_T & -K_T & -K_T & -K_T \\ -K_T a_{\frac{3\pi}{8}} & -K_T a_{\frac{\pi}{8}} & -K_T a_{\frac{\pi}{8}} & -K_T a_{\frac{3\pi}{8}} & K_T a_{\frac{3\pi}{8}} & K_T a_{\frac{\pi}{8}} & K_T a_{\frac{\pi}{8}} & K_T a_{\frac{3\pi}{8}} \\ K_T b_{\frac{3\pi}{8}} & K_T b_{\frac{\pi}{8}} & -K_T b_{\frac{\pi}{8}} & -K_T b_{\frac{3\pi}{8}} & -K_T b_{\frac{3\pi}{8}} & -K_T b_{\frac{\pi}{8}} & K_T b_{\frac{\pi}{8}} & K_T b_{\frac{3\pi}{8}} \\ K_Q & K_Q & -K_Q & -K_Q & K_Q & K_Q & -K_Q & -K_Q \end{bmatrix}, \quad (3.38)$$

where:

$$\begin{aligned} a_{\frac{3\pi}{8}} &= \frac{l}{2} \cos\left(\frac{3\pi}{8}\right) \\ a_{\frac{\pi}{8}} &= \frac{l}{2} \cos\left(\frac{\pi}{8}\right) \\ b_{\frac{3\pi}{8}} &= \frac{l}{2} \sin\left(\frac{3\pi}{8}\right) \\ b_{\frac{\pi}{8}} &= \frac{l}{2} \sin\left(\frac{\pi}{8}\right), \end{aligned} \quad (3.39)$$

with χ_{O_1} and χ_{O_2} the mixer matrices for the PNPNPNP and the PPNNPPNN configuration respectively; $l/2$ the arm length and $\pi/4$ the angular distance between two consecutive arms.

3.3 Inertia matrix

In order to compute the inertia matrices the following assumptions and simplifications have been made:

- each frame beam has a square cross section (side equal to $w = 0.03$ m)
- frame beams have the same weight ($m_{beam} = 0.200$ kg)
- the plate weight is given by the equation (3.40)
- the height of the plate is $z = h = 0.15$ m

$$m_{plate} = MTOW - m_{mot}N_r - m_{fr}. \quad (3.40)$$

Notice that, the computation of the plate mass is based on the $MTOW$, since the multicopter is sized accounting for the maximum value of payload. Furthermore, the following approximation is made in order to simplify the computations, the mass of the devices placed on the plate is uniformly distributed inside the plate. In both, the hexacopter and the octocopter platforms, the inertia tensors of the beams, motors and plate are computed separately and then summed together along the relative axes.

3.3.1 Hexacopter

The Hexacopter (with $a = 0.35$ m and $b = 0.46$ m) is constituted by two longitudinal beams and a lateral one. Motors are considered as point masses of 0.260 kg. So, the inertia moments relative to the frame are given by:

$$\begin{aligned} I_{xx_f} &= 2\left(\frac{1}{12}m_{beam}(2w^2) + m_{beam}2w^2\right) + \frac{1}{12}m_{beam}((2a)^2 + w^2) \\ I_{yy_f} &= 2\left(\frac{1}{12}m_{beam}((2b)^2 + w^2) + m_{beam}a^2\right) + \frac{1}{12}m_{beam}((2a)^2 + w^2) \\ I_{zz_f} &= 2\left(\frac{1}{12}m_{beam}((2b)^2 + w^2) + m_{beam}a^2\right) + \frac{1}{12}m_{beam}((2a)^2 + w^2). \end{aligned} \quad (3.41)$$

While for the motors:

$$\begin{aligned} I_{xx_m} &= 6m_{mot}a^2 \\ I_{yy_m} &= 4m_{mot}b^2 \\ I_{zz_m} &= 6m_{mot}a^2 + 4m_{motor}b^2. \end{aligned} \quad (3.42)$$

Taking the dimensions of the plate in Figure 2.6 ($x = 0.40$ m, $y = 0.20$ m) and the plate mass $m_{plate} = 5.84$ kg, the plate moments of inertia are:

$$\begin{aligned} I_{xx_p} &= \frac{1}{12}m_{plate}(y^2 + z^2) \\ I_{yy_p} &= \frac{1}{12}m_{plate}(x^2 + z^2) \\ I_{zz_p} &= \frac{1}{12}m_{plate}(x^2 + y^2). \end{aligned} \quad (3.43)$$

Then, the total moments of inertia are:

$$\begin{aligned} I_{xx} &= I_{xx_f} + I_{xx_m} + I_{xx_p} \\ I_{yy} &= I_{yy_f} + I_{yy_m} + I_{yy_p} \\ I_{zz} &= I_{zz_f} + I_{zz_m} + I_{zz_p}. \end{aligned} \quad (3.44)$$

In conclusion, due to symmetry:

$$I_{n_H} = \begin{bmatrix} I_{xx} & 0 & 0 \\ 0 & I_{yy} & 0 \\ 0 & 0 & I_{zz} \end{bmatrix}. \quad (3.45)$$

3.3.2 Octocopter

The octo-frame has an X-shape. On one hand the X-structure, permits to obtain an higher order symmetry respect to hexacopter; on the other hand the inertia moments of the frame needs to be translated along the principal axes (X, Y and Z) of the body-frame. To achieve this target, *rotation matrices* have been used. Especially, knowing one principal axis (Z) which coincides with Z' it is necessary to accomplish a plane rotation along the other axes. The situation is depicted in Figure 3.4:

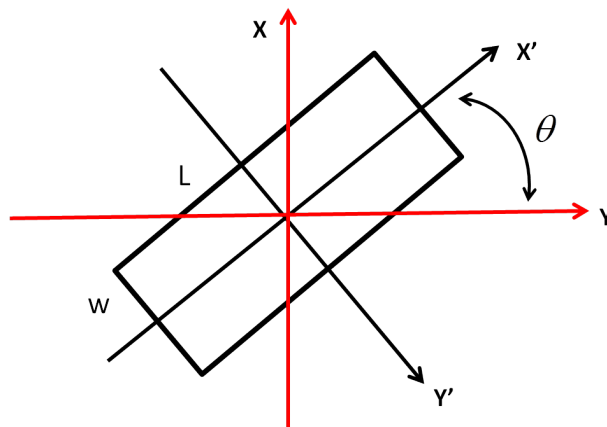


Figure 3.4: Plane rotation

The coordinate transformation that takes a vector in X', Y', Z' reference into the X, Y, Z is:

$$\begin{cases} X = X' \sin(\theta) - Y' \cos(\theta) \\ Y = X' \cos(\theta) + Y' \sin(\theta) \\ Z = Z' \end{cases} \implies T = \begin{bmatrix} S_\theta & -C_\theta & 0 \\ C_\theta & S_\theta & 0 \\ 0 & 0 & 1 \end{bmatrix}. \quad (3.46)$$

Applying a superscript notation to indicate the reference frames, the inertia tensor rotation is given by:

$$I^{XYZ} = [T][I^{X'Y'Z'}][T^T]. \quad (3.47)$$

Since, for the octocopter frame (made up of four arms at distance $\frac{\pi}{4}$ each other), $\theta = \frac{\pi}{8}, \frac{3\pi}{8}, \frac{5\pi}{8}, \frac{7\pi}{8}$; the result is of four rotation matrices. Therefore, for each beam of length $l = 1.20$ m (see Figure 2.10 for dimensions), and square cross section the moments of inertia have been computed through the following formulas:

$$\begin{cases} I_{xx_f}^{X'Y'Z'} = \frac{1}{12}m_{beam}(2w^2) \\ I_{yy_f}^{X'Y'Z'} = \frac{1}{12}m_{beam}(l^2 + w^2) \\ I_{zz_f}^{X'Y'Z'} = \frac{1}{12}m_{beam}(l^2 + w^2) \end{cases} \implies I_f^{X'Y'Z'} = \begin{bmatrix} I_{xx}^{X'Y'Z'} & 0 & 0 \\ 0 & I_{yy}^{X'Y'Z'} & 0 \\ 0 & 0 & I_{zz}^{X'Y'Z'} \end{bmatrix}. \quad (3.48)$$

So, the total frame inertia matrix along the principal axes is given by:

$$I_{n_f} = [T_{\frac{\pi}{8}}][I_f^{X'Y'Z'}][T_{\frac{\pi}{8}}^T] + [T_{\frac{3\pi}{8}}][I_f^{X'Y'Z'}][T_{\frac{3\pi}{8}}^T] + [T_{\frac{5\pi}{8}}][I_f^{X'Y'Z'}][T_{\frac{5\pi}{8}}^T] + [T_{\frac{7\pi}{8}}][I_f^{X'Y'Z'}][T_{\frac{7\pi}{8}}^T]. \quad (3.49)$$

Notice that, the subscript in matrix T underlines the respective θ value.

As previously done, inertia moments related to motors are given by:

$$\begin{aligned} I_{xx_m} &= 4m_{mot} \left[\left(\frac{l}{2} \cos\left(\frac{\pi}{8}\right) \right)^2 + \left(\frac{l}{2} \cos\left(\frac{3\pi}{8}\right) \right)^2 \right] \\ I_{yy_m} &= 4m_{mot} \left[\left(\frac{l}{2} \sin\left(\frac{\pi}{8}\right) \right)^2 + \left(\frac{l}{2} \sin\left(\frac{3\pi}{8}\right) \right)^2 \right] \\ I_{zz_m} &= 8m_{mot} \left(\frac{l}{2} \right)^2. \end{aligned} \quad (3.50)$$

While the inertia moments related to the plate have been computed as:

$$\begin{aligned} I_{xx_p} &= \frac{1}{12}m_{plate}(3r^2 + h^2) \\ I_{yy_p} &= I_{xx_p} \\ I_{zz_p} &= \frac{1}{2}m_{plate}(r^2). \end{aligned} \quad (3.51)$$

Note that, since $\cos(\frac{\pi}{8}) = \sin(\frac{3\pi}{8})$ and $\cos(\frac{3\pi}{8}) = \sin(\frac{\pi}{8})$, as a consequence $I_{xx_m} = I_{yy_m}$.

The sum of all the moments of inertia in matrix form is shown below:

$$I_{nO} = I_{nf} + I_{nm} + I_{np}. \quad (3.52)$$

3.3.3 Results

Table 3.1 shows the inertia values:

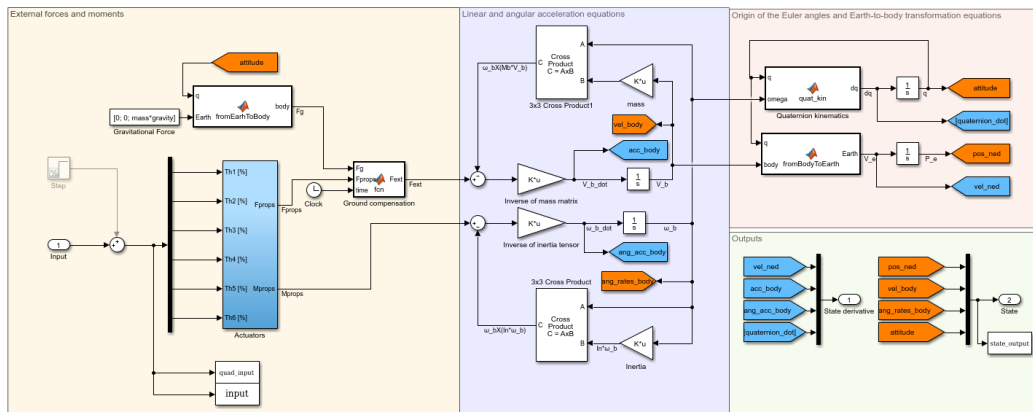
	I_{xx}	I_{yy}	I_{zz}	Unit
Hexa	0.278	0.373	0.594	$[kg \cdot m^2]$
Octo	0.489	0.489	0.957	$[kg \cdot m^2]$

Table 3.1: Summary table of moments of inertia

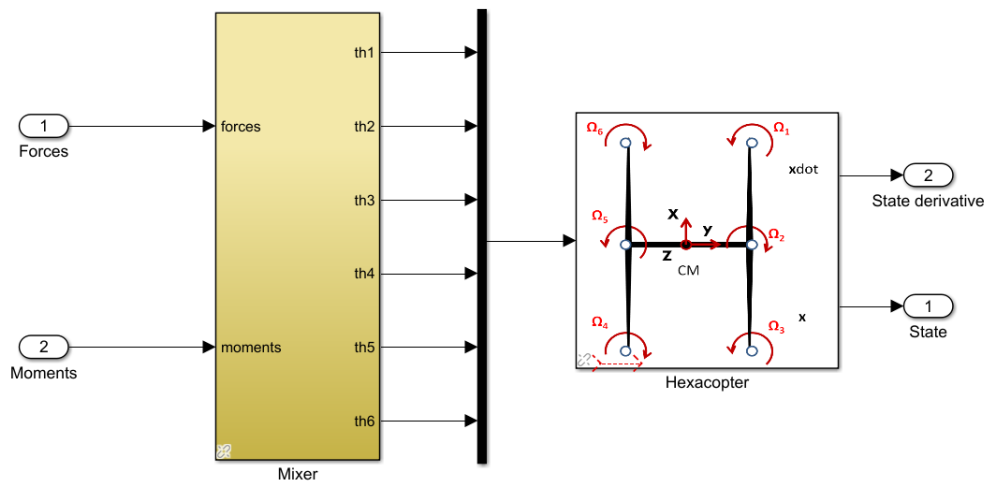
It can be noted that, while in the hexacopter $I_{xx} \neq I_{yy}$, in the octocopter the I_{xx} and I_{yy} are equal due to the symmetry of the chassis.

3.4 Simulink

The overall model given by equations (3.36) and (3.28), has been implemented in Simulink for both the hexarotor (Figure 3.5) and the octorotor (Figure 3.6).

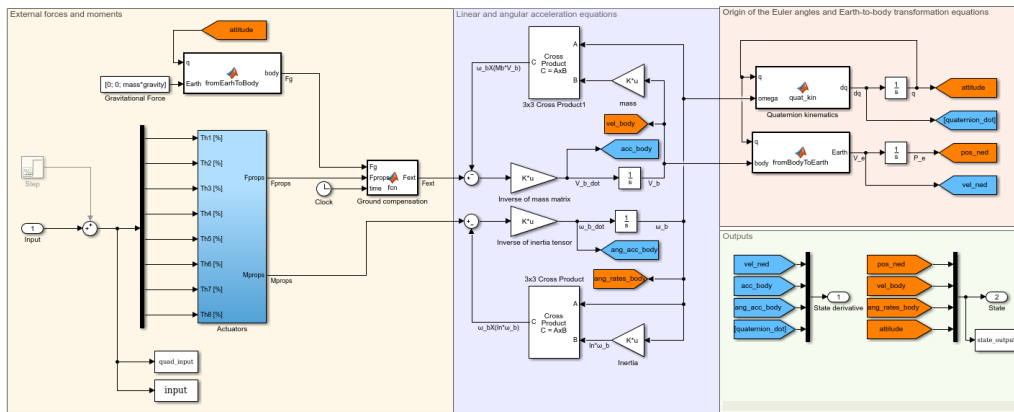


(a)

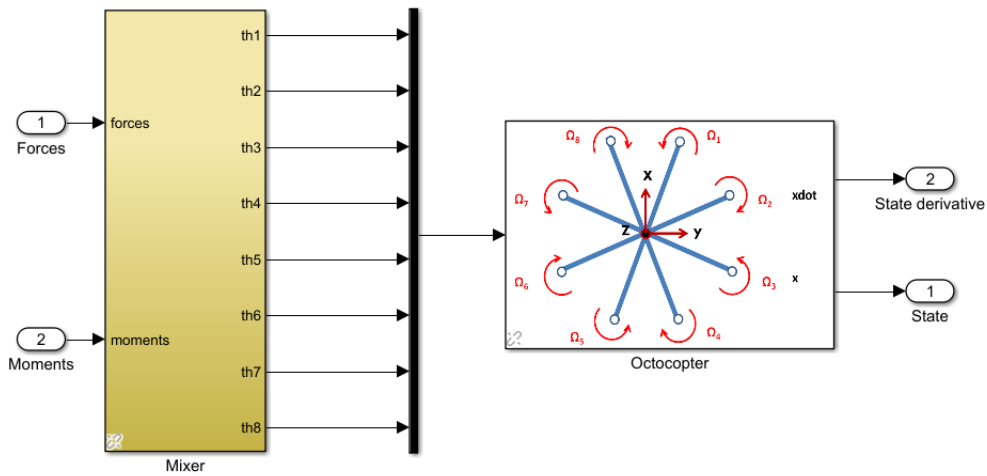


(b)

Figure 3.5: (a) Simulator of the hexacopter; (b) Simulator of the hexacopter and mixer



(a)



(b)

Figure 3.6: (a) Simulator of the octocopter; (b) Simulator of the octocopter and mixer

Chapter 4

Control law design

In this chapter the model which describes the behaviour of a multicopter in hovering condition shall be pointed out. Then, the basics regarding a structured H_∞ synthesis will be described. Moreover, the structure of the control system will be defined and an H_∞ control synthesis will be applied to compute the parameters of the regulators. In conclusion, the controllers shall be implemented on the simulator of the hexacopter and the octocopter and the results will be given.

4.1 Hovering model

The matrix equation (3.28) shows that the dynamics of motion of the system are fully non linear. Therefore, a more simplified model of the system in near hovering has been computed in order to be able to design a linear controller. The system model (3.28) is linearised around the equilibrium point \bar{x} with:

$$\begin{cases} \bar{x} = [\bar{N} \quad \bar{E} \quad \bar{D} \quad 0_{1 \times 9}]^T \\ \delta x = x - \bar{x} \\ \delta u = [\delta F_z \quad \delta L \quad \delta M \quad \delta N]^T \end{cases} \quad (4.1)$$

The final linear model is given by the following equations:

$$\begin{cases} \dot{N} = u \\ \dot{E} = v \\ \dot{D} = w \end{cases} \quad (4.2)$$

$$\begin{cases} \dot{u} = -g\Theta \\ \dot{v} = g\Phi \\ \dot{w} = \frac{\delta F_z}{m} \end{cases} \quad (4.3)$$

$$\begin{cases} \dot{p} = \frac{\delta L}{I_{xx}} \\ \dot{q} = \frac{\delta M}{I_{yy}} \\ \dot{r} = \frac{\delta N}{I_{zz}} \end{cases} \quad (4.4)$$

$$\begin{cases} \dot{\Phi} = p \\ \dot{\Theta} = q \\ \dot{\Psi} = r \end{cases} \quad (4.5)$$

4.2 Control strategy

The adopted control logic is based on PID regulators, which are the subjects of an H_∞ control synthesis.

4.2.1 Structured H_∞ synthesis

H_∞ is a control law synthesis technique which has become increasingly popular in the control engineering community over the years, finding application in several fields.

The H_∞ control law synthesis problem can be summarized as follows: let $G(s)$ be the (multivariable) transfer function of the plant, with control inputs $u \in \mathbb{R}^m$ and measurable outputs $y \in \mathbb{R}^p$ which are used to close the loop with the regulator $K(s)$. Additionally, performance inputs w and outputs z , can be defined. Such performance signals can be weighted and frequency-dependent weighting functions are employed. In this way, an augmented plant $P(s)$ is obtained by introducing the additional performance signals and weight functions to the original plant $G(s)$. Moreover, the structured controller $K(s; \theta)$ (Figure 4.1) combines all tunable control elements in a vector θ .

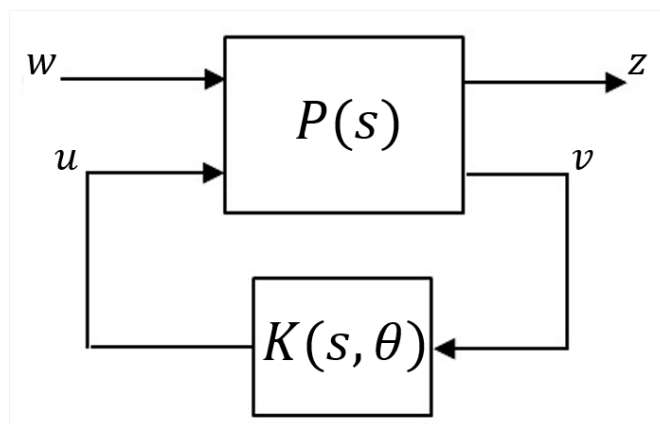


Figure 4.1: H_∞ synthesis scheme

The approach, here used to solve the structured H_∞ control synthesis is a mixed-sensitivity one. In this particular case the transfer functions to be shaped are:

- sensitivity function $S(s)$
- control sensitivity function $Q(s)$
- complementary sensitivity function $T(s)$.

Thus, the cost function of the optimization problem is given by:

$$J(\theta) = \max_{i=1,\dots,3} J_i(\theta). \quad (4.6)$$

Where $J_i(\theta)$ is one of the $n = 3$ cost functions to be minimized given by:

$$J_1(\theta) = \|W_s(s)S(s, \theta)\|_\infty, \quad J_2(\theta) = \|W_q(s)Q(s, \theta)\|_\infty, \quad J_3(\theta) = \|W_t(s)T(s, \theta)\|_\infty. \quad (4.7)$$

To solve this optimization problem, the Robust Control Toolbox of MATLAB has been used. For the assigned controller structure, the procedure finds the (locally) optimal parameters for the regulators so as to satisfy the requirements given in terms of weighting function (see [3] and [4]).

4.2.2 Method and PID structure

The regulation system is based on PIDs. Note that, since FCUs work at about 100 Hz, discrete time PIDs are considered. Equation (4.8) describes the behaviour of the PID controller:

$$u = K_p e + K_i \frac{t_s}{z-1} e - K_d \frac{z-1}{z t_s} Z(z) y, \quad (4.8)$$

with t_s the sample time, u the input to the system to be controlled, e the reference error value and y the measured output, respectively. $Z(z)$ is obtained discretizing a continuous low pass filter with time constant equal to 0.01 s. The parameters to be tuned are the proportional action (K_p), the integral action (K_i) and the derivative one (K_d).

The state variables N and E depend respectively on pitch (Θ) and roll (Φ) by the equations:

$$\begin{cases} \ddot{N} = \dot{u} = -g\Theta \\ \ddot{E} = \dot{v} = g\Phi \end{cases} \quad (4.9)$$

therefore, the translational controllers have been tuned once stabilized the attitude behaviour. The scheme adopted to control the roll, pitch and yaw angles is

	Roll	Pitch	Yaw
r	Φ_0	Θ_0	Ψ_0
u_2	p_0	q_0	r_0
u_1	δL	δM	δN
y_1	p	q	r
y_2	Φ	Θ	Ψ
$G_i(s)$	$\frac{1}{sI_{xx}}$	$\frac{1}{sI_{yy}}$	$\frac{1}{sI_{zz}}$
$G_o(s)$	$\frac{1}{s}$	$\frac{1}{s}$	$\frac{1}{s}$

Table 4.1: Signals and transfer functions

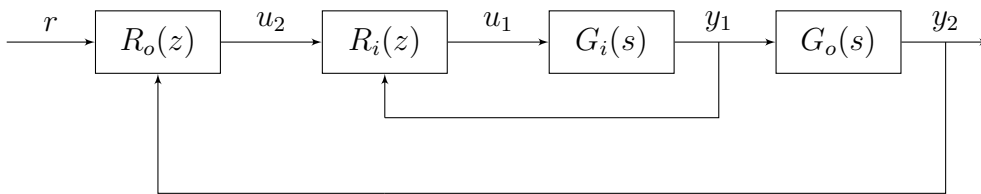


Figure 4.2: Adopted scheme for controlling the attitude

depicted in Figure 4.2. While Table 4.1 shows the signals and transfer functions related to the particular DoF under exam.

The block diagram in Figure 4.3 has been applied to control the motion in North and East directions. Notice that it is composed by a cascade of four loops (including the attitude), where C_o and C_i are the position and velocity controllers, respectively.

Similar block diagram can be used for the motion along the Down axis, (see Figure 4.4).

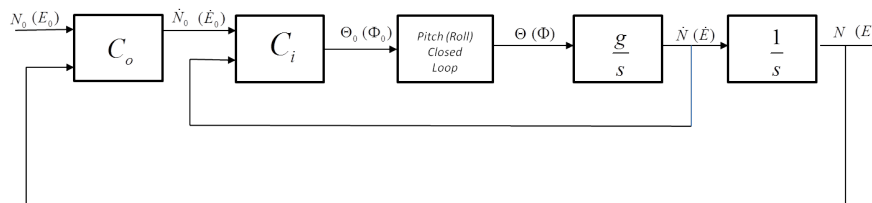


Figure 4.3: Position closed loop block diagram

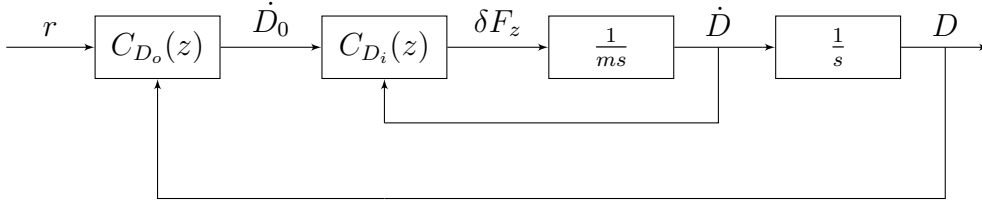


Figure 4.4: Adopted scheme for controlling the altitude

4.2.3 Hexacopter tuning requirements

Roll and pitch control

In general, weights are functions of frequency, they are chosen to be stable, minimum phase, proper transfer functions. The inverse of the magnitude of a weight can be interpreted as the desired shape, or template, for the magnitude of the transfer function to be shaped. The mapping from requirements to frequency-domain metrics can be summarised as follows:

- Sensitivity: The sensitivity function is related to the multirotor performance. The structure of the weighting function on the sensitivity is:

$$W_s(s) = \frac{s/M_s + p}{s + Ap}, \quad (4.10)$$

where $A = 10^{-3}$ is the desired attenuation in the interested frequency range and it is related to the tracking error; $M_s = 1.5$ is the maximum magnitude peak, while p is chosen in order to obtain $|W_s(j\omega_b)^{-1}| = -3dB$ at the desired bandwidth $\omega_b = 1.5$ rad/s.

- Control sensitivity: The weighting function $W_q(s)$ on the control sensitivity $Q(s)$ has been chosen to keep the control action moderated at high frequencies:

$$W_q(s) = K \frac{s + \omega_a 10^{-3}}{s + \omega_a}, \quad (4.11)$$

where $\omega_a = 17$ rad/s is the hypothesized value of the actuator bandwidth. This value has been defined based on the results in [2] and [5]; while $K = \pi/6$ is the high frequencies gain.

- Complementary sensitivity: The weighting function $W_t(s)$ is specified as requirement of attenuation of the disturbance on the control error:

$$W_t(s) = \frac{s + p/M_t}{As + p}, \quad (4.12)$$

where $A = 10^{-3}$, $M_t = 1.5$ and p is chosen to obtain $|W_t(j\omega_{bt})^{-1}| = -3dB$ with $\omega_{bt} = 2.25 \text{ rad/s} > \omega_b$. Therefore, the desired cut-off frequency of the open loop should be $\omega_b < \omega_c < \omega_{bt}$.

Notice that the same requirements have been applied to both roll and pitch angles as to guarantee same performances.

The results are given in Figures 4.5 and 4.6.

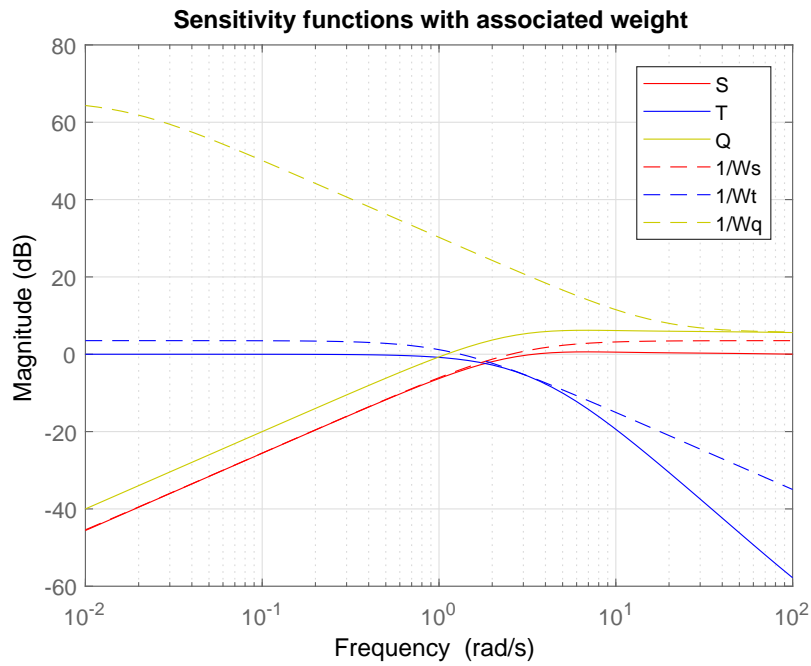


Figure 4.5: Sensitivity functions with associated weights on the roll angle

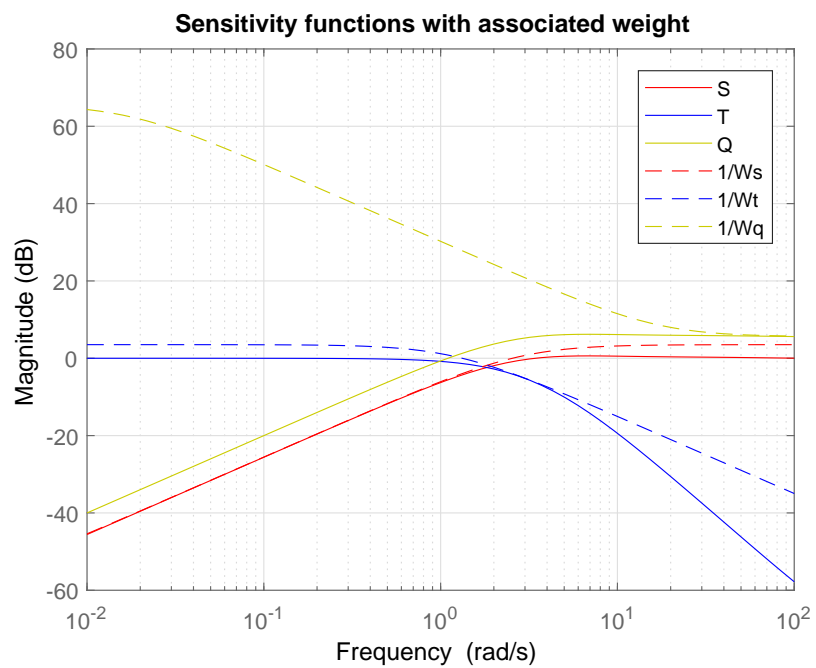


Figure 4.6: Sensitivity functions with associated weights on the pitch angle.

Position and heading control

In the translational control the weight functions taken into account, have the same structure of the ones just seen for the attitude.

In particular for the North and East motion the requirements are given in terms of $\omega_b = 0.5 \text{ rad/s}$, $\omega_{bt} = 0.75 \text{ rad/s}$, $A = 10^{-3}$ and $M_s = 2$, $M_t = 1.1$. The altitude behaviour is faster because does not depend on the attitude, therefore the requirements have been defined as: $\omega_b = 1 \text{ rad/s}$, $\omega_{bt} = 1.5 \text{ rad/s}$, $A = 10^{-3}$ and $M_s = M_t = 1.2$. In the end, the heading positioning behaviour has a slower dynamic respect to roll and pitch. Therefore, the requirements are: $w_b = 0.8 \text{ rad/s}$, $w_{bt} = 1.2 \text{ rad/s}$, $A = 10^{-3}$ and $M_s = M_t = 1.1$. The final shaping functions with associated weights of the overall controlled traslational and heading systems are represented in Figures 4.7, 4.8, 4.9, 4.10.

Note that, since the control action had already been limited in the inner loops, only the complementary and sensitivity functions have been shaped.

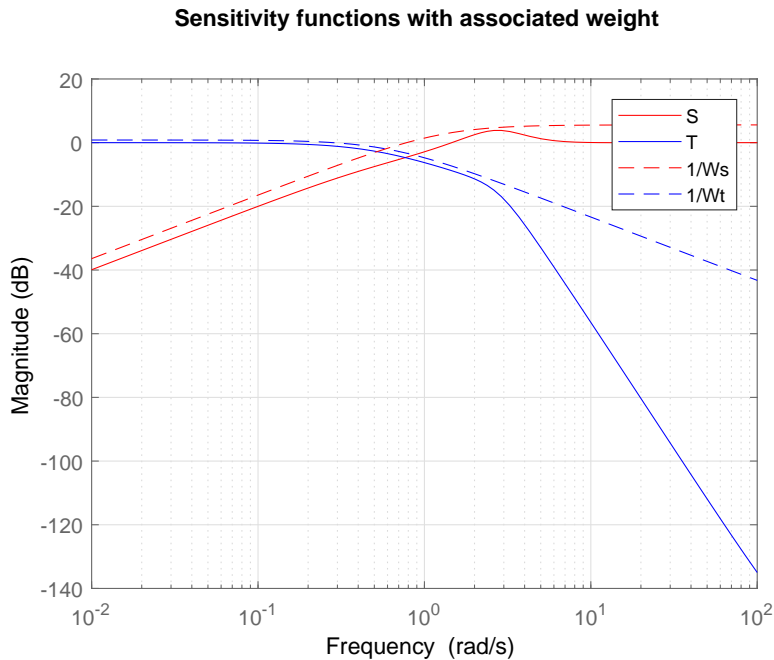


Figure 4.7: Sensitivity functions with associated weights on the North control loop

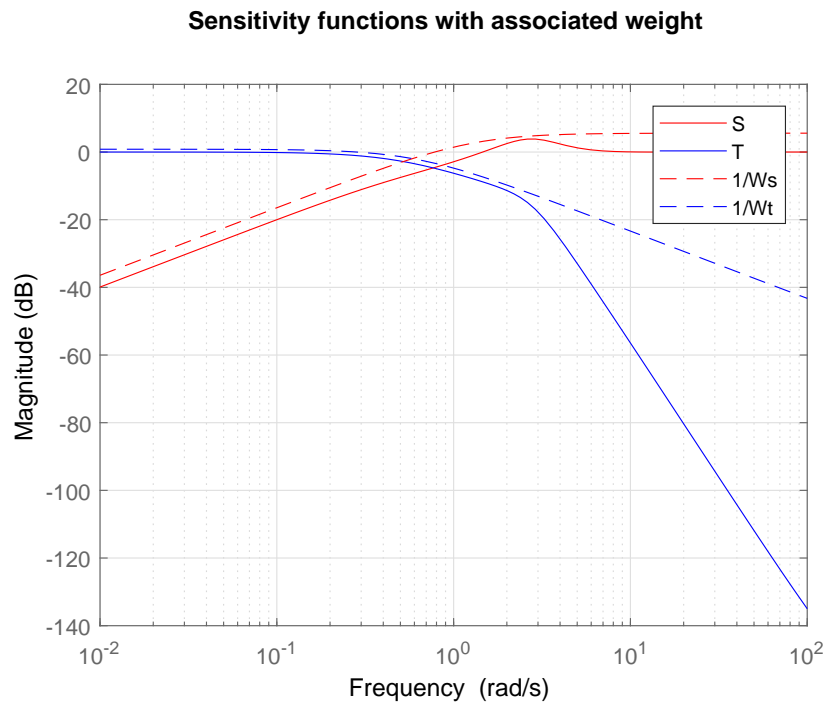


Figure 4.8: Sensitivity functions with associated weights on the East control loop.

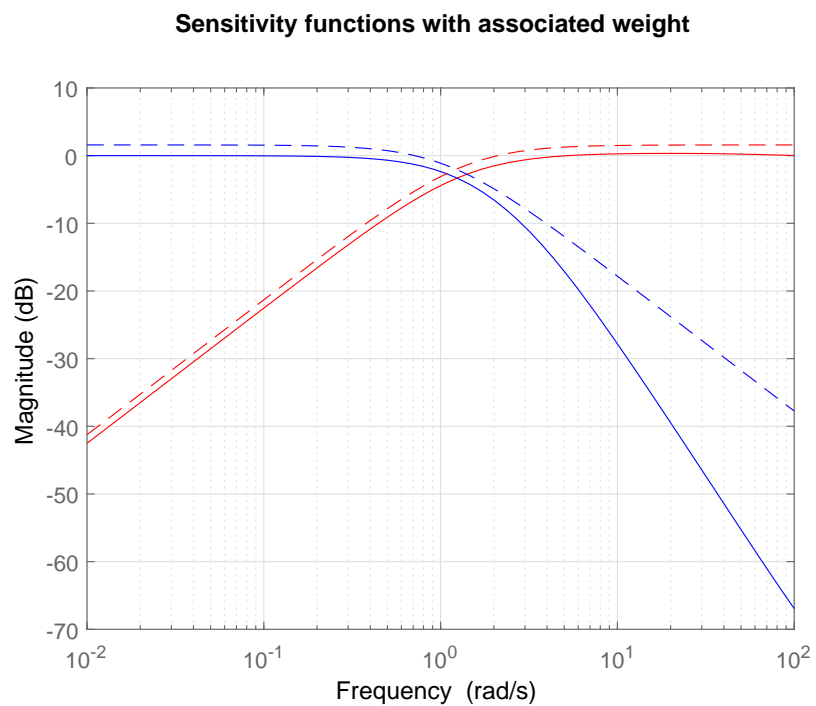


Figure 4.9: Sensitivity functions with associated weights on the altitude control loop

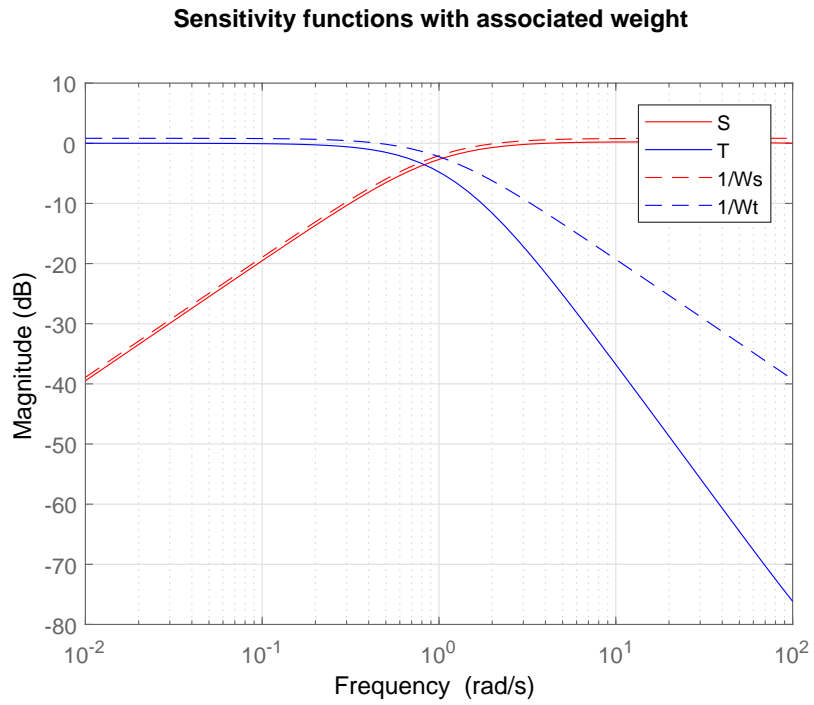


Figure 4.10: Sensitivity functions with associated weights on the yaw angle

In Table 4.2 the controllers values are listed.

	P	I	D
p	1.681	0.0	0.0
q	2.034	0.0	0.0
r	0.8948	0.0	0.0014
Φ	1.902	0.0	0.162
Θ	1.902	0.0	0.162
Ψ	0.9417	0.0	0.6117
\dot{N}	0.131	0.0	0.0855
\dot{E}	0.131	0.0	0.0855
\dot{D}	24.3	0.0002541	0.0004465
N	0.989	0.0	1.478
E	0.989	0.0	1.478
D	1.335	0.0	0.433

Table 4.2: Values of the regulators

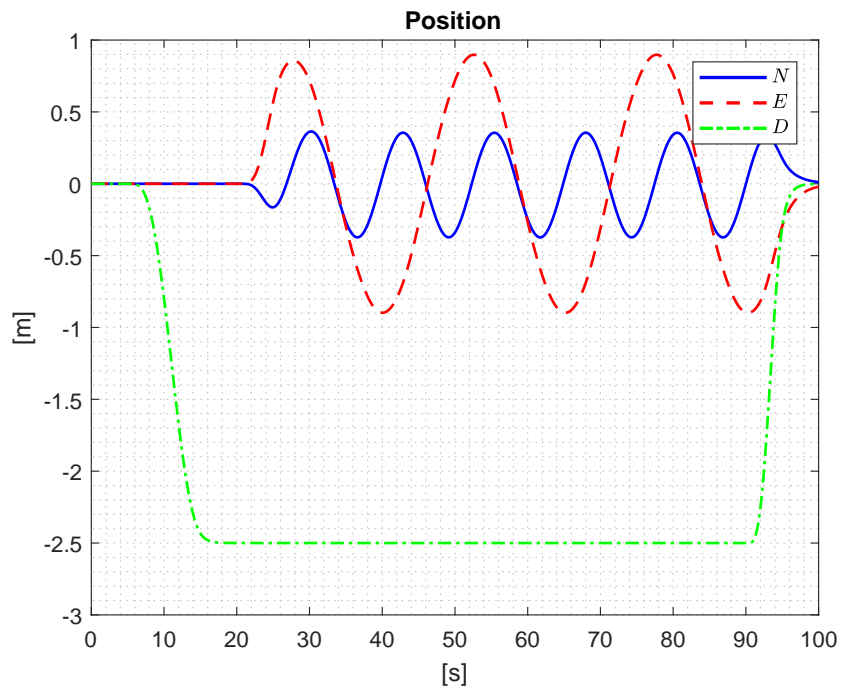
4.2.4 Hexacopter simulation results

The controllers have been implemented in the simulator in Figure 3.5. The complete model of the multicopter has been tested assigning a smooth set-point given by equation (4.13). The reference describes an eight-shape trajectory which is the Lemniscate of Bernoulli. It is defined as:

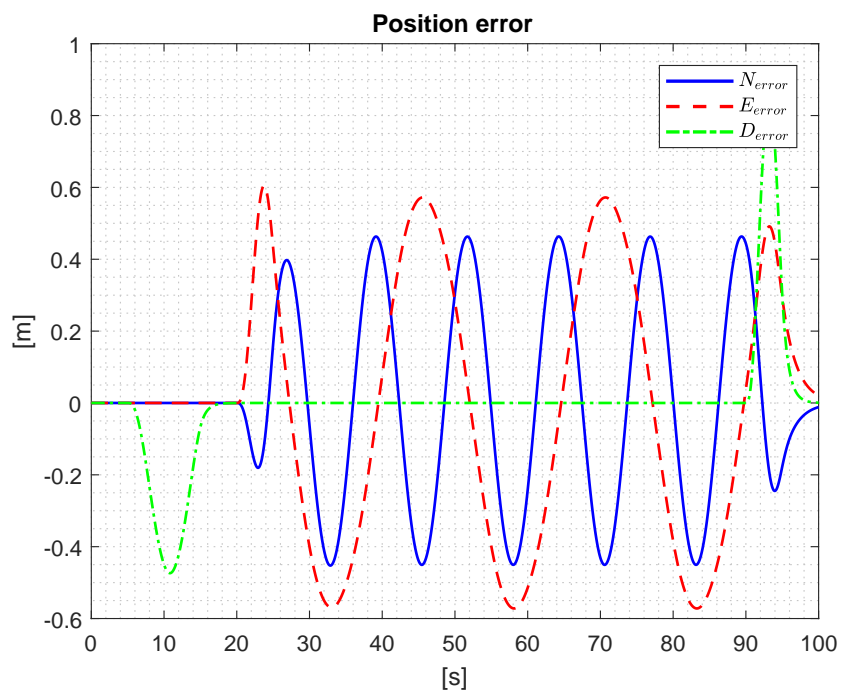
$$P_d = \begin{bmatrix} \frac{\sin(2\omega t)}{3 - \cos(2\omega t)} \\ \frac{2 \cos(\omega t)}{3 - \cos(2\omega t)} \\ h \end{bmatrix}, \quad (4.13)$$

where t is the simulation time, ω is the linear speed and h is the altitude at which the eight-shape trajectory is performed. In Figures 4.11a, 4.11b, 4.12, 4.13a, 4.13b, 4.14 and 4.15 the response of the NPPNPN multicopter configuration.

Notice that the system manages to track the dynamic set-point, even if the controllers have been tuned on the linearized system.



(a)



(b)

Figure 4.11: (a) Position of the hexacopter; (b) Position error of the hexacopter

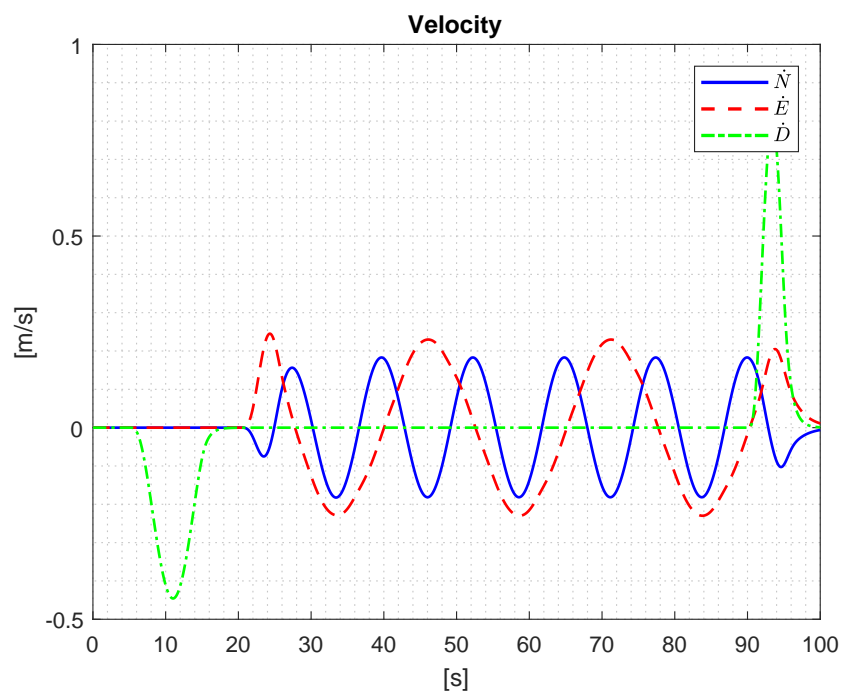
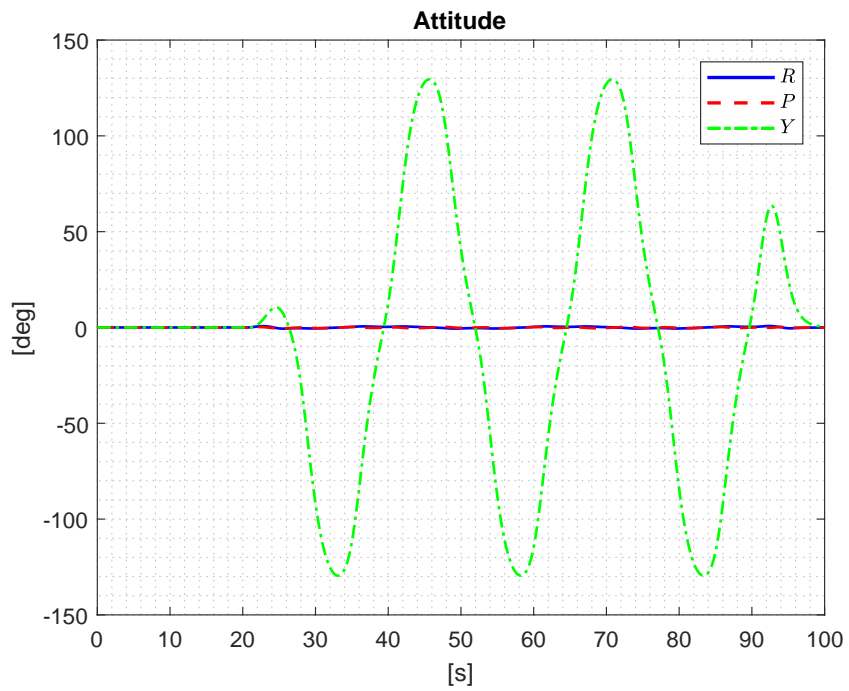
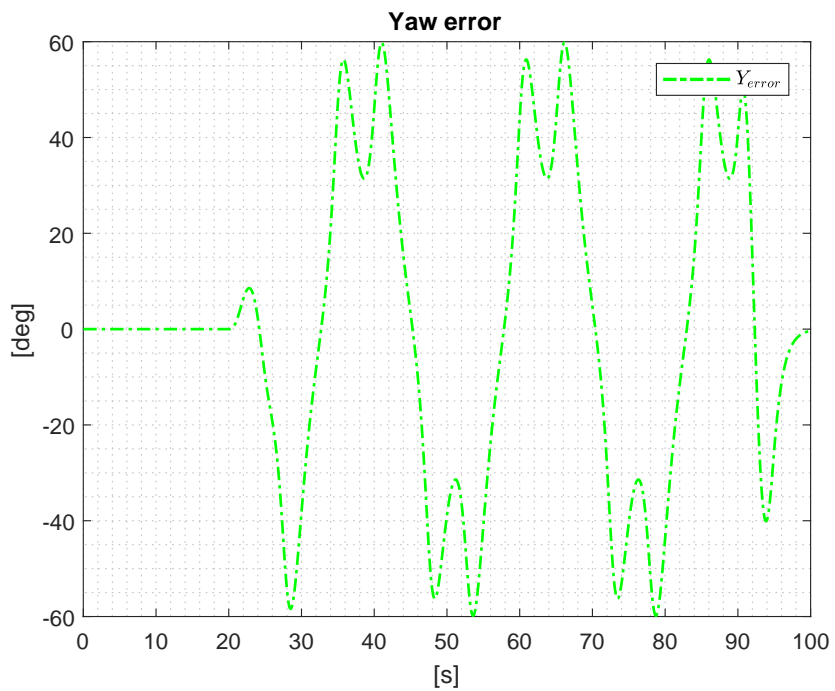


Figure 4.12: Velocity of the hexacopter



(a)



(b)

Figure 4.13: (a) Attitude of the hexacopter; (b) Yaw error of the hexacopter

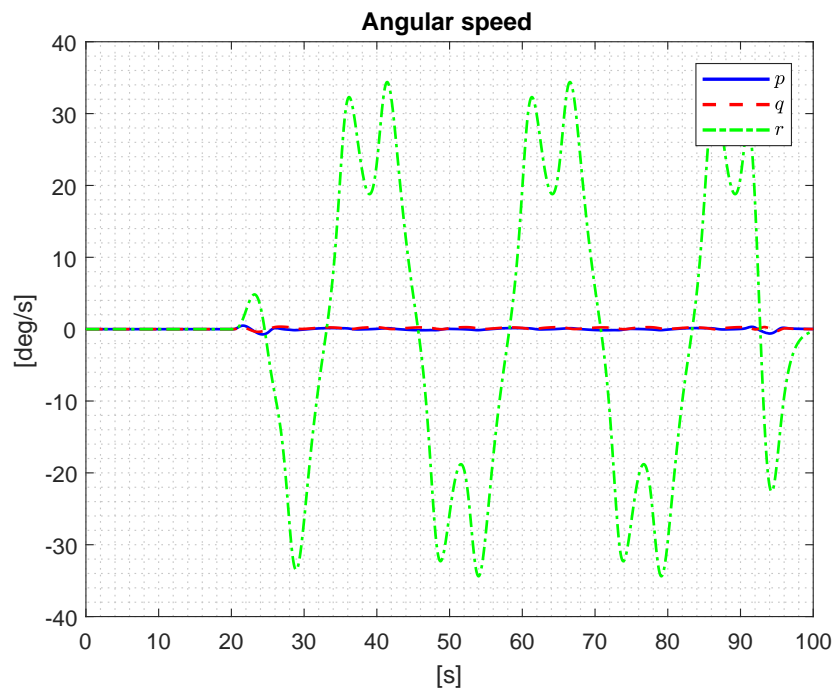


Figure 4.14: Angular speeds of the hexacopter

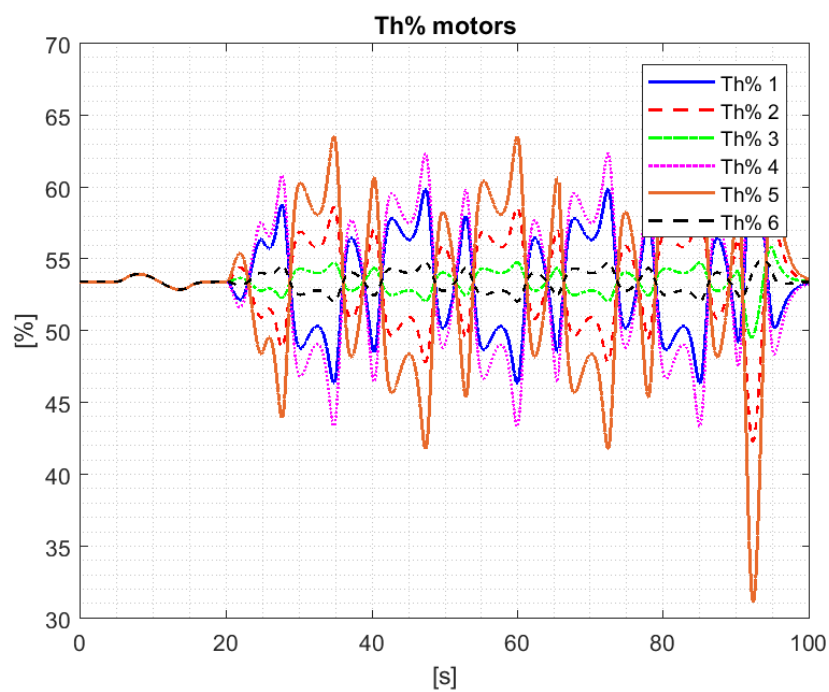


Figure 4.15: Motor thrusts of the hexacopter

4.2.5 Octocopter

The control synthesis has been performed with the same weight functions considered in Section 4.2.3. Due to the symmetry of the frame (see Chapter 3) the inertia values along the X and Y axes of the body-frame are equal. Therefore the same regulators can be applied to controll the roll and pitch angles.

Roll and Pitch control

The requirements considered, are given in terms of $\omega_b = 1.5$ rad/s, $A = 10^{-3}$, $M_s = 1.5$, $M_t = 1.5$, $\omega_{bt} = 2.25$ rad/s and $K = \pi/6$. The results are presented in Figure 4.16.

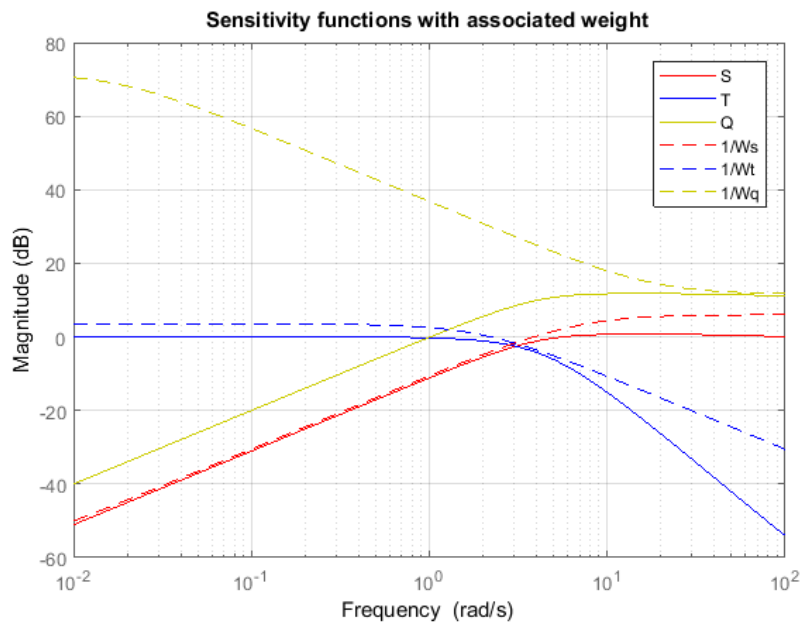


Figure 4.16: Sensitivity functions with associated weights on roll and pitch angles

Position and heading control

For North and East motion the requirements are given in terms of $\omega_b = 0.5$ rad/s, $\omega_{bt} = 0.8$ rad/s, $A = 10^{-3}$ and $M_s = 2$, $M_t = 1.1$. The heading positioning and the altitude controllers have been tuned considering the same requirements applied to the hexacopter ones.

Figures 4.17, 4.18 and 4.19 depict the sensitivity functions with associated weights computed for the North/East, altitude and yaw closed loops.

In the end, Table 4.3 shows the values of the PID regulators.

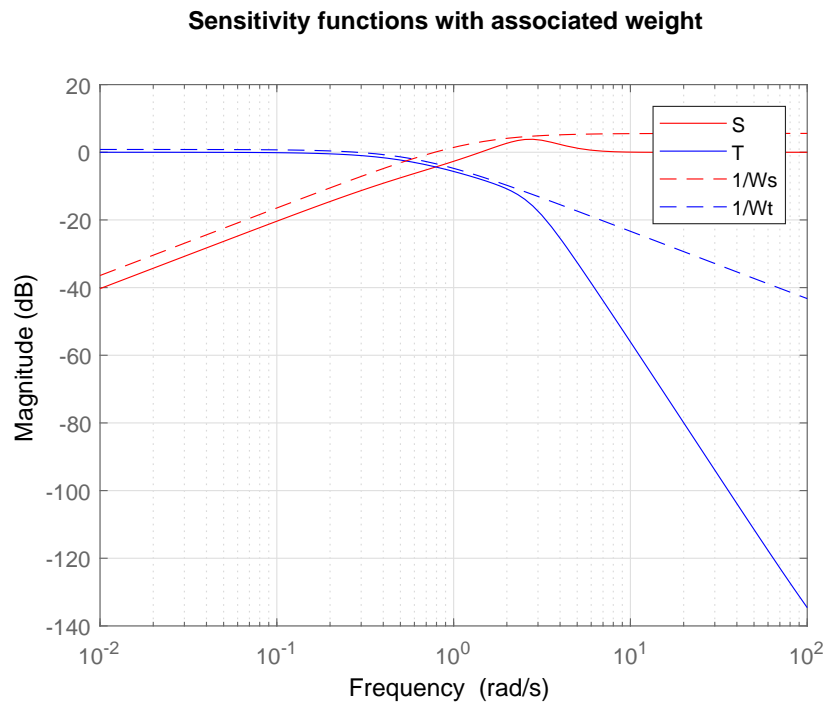


Figure 4.17: Sensitivity functions with associated weights on the North control loop and East control loops

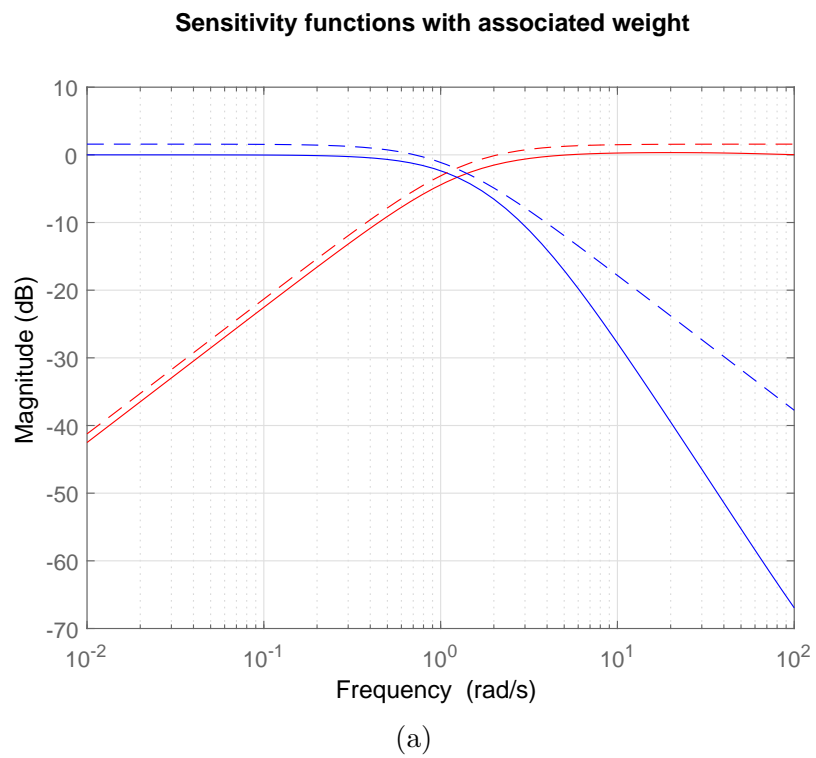


Figure 4.18: Sensitivity functions with associated weights on altitude control loop

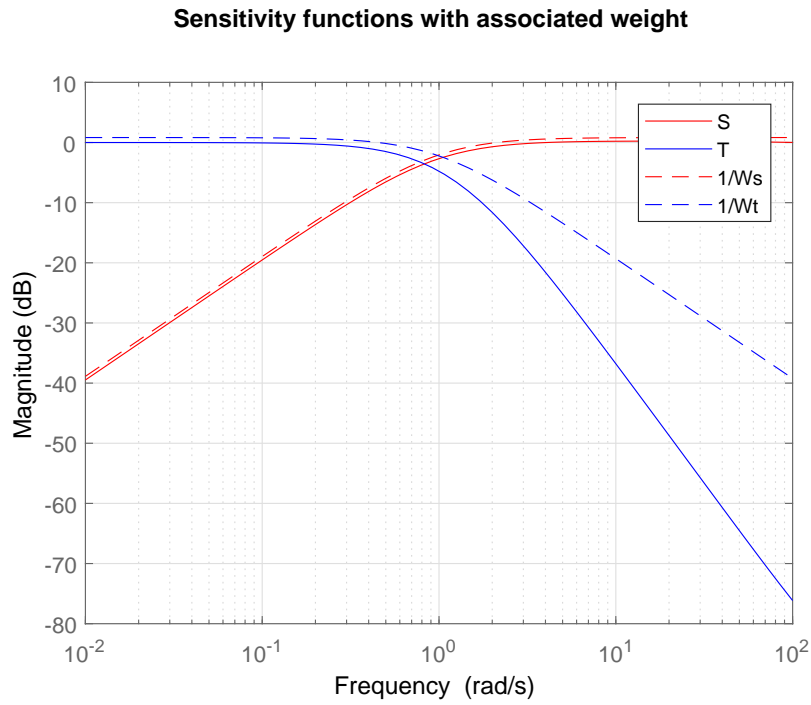


Figure 4.19: Sensitivity functions with associated weights on the yaw angle

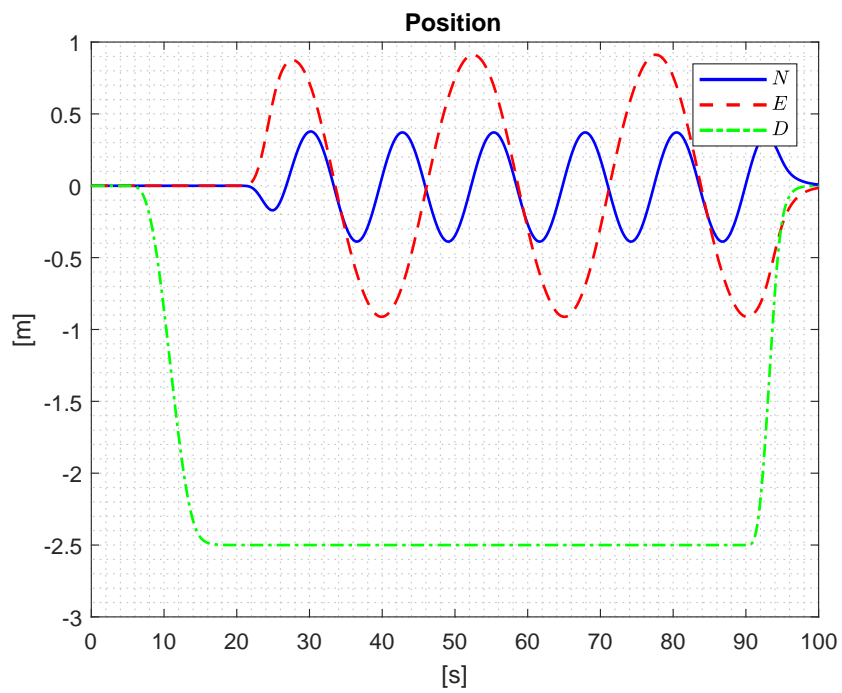
	P	I	D
p	2.948	0.0	0.0
q	2.948	0.0	0.0
r	1.441	0.0	0.002
Φ	1.902	0.0	0.1617
Θ	1.902	0.0	0.1617
Ψ	0.942	0.0	0.612
\dot{N}	0.131	0.0	0.08549
\dot{E}	0.131	0.0	0.08549
\dot{D}	25.82	0.0002582	0.0003829
N	1.035	0.0	1.438
E	1.035	0.0	1.438
D	1.336	0.0	0.4323

Table 4.3: Values of the regulators

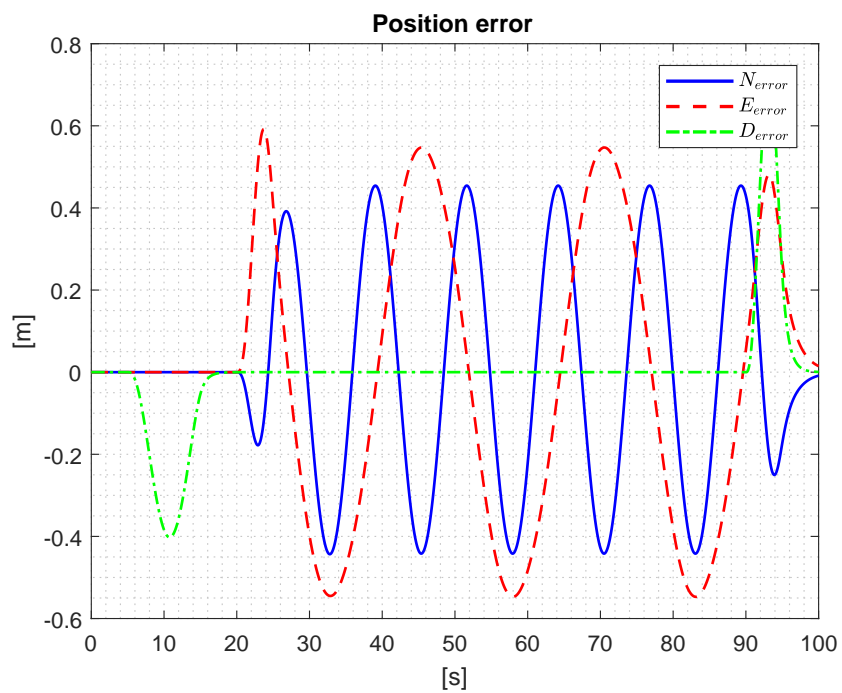
4.2.6 Octocopter simulation results

The complete model of the multicopter is tested assigning a smooth set-point given by equation (4.13) as function of time. The response of the O_2 multicopter configuration is reported in Figures 4.20a, 4.20b, 4.21 4.22a, 4.22b, 4.23 and 4.24.

Notice that the throttles of the motors (Figure 4.24) are in general smaller respect to the hexarotor ones (Figure 4.15). This is in accordance with the assumptions made during the sizing.



(a)



(b)

Figure 4.20: (a) Position of the hexacopter; (b) Position error of the octocopter

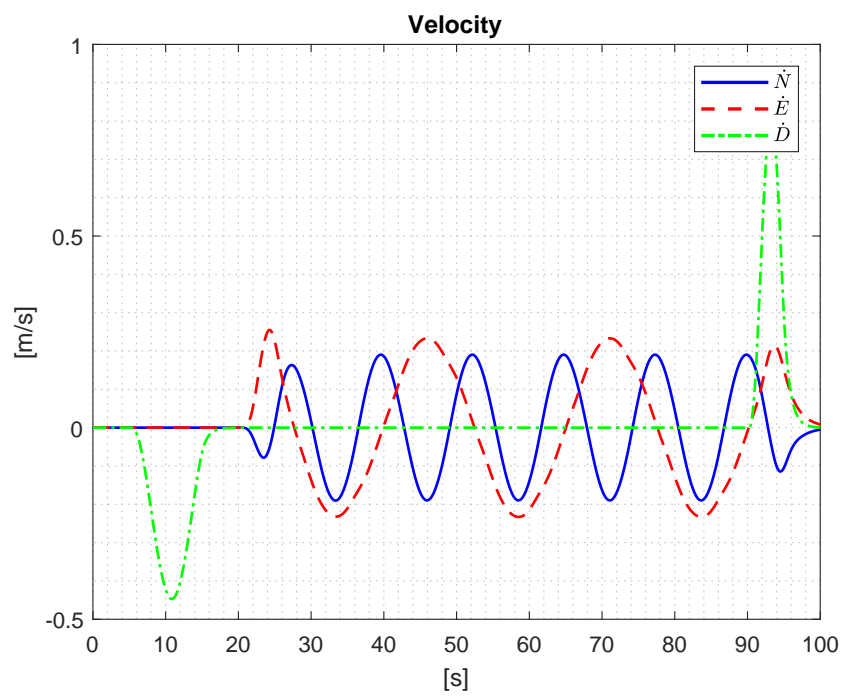
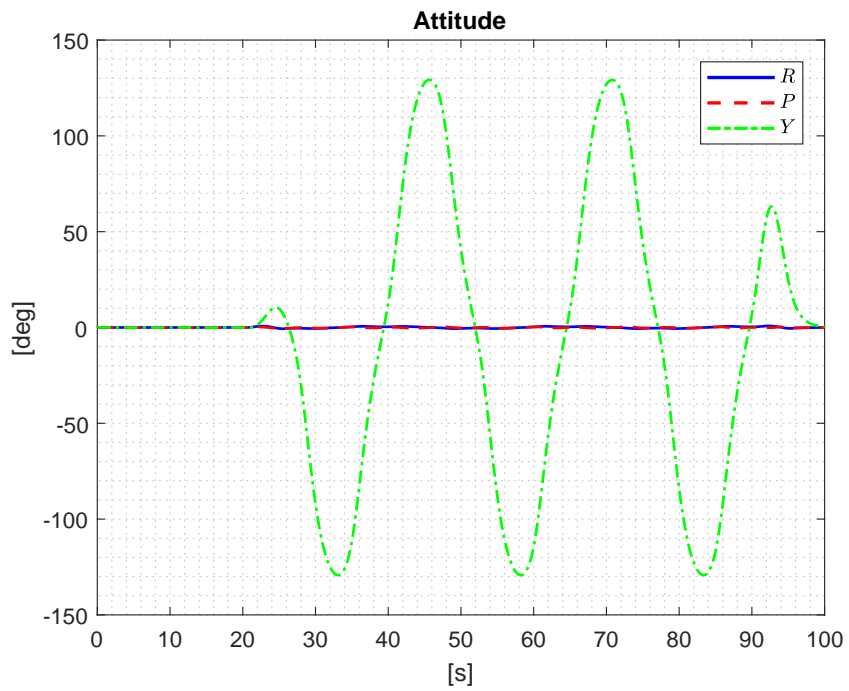
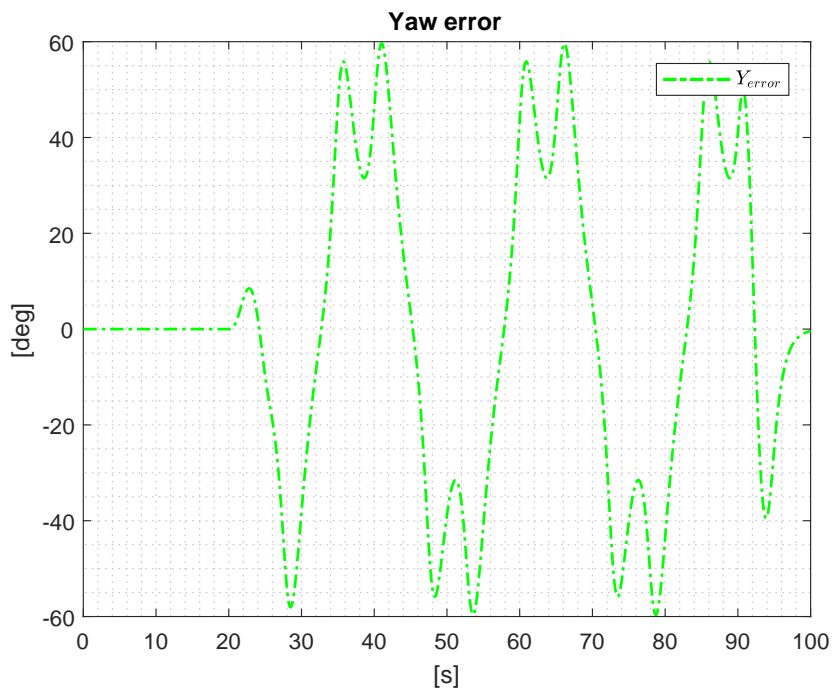


Figure 4.21: Velocity of the octocopter



(a)



(b)

Figure 4.22: (a) Attitude of the octocopter; (b) Yaw error of the octocopter

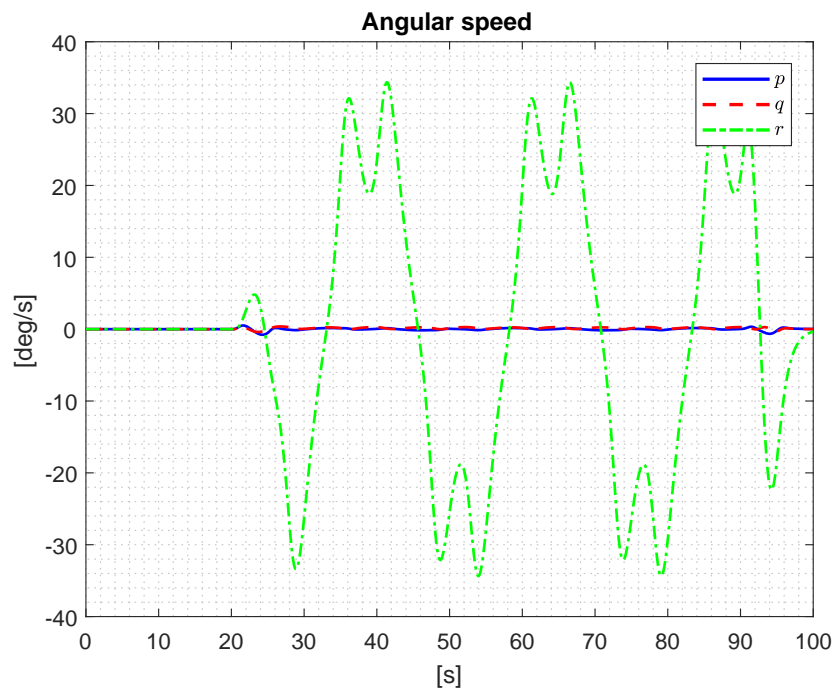


Figure 4.23: Angular speeds of the octocopter

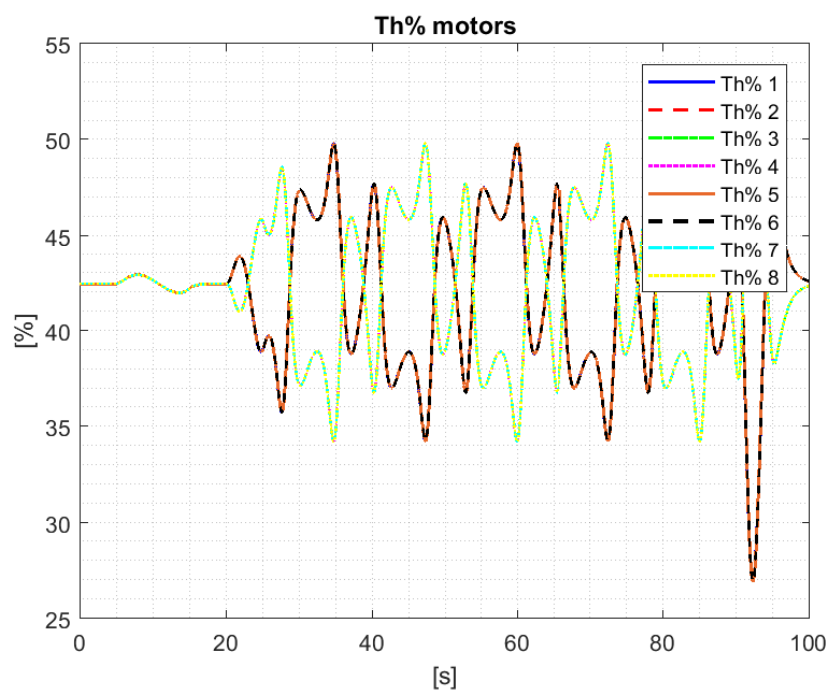


Figure 4.24: Motor thrusts of the octocopter

4.3 Drift analysis of the vision system

In a stereo camera the drift phenomenon of the position respect to an Earth-reference system is caused by multiple factors:

- Lighting
- Velocity
- Environment.

Therefore, the problem of quantifying the drift can be very complex. A simplified model of the drift has been taken into account to understand its influence on the control system and if the controller is able to reject this disturbance. Equation (4.14) describes a first order Markov process, where P_e is the absolute position of the aircraft (in NED), \tilde{P}_e is the estimated position, η_v and η_w two white Gaussian noises with zero mean and spectral densities σ_v^2 and σ_w^2 , respectively. η_v and η_w are commonly defined as random walk (RW) and rate random walk (RRW).

$$\begin{aligned}\tilde{P}_e &= P_e + \beta + \eta_v, \\ \dot{\beta} &= \eta_w, \quad \beta(0) = \beta_0.\end{aligned}\tag{4.14}$$

Moreover, β is the drift, while its initial condition (β_0) represents the bias. In general, the smaller RW, the less will be the white noise on the measurement; the smaller RRW the slower will be the drift.

Since the Guidance vision system works at a frequency equal to 20 Hz, a discrete form of the drift model (with Gaussian noises η_{wd} and η_{vd}) has been applied to the feedback chain of a quadrotor Simulator (Figure 4.25) which adopts the same control schemes and PID structure seen in Section 4.2.2.

Henceforward, σ_{wd} and σ_{vd} will be the standard deviation of the Gaussian rate random walk and the standard deviation of the random walk measured in meters. Furthermore the values of σ_{wd} and σ_{vd} characterize the disturbance acting on the feedback chain.

Since the monitoring platform should move inside an industrial plant to effect measurements, a trapezoidal velocity reference has been generated.

The set-point profile can be summarised as follows, the aircraft takes-off up an altitude of 2.5 m, then it constantly accelerates in North direction (for 10 seconds) until a constant velocity (1 m/s). The motion continues for a distance equal to 200 m. In the end, it decelerates constantly.

The noise free position response of the closed loop system to the set-point is given in Figure 4.26a. While the trapezoidal profile of the velocity is shown in Figure 4.27.

Notice that, the North position error (Figure 4.26b) is constant (about 1 m) when the ramp is present. To improve the response, the position regulator was tuned.

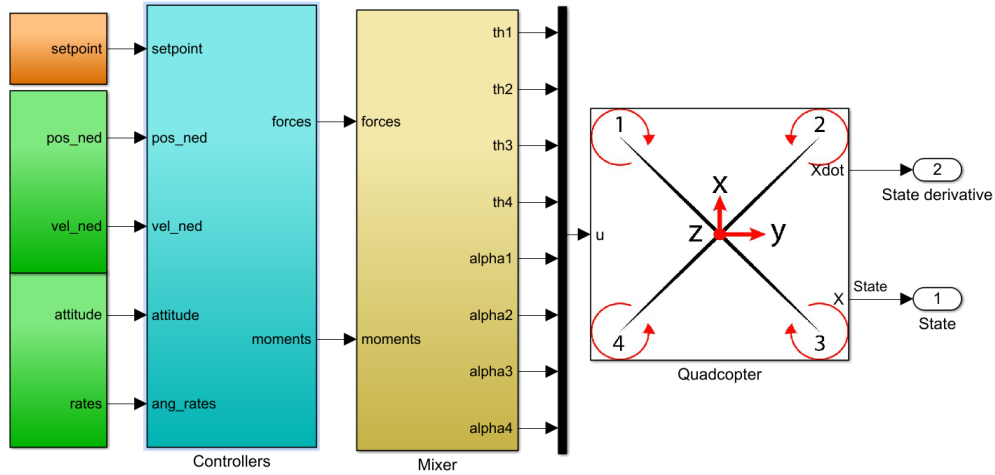


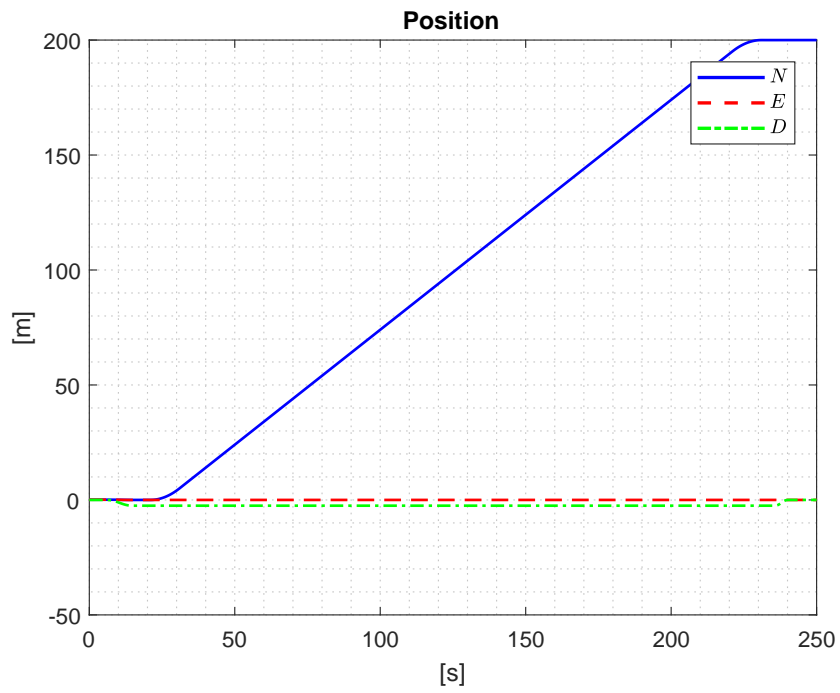
Figure 4.25: Overall simulator of the quadrotor

Indeed, once computed the bode diagram of the North velocity closed loop (see Figure 4.28), a PI position controller has been tuned requiring a cut-off frequency of 0.8 rad/s for the open loop transfer function. Successively, the values obtained ($K_p = 0.8$ and $K_i = 0.064$) have been used to initialize the H_∞ procedure whose subject was the the position PID controller given by equation (4.8). Furthermore, the sensitivity function has been weighted considering:

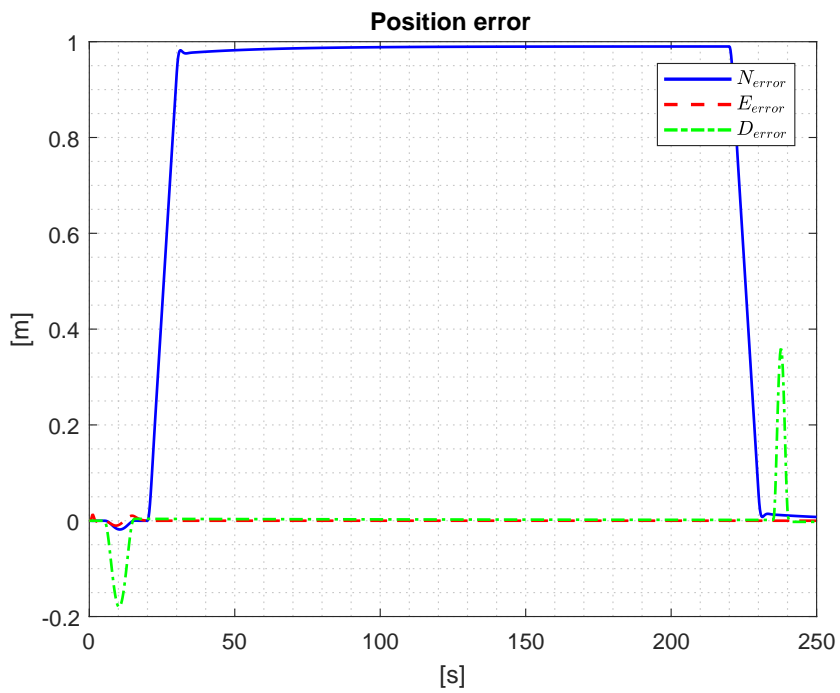
$$W_s = \frac{(s/M_s + p)(s/M_s + 0.1p)}{(s + Ap)(s + 0.1Ap)}, \quad (4.15)$$

with $A = 10^{-6}$ (to attenuate the tracking error), $w_b = 0.65$ rad/s (the bandwidth of W_s^{-1}) and $M_s = \sqrt{1.5}$. The weight on the complementary sensitivity function is defined according to equation (4.12), with $w_{bt} = 1.3$ rad/s, $A = 10^{-3}$ and $M_t = 1.2$. The final shaping functions and their weights are reported in Figure 4.29, while the controller parameters found are: $K_p = 1.08$, $K_i = 0.262$ and $K_d = 0.334$.

The controller has then been implemented on the simulator of the quadcopter; the position behaviour (see Figures 4.30a, 4.30b) shows that the system manages to follow the ramp keeping a constant error of about 0.01 m.



(a)



(b)

Figure 4.26: (a) Position of the quadcopter; (b) Position error of the quadcopter

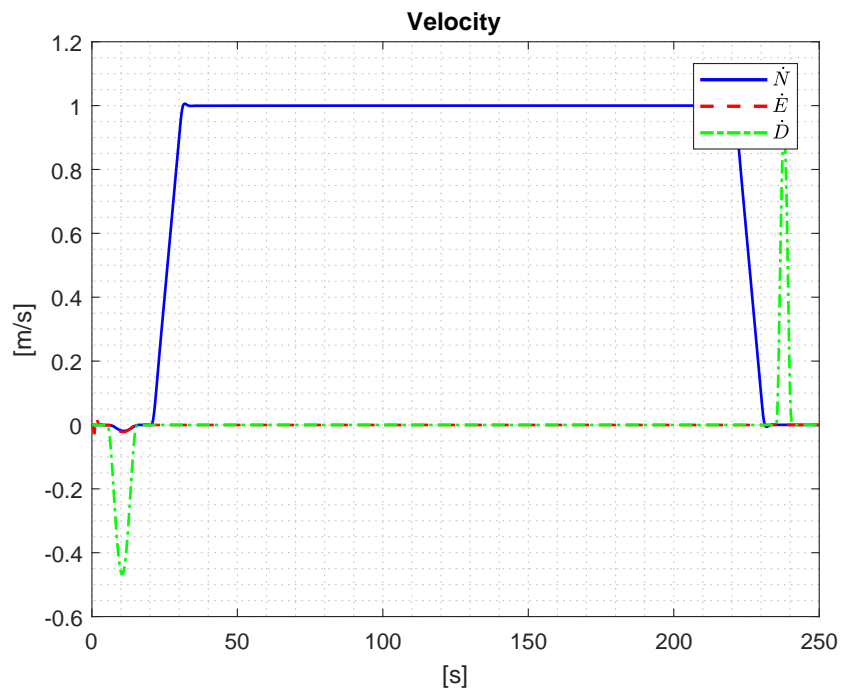


Figure 4.27: Velocity of the quadcopter

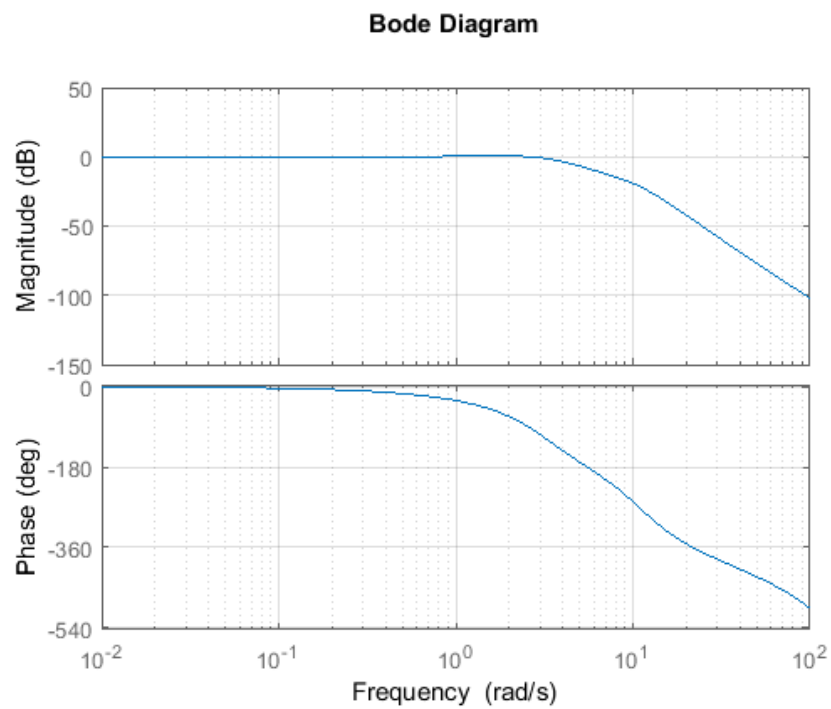


Figure 4.28: Bode diagram on the North velocity control loop

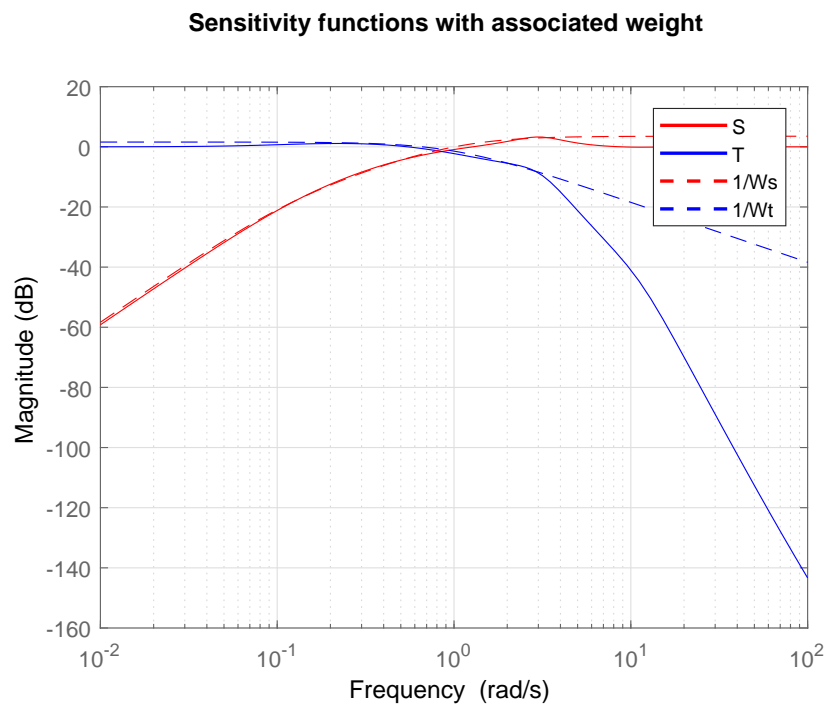
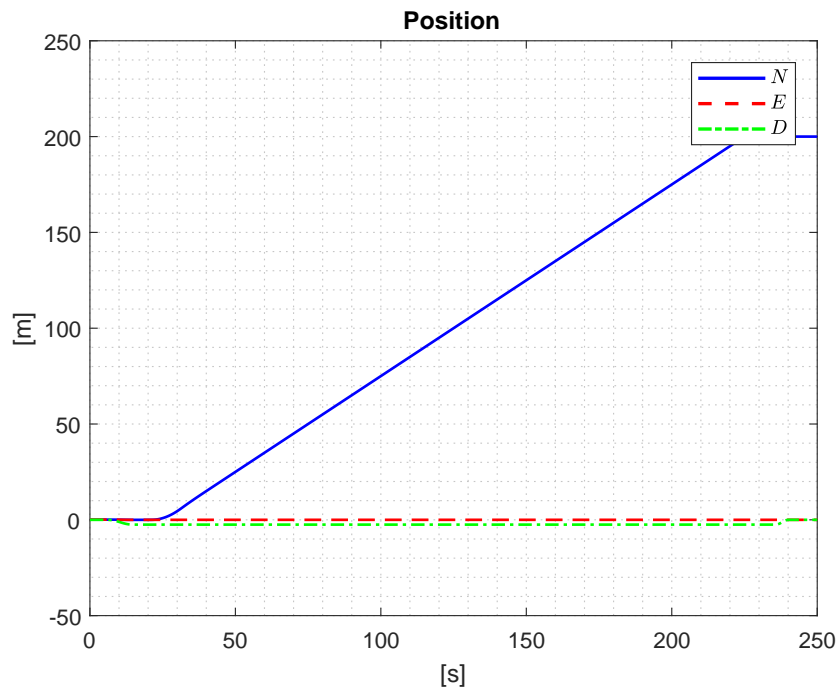
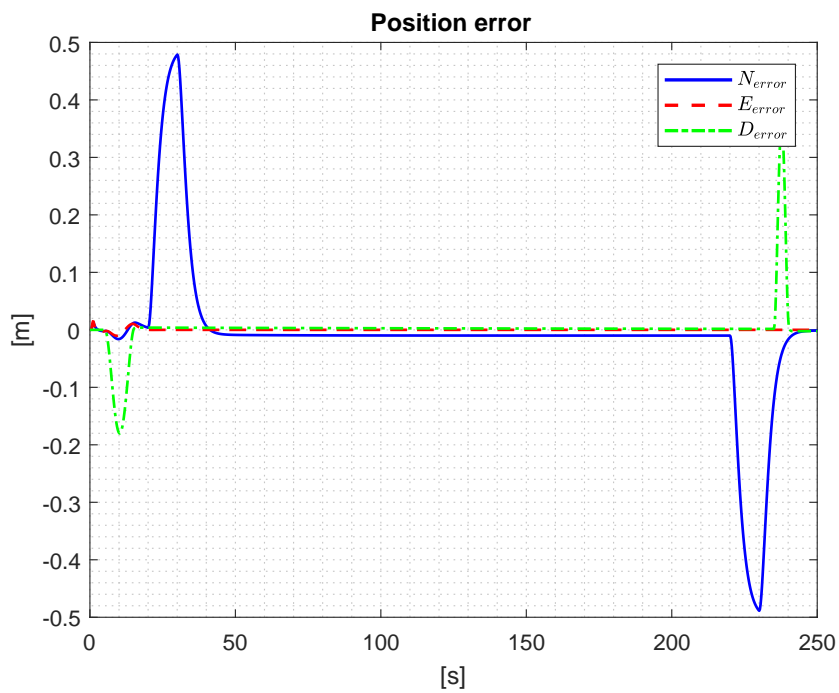


Figure 4.29: Sensitivity functions with associated weights on the North control loop



(a)



(b)

Figure 4.30: (a) Position of the quadcopter after tuning; (b) Position error of the quadcopter after tuning

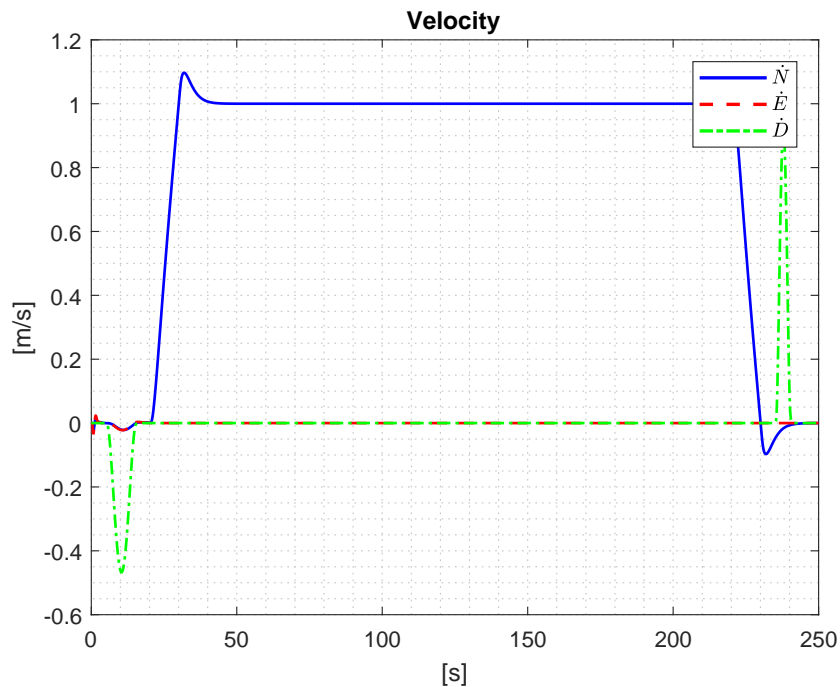


Figure 4.31: Velocity of the quadcopter after tuning

In [6] a comprehensive comparison of publicly-available monocular visual-inertial algorithms typically used on flying robots is addressed. The authors managed to compute (for each one of the visual inertial algorithms considered) the final translational error of the flying robot respect to the distance travelled. From [6], the mean of the translational errors data of the most and the worst performant VIO algorithms (VINS-mono and SVO+MSF respectively) tested on different platforms have been taken into account (see Table 4.4).

	VINS-MONO		SVO+MMSF	
Distance travelled [m]	7	35	7	35
Error [m]	0.38	0.57	1.45	1.6

Table 4.4: Translational errors respect to distance travelled given by VINS-MONO and SVO+MSF

The points given by the couple, distance travelled and translational error (in Table 4.4) have been interpolated to define the lower bound (given by VINS-mono) and the upper limit (by SVO+MSF) on the values of translational error respect to the distance travelled for a generic VIO algorithm. Then, different tests have been run on the quadrotor system simulator according to the following assumptions:

- the noise acts with same intensity (in terms of $\sigma_{RW} = \sigma_{vd}$ and $\sigma_{RRW} = \sigma_{wd}$) on all the three axes NED;
- the values of σ_{vd} and σ_{wd} have been considered in the order of centimeters or decimeters.

Consequently, the effect of the drift on the system has been evaluated by computing the absolute value of the difference between the noisy position error e_n and the noise free position error e_i (no drift applied on the system). The results are given in Figures 4.32, 4.33 and 4.34.

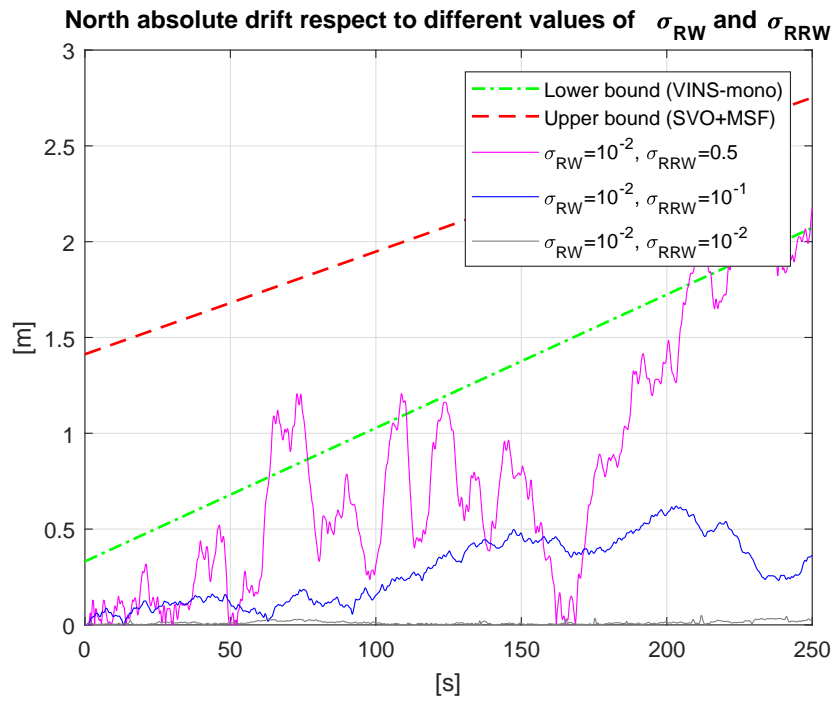


Figure 4.32: Absolute North translational error due to the drift and for different values of σ_{RW} and σ_{RRW}

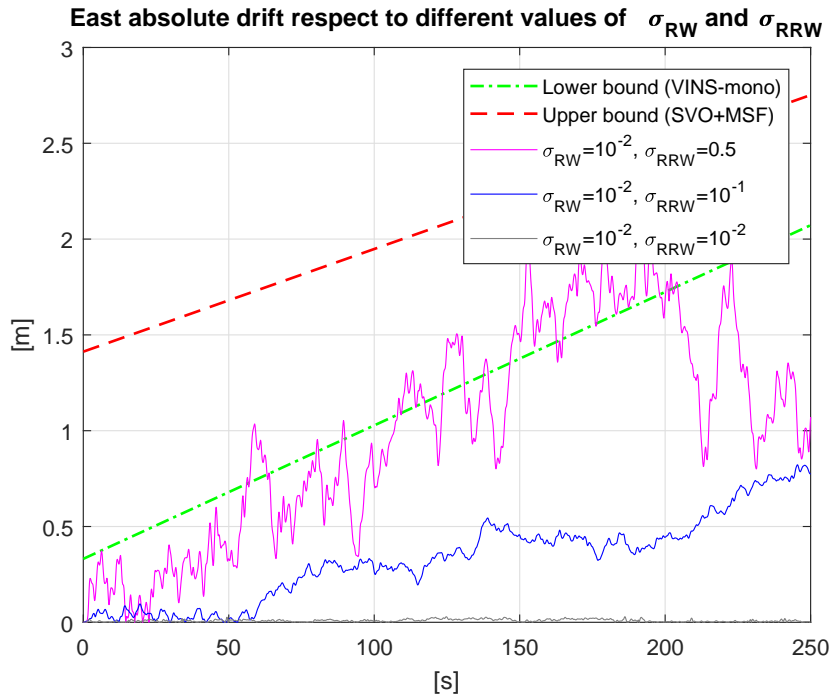


Figure 4.33: Absolute East translational error due to the drift and for different values of σ_{RW} and σ_{RRW}

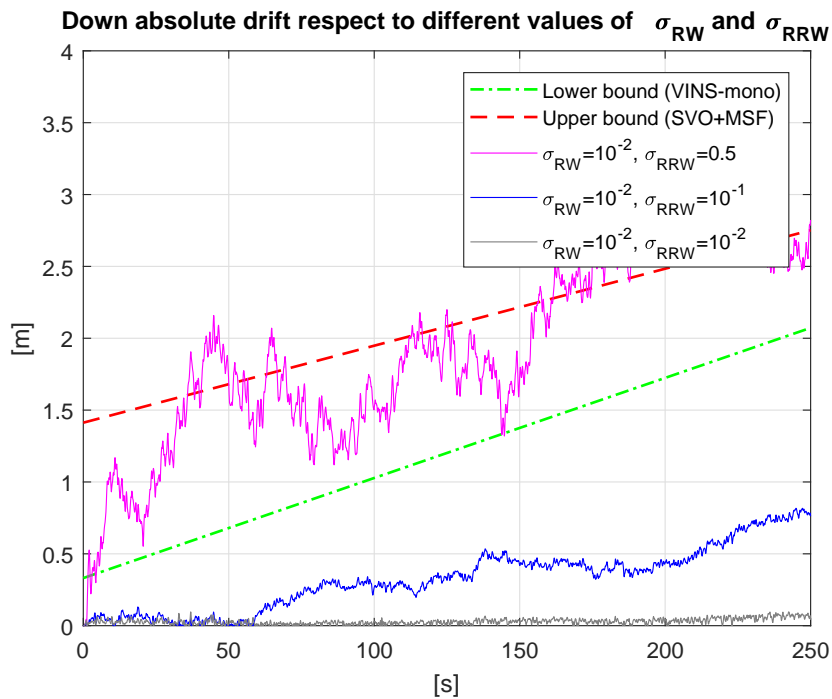


Figure 4.34: Absolute translational error on the altitude due to the drift and for different values of σ_{RW} and σ_{RRW}

Since the Guidance is a professional vision system composed by five stereocameras it is reasonable to assume that it would introduce a drift in the position with values below the lower limit (green dotted line in Figures 4.32, 4.33 and 4.34). Notice that, thanks to this assumption, and fixing the value of $\sigma_{vd} = \sigma_{RW} = 10^{-2}$, the value of $\sigma_{wd} = \sigma_{RRW}$ has to be lower than 0.5 (see Figures 4.32, 4.33 and 4.34). Furthermore, if $\sigma_{vd} = 10^{-2}$, $\sigma_{wd} = 10^{-1}$ and the purpose is to avoid drifts bigger than 0.5 m, the aircraft should not fly for more than 200 m.

Chapter 5

Fault tolerance analysis

Many approaches exist to study the capability of fault tolerance against rotor or motor in UAVs. In this work the results of a structural reconfigurability analysis (see [1]) will be applied to investigate the static controllability of the system in fault configuration; then a pseudo-inverse control allocator will be developed and tested on the multicopter simulator.

5.1 Basic concepts

Fault tolerant control (FTC) aims at increasing the availability of technical processes subject to faults or failures. In FTC a diagnosis unit has to detect and isolate the fault f . Once a fault has been isolated three cases can occur:

- If it is negligible, it is not necessary to redesign the existing control system, which should possess an intrinsic robustness (passive fault tolerance);
- If it is significant, but not too critical, it is possible to modify the control parameters without modifying its structure (active fault tolerance, adaptive systems);
- If the fault is critical, such as break of sensors or actuators, it is necessary to reconfigure the system (active fault tolerance).

The scheme reported in Figure 5.1 presents an active FTC scheme. The diagnoser isolates the fault and then a reconfiguration unit adapts the controller. Whether a system can be reconfigured or not depends on the physical structure and the presence of redundancies. The availability of such redundancy is the purpose of a reconfigurability analysis. In this work the consequences of a complete loss of a rotor are analysed. The desired control position which has to be recovered after a

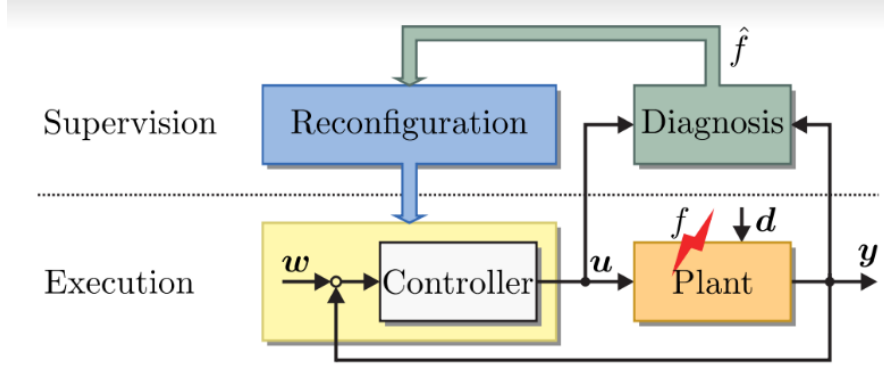


Figure 5.1: Active fault control scheme (see [1])

rotor failure is the hover flight. The reconfiguration is performed by using a LVA (Linear Virtual Actuator). Given a linear time-invariant (LTI) system:

$$\begin{cases} \dot{x} = Ax + Bu & x(0) = x_0 \\ y = Cx \end{cases} \quad (5.1)$$

where the state is denoted by $x \in \mathbb{R}^n$, the input by $u \in \mathbb{R}^m$ and the output $y \in \mathbb{R}^r$; the actuator failure is modelled by the faulty plant:

$$\begin{cases} \dot{x}_f = Ax_f + B_f u_f & x(0) = x_0 \\ y_f = Cx_f. \end{cases} \quad (5.2)$$

B_f is the faulty input matrix obtained from B where the column corresponding to the failed actuator is set to zero. In order to be able to use a LVA:

$$u_f = Nu, \quad N = B_f^+ B, \quad (5.3)$$

there must be proven that $\text{rank}(B_f) = \text{rank}(B_f B)$ with $B_f N = B$.

5.2 Application

According to [1] the linear model of a multicopter in hovering condition, can be written in dependency of the rotor speeds (see also [7]) $u_i(t) = \Omega_i(t)^2$. The LTI model of the system presents the following structure:

$$\delta \dot{x}(t) = A \delta x(t) + \begin{bmatrix} 0_{5 \times N_r} \\ \tilde{B} \\ 0_{3 \times N_r} \end{bmatrix} \delta u(t) \quad (5.4)$$

where the state vector $\delta x(t)$ and the matrix $A \in \mathbb{R}^{n \times n}$ can be obtained by the equations in Section 4.1. The input vector $\delta u(t) \in \mathbb{R}^{N_r}$ contains the N_r variables

$\delta u_i(t) = \Omega_i(t)^2 - \bar{\Omega}_i^2$, where $\bar{\Omega}_i = \sqrt{\frac{mg}{K_T N_r}}$ and N_r is the number of rotors. While \tilde{B} coincides with the mixer matrix of the multicopter multiplied by the diagonal matrix J^{-1} :

$$J^{-1} = \begin{bmatrix} 1/m & 0 & 0 & 0 \\ 0 & 1/I_{xx} & 0 & 0 \\ 0 & 0 & 1/I_{yy} & 0 \\ 0 & 0 & 0 & 1/I_{zz} \end{bmatrix}. \quad (5.5)$$

Notice that, as seen in Chapter 3 the mixer matrix strictly depends on the structure of the unmanned aerial vehicle and on the direction of rotation of the rotors (clockwise or counter-clockwise). Therefore, (as described in [1]) matrix \tilde{B} is taken into account to analyse the reconfigurability of multirotors.

In this thesis the configurations shown in Figures 3.2a 3.2b (with mixer matrices (3.33), (3.34), respectively) and in Figures 3.3a 3.3b (with mixer matrices (3.37), (3.38) respectively) have been studied.

The application of the reconfigurability analysis is fully described for the PNPNP hexacopter, with mixer matrix χ_{H_1} . While only the results will be presented for the other configurations.

Renaming as $\tilde{B} = B_{H_1} = J^{-1}\chi_{H_1}$, the result is:

$$B_{H_1} = \begin{bmatrix} -\frac{K_T}{m} & -\frac{K_T}{K_T a} & -\frac{K_T}{K_T a} & -\frac{K_T}{K_T a} & -\frac{K_T}{K_T a} & -\frac{K_T}{K_T a} \\ -\frac{I_{xx}}{K_T b} & \frac{I_{xx}}{I_{xx}} & -\frac{I_{xx}}{K_T b} & \frac{I_{xx}}{K_T b} & \frac{I_{xx}}{I_{xx}} & \frac{I_{xx}}{K_T b} \\ \frac{I_{yy}}{K_Q} & 0 & -\frac{I_{yy}}{K_Q} & -\frac{I_{yy}}{K_Q} & 0 & \frac{I_{yy}}{K_Q} \\ \frac{K_Q}{I_{zz}} & -\frac{K_Q}{I_{zz}} & \frac{K_Q}{I_{zz}} & -\frac{K_Q}{I_{zz}} & \frac{K_Q}{I_{zz}} & -\frac{K_Q}{I_{zz}} \end{bmatrix}, \quad (5.6)$$

which can be rewritten in a more compact form as:

$$B_{H_1} = \begin{bmatrix} -K_z & -K_z & -K_z & -K_z & -K_z & -K_z \\ -K_r a & -K_r a & -K_r a & K_r a & K_r a & K_r a \\ K_p b & 0 & -K_p b & -K_p b & 0 & K_p b \\ K_y & -K_y & K_y & -K_y & K_y & -K_y \end{bmatrix}, \quad (5.7)$$

with $K_z = \frac{K_T}{m}$, $K_r = \frac{K_T}{I_{xx}}$, $K_p = \frac{K_T}{I_{yy}}$ and $K_y = \frac{K_Q}{I_{zz}}$.

Matrix B_{H_1} multiplies the input vector:

$$\delta u(t) = [\delta u_1(t) \quad \delta u_2(t) \quad \delta u_3(t) \quad \delta u_4(t) \quad \delta u_5(t) \quad \delta u_6(t)]^T. \quad (5.8)$$

Therefore, in the operating point it must hold that $B\delta\bar{u} = 0_{4 \times 1}$; which means

that:

$$\begin{cases} \sum_{i=1}^6 -K_T \bar{u}_i = -mg \\ -K_r a \bar{u}_1 - K_r a \bar{u}_2 - K_r a \bar{u}_3 + K_r a \bar{u}_4 + K_r a \bar{u}_5 + K_r a \bar{u}_6 = 0 \\ K_p b \bar{u}_1 - K_p b \bar{u}_3 - K_p b \bar{u}_4 + K_p b \bar{u}_6 = 0 \\ K_y \bar{u}_1 - K_y \bar{u}_2 + K_y \bar{u}_3 - K_y \bar{u}_4 + K_y \bar{u}_5 - K_y \bar{u}_6 = 0. \end{cases} \quad (5.9)$$

As performed in [1] matrix B_{H_1} is reduced row by row (applying a Gaussian elimination algorithm on the last three rows). The result is a reduced matrix V s.t. the new virtual input vector is $\delta v(t) = V \delta u(t)$. Then a 4×4 matrix $B^v_{H_1}$ is computed to ensure $B_{H_1} = B^v_{H_1} V$. This solution allows to find a minimal form of the relations between $\delta v(t)$ and $\delta u(t)$ and to simplify the system reconfigurability analysis. Considering B_{H_1} , the virtual inputs are given by:

$$\begin{cases} \delta v_1(t) = \sum_{i=1}^6 \delta u_i(t) \\ \delta v_2(t) = \delta u_1(t) - \delta u_4(t) \\ \delta v_3(t) = \delta u_2(t) - \delta u_5(t) \\ \delta v_4(t) = \delta u_3(t) - \delta u_6(t) \end{cases} \quad (5.10)$$

which can be also written as:

$$\begin{cases} \delta v_1(t) = v_1(t) - \bar{v}_1 = \sum_{i=1}^6 u_i(t) - \frac{mg}{K_T} \\ \delta v_2(t) = v_2(t) - \bar{v}_2 = u_1(t) - u_4(t) \\ \delta v_3(t) = v_3(t) - \bar{v}_3 = u_2(t) - u_5(t) \\ \delta v_4(t) = v_4(t) - \bar{v}_4 = u_3(t) - u_6(t). \end{cases} \quad (5.11)$$

Notice that $\bar{v}_1 = \frac{mg}{K_T}$ while $\bar{v}_i = 0$ for $i = 2, 3, 4$. Then the new matrix $B^v_{H_1}$ is:

$$B^v_{H_1} = \begin{bmatrix} -K_z & 0 & 0 & 0 \\ 0 & -K_r a & -K_r a & -K_r a \\ 0 & K_p b & 0 & -K_p b \\ 0 & K_y & -K_y & K_y \end{bmatrix}. \quad (5.12)$$

Moreover in the operating point:

$$\begin{cases} \bar{v}_1 = \sum_{i=1}^6 \bar{u}_i = \frac{mg}{K_T} \\ \bar{v}_2 = \bar{u}_1 - \bar{u}_4 = 0 \\ \bar{v}_3 = \bar{u}_2 - \bar{u}_5 = 0 \\ \bar{v}_4 = \bar{u}_3 - \bar{u}_6 = 0. \end{cases} \quad (5.13)$$

The virtual inputs and the reduced matrix $B^v_{H_1}$ are used to test the reconfigurability of the faulty system (proof in [1]). In particular, if after that acuator

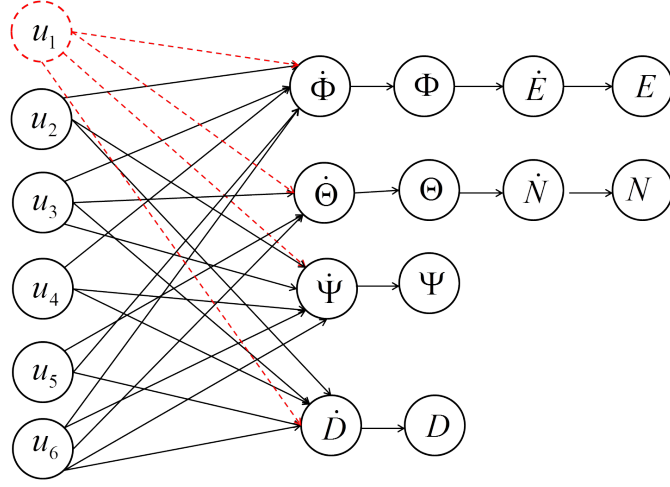


Figure 5.2: Digraph of a hexarotor

j fails ($u_j(t) = 0$ and $\bar{u}_j = 0$), there exist virtual faulty inputs $\delta v_{i_f}(t)$ that are constrained by zero on one side, the column of $B^v_{H_1}$ related to this faulty virtual input must be put to zero. The resulting matrix is $B^v_{f_{H_1}}$. In the end, UAVs reconfigurability to a rotor failure can be verified by the followign steps:

1. Testing the system input-connectivity through the use of its digraph
2. Testing the reduced rank condition $rank(B^v_{f_{H_1}}) = rank(B^v_{H_1}) = 4$.

Notice that, since $B^v_{H_1}$ is a square four by four matrix, as soon as one of the virtual inputs $\delta v_{i_f}(t)$ becomes constrained by zero on one side (because of a fault in one of the motors), the UAV becomes not reconfigurable.

As an example, suppose that motor 1 of the hexacopter H_1 fails; then conditions 1) and 2) has to be checked.

The digraph of H_1 is pictured in Figure 5.2. If motor one ($u_1(t) = 0$) breaks down the digraph remains input connected. Hence, input connectivity is always verified. As the number of rotor increases the number of redundancies raises and requirement 1) remains satisfied. Henceforward, the focus will be pointed on the virtual input matrix.

Condition 2) has to be verified analyzing the virtual inputs $\delta v_i(t)$, $i = 1, ..4$. In the equilibrium:

$$\begin{cases} \bar{v}_1 = \sum_{i=1}^6 \bar{u}_i = \frac{mg}{K_T} \\ \bar{v}_2 = \bar{u}_1 - \bar{u}_4 = 0 \\ \bar{v}_3 = \bar{u}_2 - \bar{u}_5 = 0 \\ \bar{v}_4 = \bar{u}_3 - \bar{u}_6 = 0 \end{cases} \implies \bar{v}_2 = -\bar{u}_4 = 0 \quad (5.14)$$

while outside the equilibrium:

$$\begin{cases} \delta v_1(t) = \sum_{i=2}^6 \delta u_i(t) \\ \delta v_2(t) = v_2(t) = -u_4(t) \leq 0 \\ \delta v_3(t) = v_3(t) = u_2(t) - u_5(t) \\ \delta v_4(t) = v_4(t) = u_3(t) - u_6(t). \end{cases} \quad (5.15)$$

Therefore, the second column of $B^v_{H_1}$ must be set to zero and the resulting faulty virtual input matrix $B^v_{fH_1}$ will have rank equal to three. The system is not reconfigurable respect to a failure on the first motor .

5.3 Hexacopter

In the previous Section it has been proved that the LVA would be not able to reconfigure the rotors speed of H_1 if the first rotor breaks.

Notice that similar results can be obtained if one of the other actuators is in fault (see equations (5.11) and (5.13)). Indeed, if for example motor 2 fails, the third equation of (5.13) leads to $\bar{u}_5 = 0$ and equations (5.11) give $v_3(t) = -u_5(t) \leq 0$. Thus, the faulty multicopter turns out to be not reconfigurable.

To complete the analysis, the H_2 configuration has been studied. The mixer matrix is given by equation (3.34). After multiplication by matrix J^{-1} (equation (5.5)) and change of variables:

$$B_{H_2} = \begin{bmatrix} -K_z & -K_z & -K_z & -K_z & -K_z & -K_z \\ -K_r a & -K_r a & -K_r a & K_r a & K_r a & K_r a \\ K_p b & 0 & -K_p b & -K_p b & 0 & K_p b \\ -K_y & K_y & K_y & -K_y & K_y & -K_y \end{bmatrix}. \quad (5.16)$$

Computing the reduced virtual matrix $B^v_{H_2}$ (see (5.19)) (as for the H_1 configuration), the virtual inputs $\delta v_i(t)$ are given by the following equations:

$$\begin{cases} \delta v_1(t) = \sum_{i=1}^6 \delta u_i(t) \\ v_2(t) = -2u_1(t) + 2u_5(t) \\ v_3(t) = u_1(t) - u_3(t) - u_4(t) + u_6(t) \\ v_4(t) = u_2(t) - 2u_4(t) + u_5(t). \end{cases} \quad (5.17)$$

While in the operating point equations (5.17) become:

$$\begin{cases} \bar{v}_1 = \sum_{i=1}^6 \bar{u}_i = \frac{mg}{K_T} \\ \bar{v}_2 = -2\bar{u}_1 + 2\bar{u}_5 = 0 \\ \bar{v}_3 = \bar{u}_1 - \bar{u}_3 - \bar{u}_4 + \bar{u}_6 = 0 \\ \bar{v}_4 = \bar{u}_2 - 2\bar{u}_4 + \bar{u}_5 = 0. \end{cases} \quad (5.18)$$

Therefore, the virtual input matrix of H_2 is:

$$B^v_{H_2} = \begin{bmatrix} -K_z & 0 & 0 & 0 \\ 0 & K_r a & K_r a & -K_r a \\ 0 & 0 & K_p b & 0 \\ 0 & K_y & -K_y & K_y \end{bmatrix}. \quad (5.19)$$

Subsequently, the system reconfigurability analysis is applied to the faulty multi-rotor H_2 with $u_1(t) = 0$, $\bar{u}_1 = 0$. Then according to equation (5.18) the breakeage of motor 1 implies that motor 5 needs to be turned off at least in the equilibrium point. While around the equilibrium the virtual input $v_2(t)$ becomes constrained by zero on one side. Then:

$$\begin{cases} \bar{v}_2 = 2\bar{u}_5 = 0 \\ v_2(t) = +u_5(t) \geq 0. \end{cases} \quad (5.20)$$

Suppose now that the second rotor is damaged ($u_2(t) = 0$, $\bar{u}_2 = 0$) the result is given by equations (5.21):

$$\begin{cases} \bar{v}_4 = -2\bar{u}_4 + \bar{u}_5 = 0 \\ v_4(t) = -2u_4(t) + u_5(t). \end{cases} \quad (5.21)$$

Since, the faulty rotor does not bring any other rotor to zero, the system turns out to be reconfigurable.

Table 5.1 resumes the results of the reconfigurability analysis applied to H_1 and H_2 if one at a time the rotor speed $u_j(t)$ is set to zero for $j = 1, \dots, 6$.

	Reconfigurability
H_1	no reconfigurable
H_2	rotors: 2, 3, 6

Table 5.1: Summary table of reconfigurable rotors for H_1 and H_2

Note that, the direction of rotation of the propellers influences the system reconfigurability.

5.3.1 Simulation

In FTC a diagnosis unit is able to isolate and detect the fault. In this case it is assumed that the fault detection has been already accomplished. Therefore, the diagnoser output is a vector η :

$$\eta = [\eta_1 \quad \eta_2 \quad \dots \quad \eta_{N_r}] \quad (5.22)$$

where N_r corresponds to the number of engines of the multicopter. Each element of η can be 0 (if the correspondent motor failed) or 1 (the correspondent actuator is not in fault). The information given by η is then translated on the input matrix of the system as:

$$B_{H_\eta} = B_H \text{diag} [\eta_1 \quad \eta_2 \quad \dots \quad \eta_{N_r}]. \quad (5.23)$$

Then the LVA is computed according to equation (5.3) and applied to the faulty system. The Simulink implementation of the LVA on the multicopter simulator has been performed as depicted in the scheme 5.3. A smooth fixed point tra-

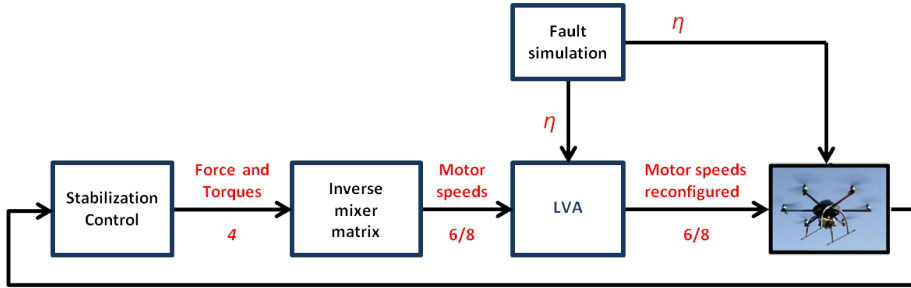


Figure 5.3: Control system using fault-tolerant control

jectory with the aircraft hovering at an altitude of 2.5 m has been created and the fault has been reproduced, setting to zero at instant $t_f = 20$ s one of the motors speeds. The reconfiguration occurs at instant $t_r = 20.1$ s. The time delay $t_r - t_f = 0.1$ s has been chosen to be equal to ten times the time cycle of the FCU. Even if for each one of the configurations taken into account, the connection between simulation results and theoretical ones was checked (performing a simulation for each one of the six possible fault occurrences), in this work will be shown only the response of the system to one faulty case.

PNPNPN configuration

Considering the hexacopter H_1 (see 3.2a) it has been demonstrated that it is not reconfigurable. Then, if the first motor is in fault $u_1(t) = 0$ the result of the simulation is depicted in Figure 5.4.

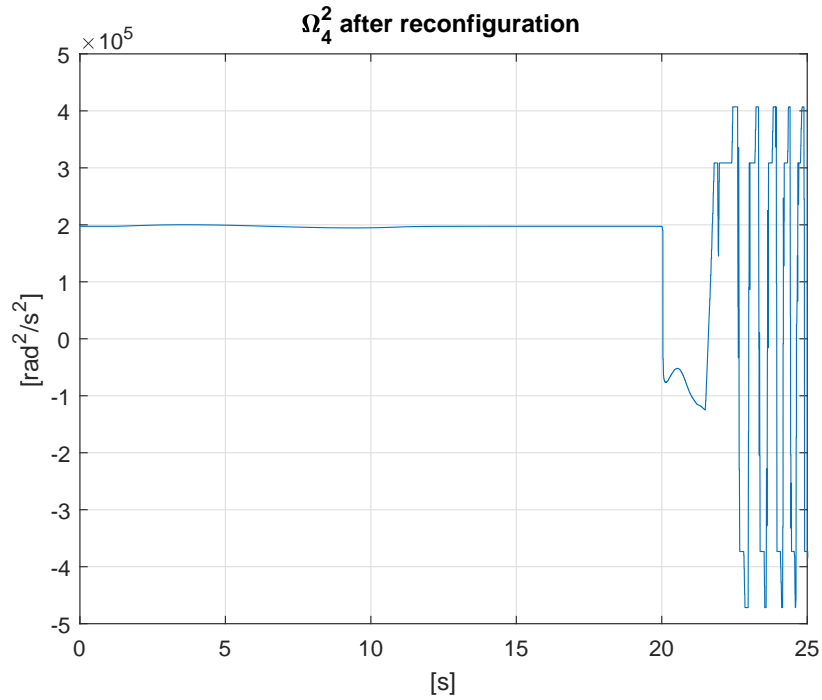
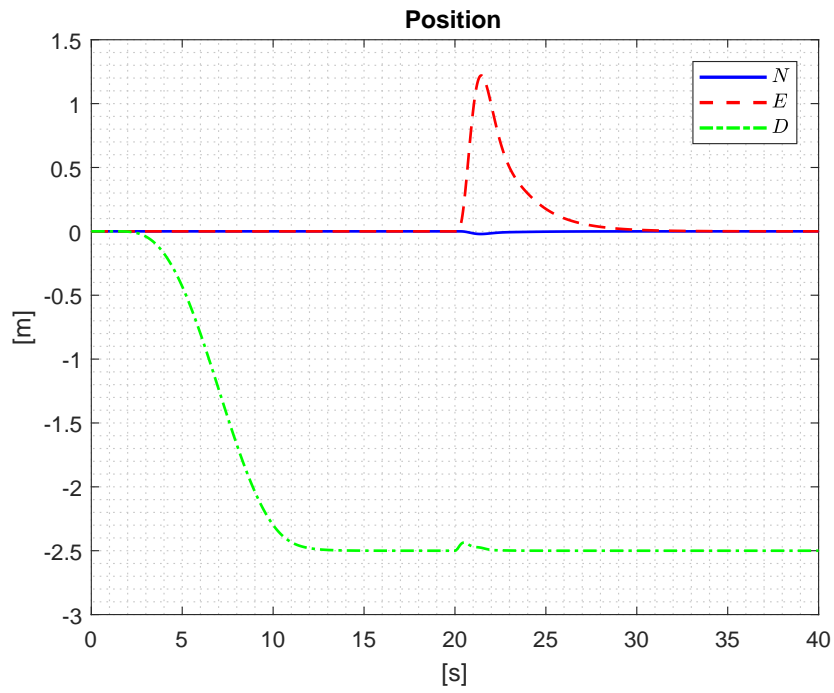
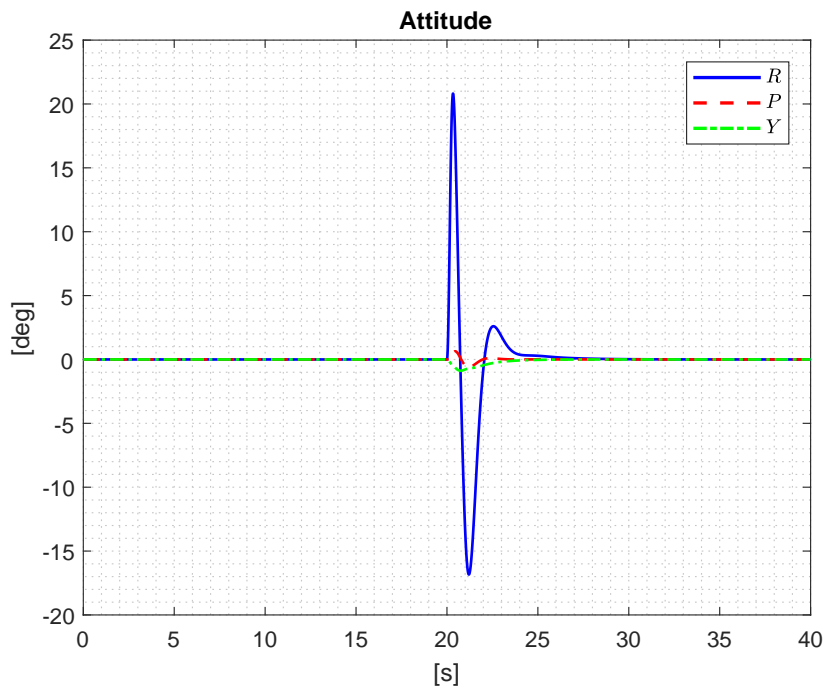


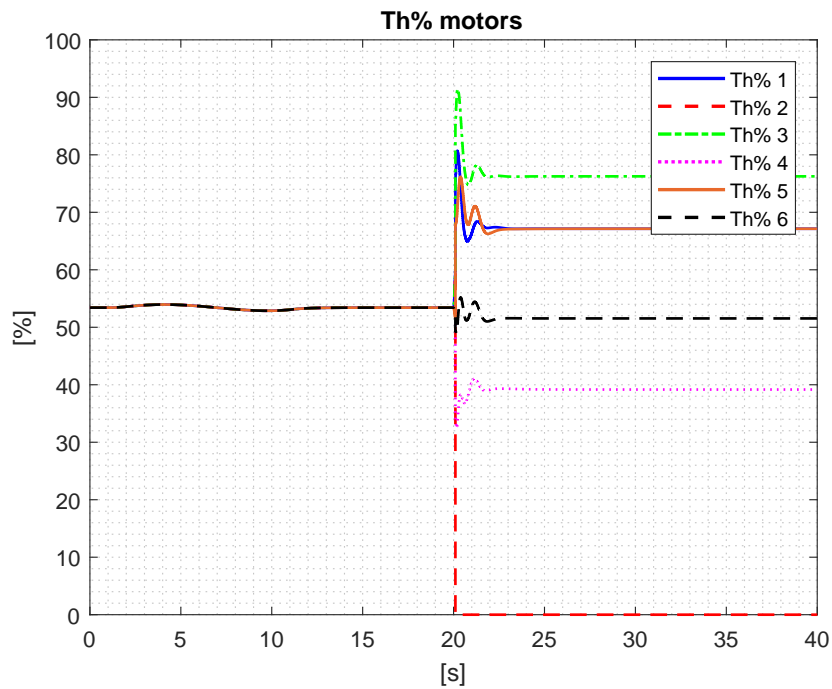
Figure 5.4: Rotational speed of rotor number four

The LVA tries to bring to zero the speed of the fourth rotor. But before this happens the hexarotor deflects into an area where u_4 should develop a negative speed (see 5.4) in order to compensate the lost of the first motor. Since this cannot happen the multirotor becomes unstable and falls down.

NPPNPN configuration

In order to show the difference respect to the previous case, the hexacopter H_2 (see 3.2b) is considered. Furthermore, it is hypothesized that u_2 is lost and the control allocator acts 0.1 s after the time instant $t_f = 20$ s at which the fault occurs. In order to center the focus on the capability of the system to recover the reference trajectory, only the plots relative to position, attitude and throttles are shown. The results are given by Figures 5.5, 5.6 and 5.7

Figure 5.5: Position response of H_2 Figure 5.6: Attitude response of H_2

Figure 5.7: Throttles of H_2

Notice that, according to theory the multicopter is reconfigurable respect to a fault on the second rotor. Indeed the LVA manages to reconfigure the speeds of each rotor in order to bring the aircraft in hovering condition. Furthermore, the greatest value of throttle is given by motor three, which is on the same axis of the faulty engine and rotates in the same direction. This consideration justifies the fact that it has to develop more torque respect to the other rotors.

5.4 Octocopter

Applying the same reconfigurability analysis, previously explained, to the matrices 3.37 and 3.38 of the octocopters O_1 and O_2 respectively, the following equations and matrices are obtained for O_1 :

$$B^v_{O_1} = \begin{bmatrix} -K_z & 0 & 0 & 0 \\ 0 & -K_r a \frac{3\pi}{8} & -K_r a \frac{\pi}{8} & -K_r a \frac{\pi}{8} \\ 0 & K_p b \frac{3\pi}{8} & K_p b \frac{3\pi}{8} & -K_p b \frac{\pi}{8} \\ 0 & K_y & -K_y & K_y \end{bmatrix}; \quad (5.24)$$

$$\begin{cases} \delta v_1(t) = \sum_{i=1}^8 \delta u_i(t) \\ v_2(t) = u_1(t) - u_4(t) - (\sqrt{2} - 1)u_5(t) - (2 - \sqrt{2})u_6(t) + (2 - \sqrt{2})u_7(t) + (\sqrt{2} - 1)u_8(t) \\ v_3(t) = u_2(t) + (\sqrt{2} - 1)u_4(t) - 2(\sqrt{2} - 1)u_5(t) - (3 - 2\sqrt{2})u_6(t) - 2(\sqrt{2} - 1)u_7(t) + \dots \\ \dots + (\sqrt{2} - 1)u_8(t) \\ v_4(t) = u_3(t) + (\sqrt{2} - 1)u_4(t) + (2 - \sqrt{2})u_5(t) - (2 - \sqrt{2})u_6(t) - (\sqrt{2} - 1)u_7(t) - u_8(t) \end{cases} \quad (5.25)$$

and for O_2 :

$$B^v_{O_2} = \begin{bmatrix} -K_z & 0 & 0 & 0 \\ 0 & -K_r a \frac{3\pi}{8} & -K_r a \frac{\pi}{8} & -K_r a \frac{\pi}{8} \\ 0 & K_p b \frac{3\pi}{8} & K_p b \frac{3\pi}{8} & -K_p b \frac{\pi}{8} \\ 0 & K_y & K_y & -K_y \end{bmatrix}, \quad (5.26)$$

$$\begin{cases} \delta v_1(t) = \sum_{i=1}^8 \delta u_i(t) \\ v_2(t) = u_1(t) - u_4(t) - (\sqrt{2} + 1)u_5(t) - (\sqrt{2})u_6(t) + (\sqrt{2})u_7(t) + (\sqrt{2} + 1)u_8(t) \\ v_3(t) = u_2(t) + (\sqrt{2} - 1)u_4(t) + 2u_5(t) + u_6(t) - 2u_7(t) - (\sqrt{2} + 1)u_8(t) \\ v_4(t) = u_3(t) + (\sqrt{2} - 1)u_4(t) - \sqrt{2}u_5(t) - \sqrt{2}u_6(t) + (\sqrt{2} - 1)u_7(t) + u_8(t). \end{cases} \quad (5.27)$$

In order to test the reconfigurability of O_1 , it is supposed that motor one breaks down. The equations (5.25) in the equilibrium, become:

$$\begin{cases} \bar{v}_1 = \sum_{i=2}^8 \bar{u}_i = \frac{mg}{K_T} \\ \bar{v}_2 = -\bar{u}_4 - (\sqrt{2} - 1)\bar{u}_5 - (2 - \sqrt{2})\bar{u}_6 + (2 - \sqrt{2})\bar{u}_7 + (\sqrt{2} - 1)\bar{u}_8 = 0 \\ \bar{v}_3 = \bar{u}_2 + (\sqrt{2} - 1)\bar{u}_4 - 2(\sqrt{2} - 1)\bar{u}_5 + (3 - 2\sqrt{2})\bar{u}_6 - (2\sqrt{2} - 1)\bar{u}_7 + (\sqrt{2} - 1)\bar{u}_8 = 0 \\ \bar{v}_4 = \bar{u}_3 + (\sqrt{2} - 1)\bar{u}_4 + (2 - \sqrt{2})\bar{u}_5 - (2 - \sqrt{2})\bar{u}_6 - (\sqrt{2} - 1)\bar{u}_7 - \bar{u}_8 = 0. \end{cases} \quad (5.28)$$

Notice that, if $\bar{u}_1 = 0$, it does not force any other rotor to zero. Furthermore, does not exist any faulty virtual input $\delta v_i(t)$ which contains the fault ($u_1(t)$) and that

becomes constrained on one side by zero. In fact, $v_2(t)$ (equations (5.29)) after the fault continues to be either positive or negative.

$$\begin{cases} \delta v_1(t) = \sum_{i=2}^8 \delta u_i(t) \\ v_2(t) = -u_4(t) - (\sqrt{2} - 1)u_5(t) - (2 - \sqrt{2})u_6(t) + (2 - \sqrt{2})u_7(t) + (\sqrt{2} - 1)u_8(t) \\ v_3(t) = u_2 + (\sqrt{2} - 1)u_4(t) - 2(\sqrt{2} - 1)u_5(t) - (3 - 2\sqrt{2})u_6(t) - 2(\sqrt{2} - 1)u_7(t) + \\ \dots + (\sqrt{2} - 1)u_8(t) \\ v_4(t) = u_3(t) + (\sqrt{2} - 1)u_4(t) + (2 - \sqrt{2})u_5(t) - (2 - \sqrt{2})u_6(t) - (\sqrt{2} - 1)u_7(t) - u_8(t). \end{cases} \quad (5.29)$$

The same result is achieved in the case of lost of any of the other engines. Therefore, the octocopter O_1 is fully reconfigurable against the breakage of one of its actuators.

Focusing on O_2 and supposing that motor one is lost it is possible to retrieve the equations of the faulty virtual inputs in the equilibrium:

$$\begin{cases} \bar{v}_1 = \sum_{i=2}^8 \bar{u}_i = \frac{mg}{K_T} \\ \bar{v}_2 = -\bar{u}_4 - (\sqrt{2} + 1)\bar{u}_5 - (\sqrt{2})\bar{u}_6 + (\sqrt{2})\bar{u}_7 + (\sqrt{2} + 1)\bar{u}_8 = 0 \\ \bar{v}_3 = \bar{u}_2 + (\sqrt{2} - 1)\bar{u}_4 + 2\bar{u}_5 + \bar{u}_6 - 2\bar{u}_7 - (\sqrt{2} + 1)\bar{u}_8 = 0 \\ \bar{v}_4 = \bar{u}_3 + (\sqrt{2} - 1)\bar{u}_4 - \sqrt{2}\bar{u}_5 - \sqrt{2}\bar{u}_6 + (\sqrt{2} - 1)\bar{u}_7 + \bar{u}_8 = 0, \end{cases} \quad (5.30)$$

and outside the equilibrium:

$$\begin{cases} \delta v_1(t) = \sum_{i=2}^8 \delta u_i(t) \\ v_2(t) = -u_4(t) - (\sqrt{2} + 1)u_5(t) - (\sqrt{2})u_6(t) + (\sqrt{2})u_7(t) + (\sqrt{2} + 1)u_8(t) \\ v_3(t) = u_2(t) + (\sqrt{2} - 1)u_4(t) + 2u_5(t) + u_6(t) - 2u_7(t) - (\sqrt{2} + 1)u_8(t) \\ v_4(t) = u_3(t) + (\sqrt{2} - 1)u_4(t) - \sqrt{2}u_5(t) - \sqrt{2}u_6(t) + (\sqrt{2} - 1)u_7(t) + u_8(t). \end{cases} \quad (5.31)$$

According to equations (5.31), $\delta v_1(t)$ and $v_2(t)$ can be positive or negative after the lost of motor one. Note that, testing the other engines the outcome does not change. Then, the octocopter O_2 is fully reconfigurable.

5.4.1 Simulation

The implementation of the LVA on the multicopter simulator follows the strategy presented in Figure 5.3. Also in this case, the pertinence of theoretical and simulation results has been verified for each motor and in both the multirotor configurations. In the following are not shown all the possible faulty cases, since it would lead to show an excessive number of figures.

Both the octocopter configurations (see Figures 3.3a and 3.3b) are fully reconfigurable; thus, the two multirotors are compared in the case $u_1(t)$ fails. In order

to center the focus on the capability of the system to recover the hovering reference, only the plots relative to position, attitude and throttles are presented. The results of the simulations are given in Figures 5.8, 5.9 and 5.10 for O_1 , while in Figures 5.11, 5.12 and 5.13 for O_2 .

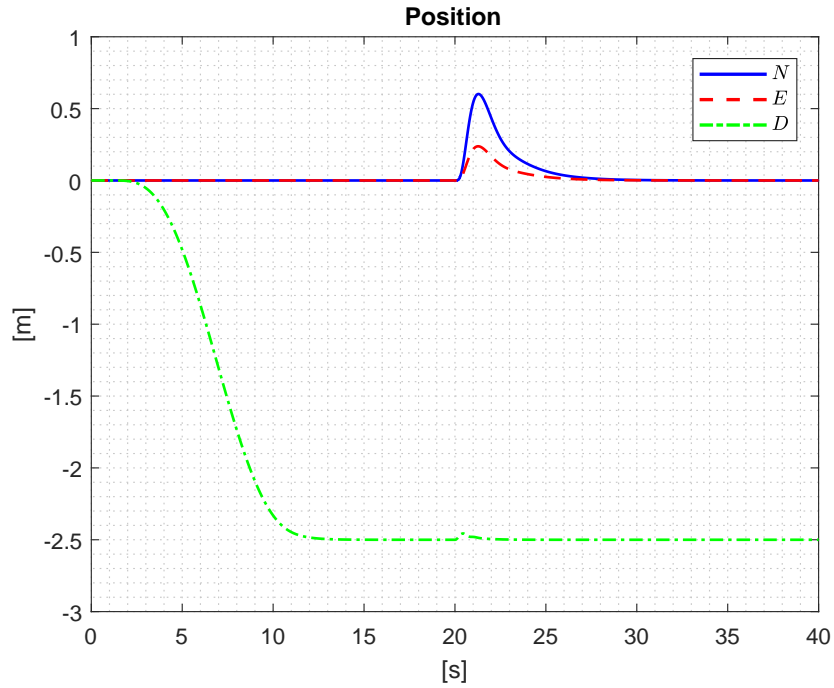
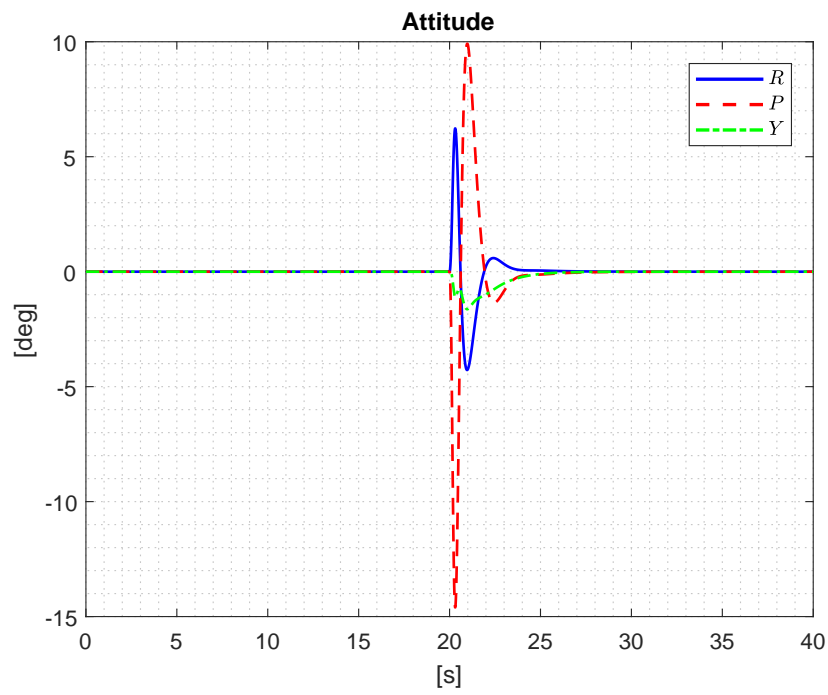
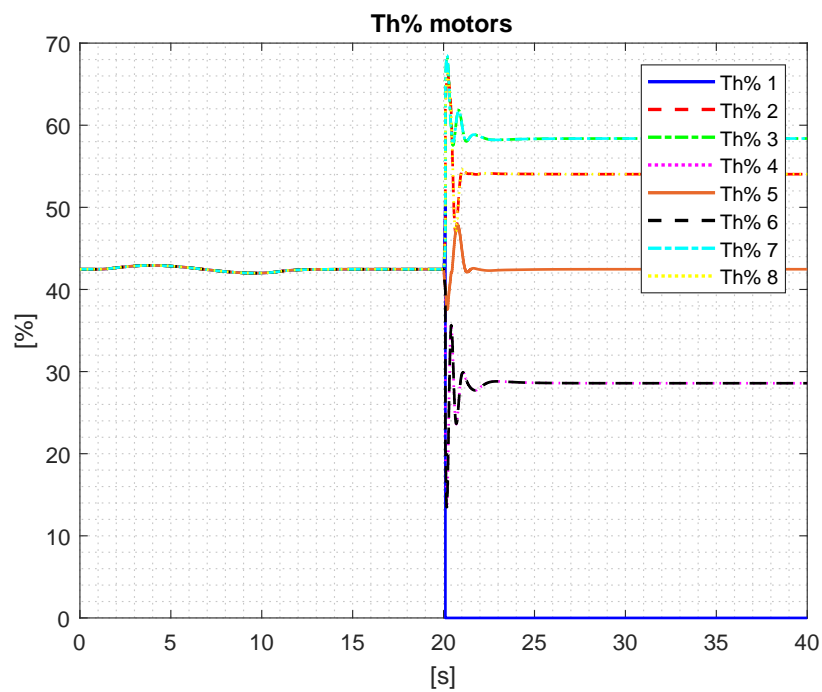
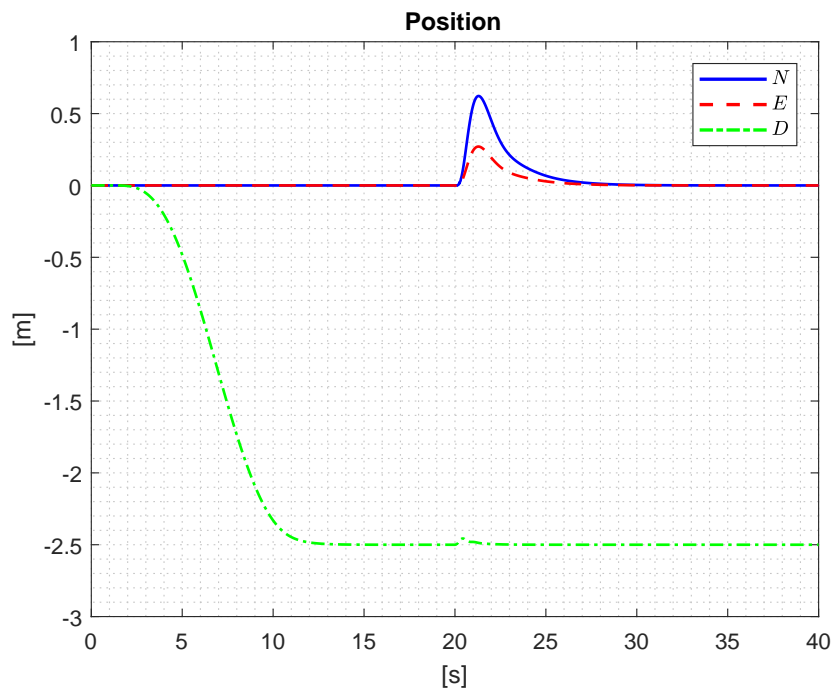
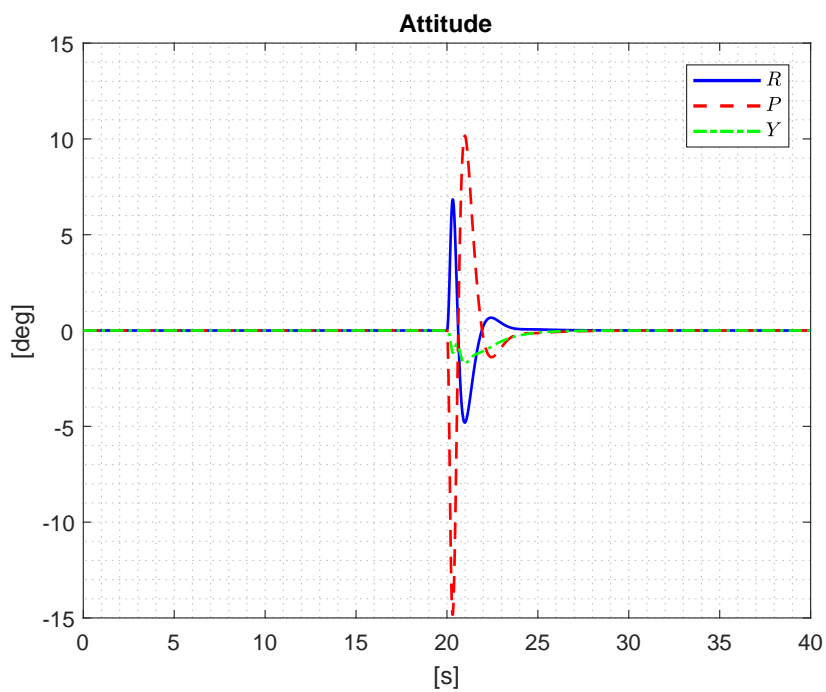
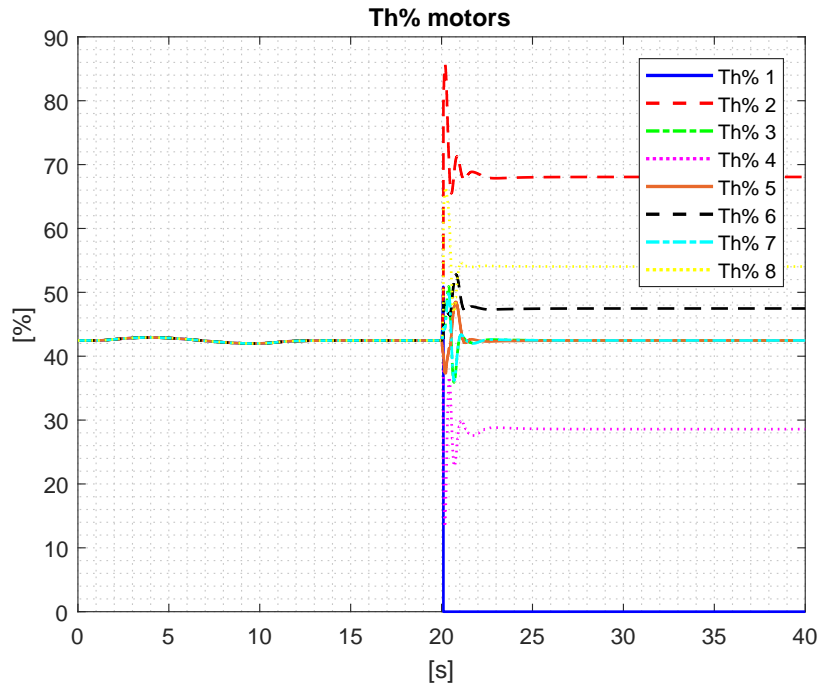


Figure 5.8: Position response of O_1

Figure 5.9: Attitude response of O_1 Figure 5.10: Throttles of O_1

Figure 5.11: Position response of O_2 Figure 5.12: Attitude response of O_2

Figure 5.13: Throttles of O_2

Considerations

The two multirotors are reconfigurable respect to a fault on $u_1(t)$, but while the maximum throttle developed in O_2 (see Figure 5.13) is generated by the second motor, in O_1 it is given by engines three and seven (see Figure 5.10). Therefore, in the reconfigured octocopter O_1 , the throttles are better redistributed respect to O_2 .

Notice also that the maximum peak of the throttles in O_1 is smaller respect to the ones in O_2 .

Moreover, the oversizing done on both the octocopters (see Chapter 2) guarantee values of throttles more restrained respect to the hexacopter (H_2) ones.

Conclusions

The work has been focused on the preliminary design, the modelling and the analysis of multirotor UAVs able to carry a vision system and a gas detector for the task of monitoring industrial plants.

In the first chapter, a market scouting of the devices (stereocamera and gas detector) available on the market is presented. Therefore, the choice of the vision system is performed based on this analysis. Then a sperimental test is run to evaluate the performances of a laser targeting system mounted on a drone. The results of the test have led to choose an OGI gas detector.

In the second chapter, in order to design customizable monitoring platforms, two multirotor structures (with six and eighth rotors) are considered and a sizing procedure is described defining the equations and parameters used. Therefore, the actuators are chosen in accordance with the requirements and assumptions made in terms of flight time, maximum take-off weight and maximum thrust over weight coefficient. Then, the dimensions of the two multicopters are given.

In the third chapter, the methods used for the characterization of the actuators and the formalisms adopted to derive the multicopter mathematical model are shown. Then, the hexacopter and octorotor models are realized and implemented in Simulink.

The fourth chapter deals with the design of the control architecture of the two multicopters. For this purpose PIDs regulators are tuned using an H_∞ structured synthesis applied to the linearized multirotor models. Furthemore, a drift analysis is conducted leading to understand the influence that the drift caused by the vision system may have on the position of a drone.

In the last chapter, a fault tolerance analysis on the hexarotor and octorotor is addressed, together with the computation and implementation of a LVA to reconfigure the system after the fault of one of the engines. In conclusion, the results confirmed that:

- As the number of redundancies increases the robustness of the system to actuators fault raises.
- The success of the reconfiguration does not depend only on the number of the actuators but on the system structure too.
- The direction of rotation of the propellers influences the performances and

the success of the reconfiguration procedure.

- The choice of oversizing the octocopter (during the sizing stage) allows to reduce the possibility of reaching excessive values of throttle when a fault occurs.
- As the reconfigurability of the system depends on its structure, the symmetry of the frame is an important parameter.

Further developments

There are several points to enforce and to develop on the base of this work:

- More precise inertia values can be computed with the support of CAD softwares to the purpose of realizing the real monitoring platform.
- The multicopter model can be improved introducing external dynamic effects.
- The systems can be tuned by the adoption of non-linear control strategies.
- A diagnoser could be developed and then tested on the simulators in order to complete the active fault tolerant control system.
- Strategies different from static LVA which use more complex algorithms can be applied in order to compare the results.
- More complex models can be adopted to quantify the drift.

Bibliography

- [1] D. Vey and J. Lunze. Structural reconfigurability analysis of multirotor uavs after actuator failures. In *IEEE Conference on Decision and Control (CDC)*. IEEE, 2015.
- [2] M. Giurato. Design, integration and control of a multirotor UAV platform. Master's thesis, Politecnico di Milano, 2015.
- [3] G. Meinsma. Unstable and non proper weights in H_∞ control. *Automatica*, 31(11):1655–1658, November 1995.
- [4] S. Panza. *Structured flight control law design for helicopters and tiltrotors*. PhD thesis, Politecnico di Milano, 2018.
- [5] D. Chevallard. Design, identification and control of a micro aerial vehicle. Master's thesis, Politecnico di Milano, 2017.
- [6] J. Delmerico and D. Scaramuzza. A benchmark comparison of monocular visual-inertia odometry algorithms for flying robots. In *IEEE International Conference on Robotics and Automation (ICRA)*. IEEE, 2018.
- [7] M. Bergamasco and M. Lovera. Identification of linear models for the dynamics of a hovering quadrotor. *IEEE Transactions on Control Systems Technology*, 2014.

